



**HAL**  
open science

# Helium-3 Magnetic Resonance Elastography of the lung

Roberta Santarelli

► **To cite this version:**

Roberta Santarelli. Helium-3 Magnetic Resonance Elastography of the lung. Instrumentation and Detectors [physics.ins-det]. Université Paris Sud - Paris XI, 2013. English. NNT : 2013PA112026 . tel-01359197

**HAL Id: tel-01359197**

**<https://theses.hal.science/tel-01359197>**

Submitted on 2 Sep 2016

**HAL** is a multi-disciplinary open access archive for the deposit and dissemination of scientific research documents, whether they are published or not. The documents may come from teaching and research institutions in France or abroad, or from public or private research centers.

L'archive ouverte pluridisciplinaire **HAL**, est destinée au dépôt et à la diffusion de documents scientifiques de niveau recherche, publiés ou non, émanant des établissements d'enseignement et de recherche français ou étrangers, des laboratoires publics ou privés.

UNIVERSITÉ PARIS-SUD

ÉCOLE DOCTORALE : STITS

Laboratoire d'Imagerie par Résonance Magnétique Médicale et Multi-Modalités

**DISCIPLINE PHYSIQUE**

**THÈSE DE DOCTORAT**

soutenue le 27 février 2013

par

**Roberta Santarelli**

# Helium-3 Magnetic Resonance Elastography of the lung

devant le jury composé de

Dr Luc DARRASSE	Directeur de recherche CNRS, IR4M, Université Paris-Sud	<i>Directeur de thèse</i>
Dr Xavier MAÎTRE	Chargé de recherche CNRS, IR4M, Université Paris-Sud	<i>Co-directeur de thèse</i>
Dr Daniel ISABEY	Directeur de recherche Inserm, CRB3, Université Paris-Est	<i>Président du jury</i>
Pr Bernard VAN BEERS	Professeur des Universités Praticien Hospitalier Université Paris Diderot, CHU Beaujon, Inserm	<i>Rapporteur</i>
Pr Samuel PATZ	Professeur de radiologie, Harvard Medical School Directeur scientifique Massachusetts General Hospital	<i>Rapporteur</i>
Dr Patrick BERTHAULT	Chercheur CEA	<i>Examineur</i>
Pr Jesus RUIZ CABELLO	Professeur de physique-chimie Centro Nacional Investigaciones Cardiovasculares Universidad Complutense Madrid	<i>Examineur</i>



# Contents

<b>Contents .....</b>	<b>3</b>
<b>Acknowledgements (Remerciements) .....</b>	<b>9</b>
<b>Introduction.....</b>	<b>11</b>
<b>Chapter 1. Probing human lungs.....</b>	<b>15</b>
1.1. Respiratory system and human lungs .....	15
1.1.1. Anatomy.....	16
1.1.1.1. The extrathoracic region.....	16
1.1.1.2. The tracheobronchial and alveolar regions.....	18
1.1.2. Diseases.....	21
1.1.2.1. Asthma.....	22
1.1.2.2. Diagnosis of pulmonary diseases .....	27
1.2. Diagnostic tool and imaging techniques.....	27
1.2.1. Auscultation .....	27
1.2.2. Pulmonary function test .....	27
1.2.3. Imaging techniques .....	28
1.2.3.1. Radiography .....	28
1.2.3.2. X-ray computed tomodensitometry .....	29
1.2.3.3. Ultrasound imaging .....	29
1.2.3.4. Scintigraphy.....	30
1.2.3.5. SPECT .....	32
1.2.3.6. PET .....	34

---

1.2.3.7.	Hydrogen magnetic resonance imaging of the lung .....	35
<b>Chapter 2.</b>	<b>Hyperpolarized helium-3 Magnetic Resonance Imaging .....</b>	<b>37</b>
2.1.	Nuclear Magnetic Resonance .....	38
2.1.1.	A spin in a magnetic field .....	38
2.1.2.	NMR signal acquisition.....	43
2.2.	Magnetic Resonance Imaging .....	44
2.2.1.	k-space and gradients .....	45
2.2.1.1.	Frequency encoding gradient.....	45
2.2.1.2.	Phase encoding gradient .....	45
2.2.1.3.	Slice selection gradient.....	46
2.2.1.4.	Fourier space acquisition.....	46
2.3.	Hyperpolarized helium-3 Nuclear Magnetic Resonance .....	48
2.3.1.	Hyperpolarized helium-3.....	49
2.3.1.1.	Metastability exchange hyperpolarization.....	50
2.3.1.2.	Centralized production and gas delivery .....	53
2.3.1.3.	On-site production and administration .....	53
2.3.2.	Helium-3 imaging .....	60
2.3.2.1.	Total magnetic moment.....	60
2.3.2.2.	RF depolarization .....	60
2.3.2.3.	Longitudinal relaxation .....	61
2.3.2.4.	Transverse relaxation.....	61
<b>Chapter 3.</b>	<b>Magnetic resonance elastography of the lungs.....</b>	<b>63</b>
3.1.	Basics of elastography .....	64
	<b>Linear elasticity reminders [100] .....</b>	<b>67</b>
3.1.1.	Static elastography .....	67
3.1.2.	Dynamic elastography.....	68
3.1.3.	Continuous elastography .....	68

---

3.1.4.	Transient elastography .....	68
3.2.	Magnetic Resonance elastography .....	69
3.2.1.	Motion generation .....	69
3.2.1.1.	Piezoelectric transducers .....	70
3.2.1.2.	Electromechanical transducers .....	71
3.2.1.3.	Electropneumatic transducers.....	72
3.2.1.4.	Electropneumatic transducers and guided pressure waves.....	73
3.2.2.	Motion encoding .....	74
3.2.2.1.	Gradient Echo or Fast Field Echo sequence .....	75
3.2.2.2.	Spin Echo or Refocused Field Echo sequence .....	76
3.2.3.	Image processing.....	77
3.2.3.1.	Equation of motion .....	77
3.2.3.2.	Inverse problem .....	78
3.3.	Magnetic Resonance Elastography of the lung .....	81
3.3.1.	Hydrogen Magnetic Resonance Elastography .....	81
3.3.2.	Helium-3 Magnetic Resonance Elastography .....	81
<b>Chapter 4.</b>	<b>Validity of helium-3 Magnetic Resonance Elastography .....</b>	<b>83</b>
4.1.	Introduction .....	83
4.2.	Primary assumption for helium-3 MRE: Gas confinement in the lung .....	85
4.2.1.	Introduction .....	85
4.2.2.	Materials and methods .....	85
4.2.2.1.	MRE sequence acceleration.....	87
4.2.2.2.	Hydrogen MRE .....	87
4.2.2.3.	Hyperpolarized helium-3 MRE .....	88
4.2.2.4.	MRE data processing.....	89
4.2.3.	Results .....	91
4.2.3.1.	MRE sequence acceleration.....	91
4.2.3.2.	Hydrogen and helium-3 MRE .....	91

---

4.2.4.	Discussion .....	96
4.3.	Secondary assumption for helium-3 MRE: Insensitivity to gas content .....	98
4.3.1.	Introduction .....	98
4.3.2.	Materials and methods .....	98
4.3.3.	Results and Discussion.....	100
4.4.	Conclusion.....	102
<b>Chapter 5.</b>	<b>Sensitivity and quantitation of lung Magnetic Resonance Elastography .....</b>	<b>103</b>
5.1.	Introduction .....	103
5.2.	Magnetic Resonance Elastography sensitivity to lung inflation.....	104
5.2.1.	Introduction .....	104
5.2.2.	Materials and methods .....	104
5.2.3.	Results.....	105
5.2.4.	Discussion .....	108
5.3.	Magnetic Resonance Elastography sensitivity to gravity.....	109
5.3.1.	Introduction .....	109
5.3.2.	Materials and methods .....	109
5.3.3.	Results.....	110
5.3.4.	Discussion .....	113
5.4.	Conclusion.....	114
<b>Chapter 6.</b>	<b><i>In vivo</i> helium-3 Magnetic Resonance Elastography of the lung.....</b>	<b>117</b>
6.1.	Introduction .....	117
6.2.	Materials and methods.....	117
6.2.1.	<b><i>In vivo</i> hyperpolarized helium-3 MRE acquisitions in rat lungs .....</b>	<b>117</b>
6.2.2.	<b><i>In vivo</i> hyperpolarized helium-3 MRE acquisitions in healthy human lungs.....</b>	<b>119</b>
6.2.3.	<b>MRE data reconstruction .....</b>	<b>119</b>
6.3.	<b>Results.....</b>	<b>120</b>
6.4.	<b>Discussion .....</b>	<b>122</b>

**6.5. Conclusion** ..... 125

**Conclusions and perspectives**..... **126**

Table of symbols ..... 130

Bibliography ..... 133

*A ma grand-mère Maria*

## **Acknowledgements (Remerciements)**

Dans un travail de recherche, la réussite s'emporte grâce à un nombre important de collaborations. C'est d'autant plus vrai sur un projet qui a comme sujet les êtres vivants étudiés entre la médecine et la physique. Dans un travail de recherche d'une thèse de doctorat, avant toutes collaborations au projet, il y a des personnes qui enseignent le métier de chercheur, qui poussent à dépasser les limites et qui suivent la progression du travail à une distance telle que l'étudiant soit autonome mais pas seul en cas de besoin. En dehors du lieu de travail, un groupe « d'étrangers », famille et amis, est fondamental pour le soutien moral et psychologique du futur docteur. Ce qui fait un nombre important de personnes à remercier à la fin d'une thèse de doctorat.

Pour ce travail de thèse, tout d'abord je dois remercier Luc Darrasse, mon directeur de thèse, et Xavier Maître, mon co-directeur de thèse, pour avoir cru en moi et mes capacités et m'avoir poussé jusqu'au bout de ce projet. En particulier, Xavier Maître a été mon « maître » dans le vrai sens du mot ; avec son infinie patience et sa constante présence, il m'a initié au métier de chercheur, il m'a montré ses côtés obscurs et comment en faire sortir les aspects positifs, il m'a toujours soutenu et assuré son aide. Sans lui, je n'aurais pas eu ni des résultats positifs ni ne serais devenue qui je suis.

La plus grande et importante collaboration a été celle avec Ralph Sinkus, qui m'a fait connaître le monde de l'élastographie et qui, grâce à son superbe logiciel de reconstruction, m'a simplifié la vie.

Un grand merci va à Daniel Isabey et à son équipe de recherche Inserm, Université Paris-Est, qui a participé à quelques une des « nuits blanche » d'expérimentations avec nous et qui m'a ouvert les portes de son laboratoire ; grâce à lui et à Adam Caluch j'ai appris tous que je sais sur la manipulation des petits animaux.

Pierre-Yves Brillet, pneumologue de l'hôpital d'Avicenne, a énormément collaboré dans le cadre du protocole sur la fibrose et m'a précieusement aidée à comprendre la complexe structure des poumons.

L'U2R2M avant d'être IR4M a été ma deuxième maison, autre que lieu de travail, et pour cela les remerciements sont double pour chacun, autant comme collaborateurs que comme soutiens moral de mon travail.

Rose-Marie Dubuisson et Emeline Boriassé ont été des piliers fondamentaux pour mes expérimentations... et pour des soirées pas trop sages.

Anne Leroy-Willing, avec son expérience, m'a guidée et conseillée pendant mes moments difficiles avec la manipulation des rats : je ferai trésor de ses enseignements.

Marie Poirier-Quinot, Lionel Martin, Lucie Calmels, Simon Lambert, Mathieu Sarracanie, Kyle Hill et Pascal Hagot ont été mes « collègues » et amis d'aventures pour toutes la durée de ma thèse et même au-delà.

José Manuel Pérez Sánchez m'a soutenue, aidée, confortée et amenée jusqu'à la conclusion de mon travail avec tous ses moyens et sa force. Muchas gracias chico.

Je remercie infiniment Marion Tardieu, sa joie et sa disponibilité : jamais je n'oublierai nos moments avec Freddy Mercury et The Queen.

Je remercie toutes les équipes de PHeLINET distribuées partout en Europe pour les échanges et les conseils fructueux que nous avons pu avoir au cours des trois années du projet.

Enfin, je remercie ma famille et mes proches qui même à des kilomètres de distance ont été capables, comme toujours, d'être à mon côté et de m'apporter leur soutien et leur amour.

## Introduction

Worldwide, lung cancer is the most common cancer in terms of both incidence and mortality. In 2012, 160,340 Americans were expected to die from lung cancer, which means a mortality of nearly 28% from all cancer [1]. In terms of prevalence, approximately 373,489 Americans live with lung cancer. In terms of incidence, 226,160 new cases, 14% of all cancer, were expected to be diagnosed [2], [3]. In the United-States, Chronic Obstructive Pulmonary Disease is the fourth leading cause of death. Moreover, it induces serious long-term disability. More than 12 million people are currently diagnosed with Chronic Obstructive Pulmonary Disease and an additional 12 million likely carry the disease and do not even know it. More specifically in the United-States, emphysema has been diagnosed in 2001 in 3 million adults and 15 thousand a year die from it. In France, Chronic Obstructive Pulmonary Disease affects more than 3.5 million people and kills 16 thousand patients every year. Besides, interstitial fibrosis affects 5 million people around the world and 20 thousand die from it every year. Two hundred thousand Americans suffer from idiopathic pulmonary fibrosis and 50 thousand new cases are reported each year. According to the American Lung Association, in the last few years, lung diseases have become the third most common cause of death worldwide after cardiovascular diseases and tumors. It is expected to rise up the ranking position in the next ten years.

Today, diagnosis of these pulmonary diseases usually occurs once symptoms have appeared and the damage caused by the disease is mostly irreversible. Hence there is a pressing need for methods that can detect these pathologies at earlier stages.

Pulmonary diseases alter the structure and the function of the lung mostly by modifying the viscoelastic properties of the lung parenchyma. The viscoelastic properties of pulmonary tissues cannot be probed *in vivo* with standard techniques, which are applied to other less remote organs. Computer tomography scans and surgical pulmonary biopsy can be used to diagnose advanced stages of the diseases. However, it is not yet possible to follow their

---

progression, to determine the optimal length of therapy, or to explore the administration of other agents potentially less toxic than those used nowadays. The causes and mechanisms of these diseases as well as the associated genetic factors are still largely undetermined. The society and medical issues are huge.

In the lung parenchyma, the viscoelastic properties are key parameters, which regulate the basic functions of the organ. They depend on the tissue structure, the biological conditions, and the pathological alterations of the lung parenchyma. They are dramatically altered by most of pulmonary diseases like cancer, emphysema, asthma, or interstitial fibrosis. They also physiologically evolve over the breathing cycle, according to the subject's position (prone, supine, upright), or with aging (a reduction of compression and shear moduli from 45% to 75% is recorded between age 20 and 60). Despite an *a priori* homogenous pulmonary tissue, the lung distensibility is partly shaped by gravity such that the upper regions of the lung are more stretched, hence more inflated, than the lower regions. Along this line, the transpulmonary pressure varies by 0.7 kPa between the apex and the base of the lung in healthy subjects. In essence, the viscoelastic properties of the pulmonary tissue should be very sensitive biomarkers of early pathophysiological changes.

Auscultation and tactual explorations are known for ages by physicians as non-invasive techniques to probe the state of the subject's lung. It is a very crude but efficient mapping of transmitted vibrations. Tactual exploration is also a widely valid approach, used by physicians, to explore the mechanical properties of the human tissue. For example, the induced vibrations would be attenuated by a local liquid pleural effusion while they would be enhanced for an acute respiratory disease. However, those simple techniques are qualitative and highly subjective.

This PhD project aims at the development of a new modality which should allow to detect, quantify, and classify diseases that modify the viscoelastic properties of the lung parenchyma like emphysema, interstitial or idiopathic fibrosis, sarcoidosis, or cancer. This modality, hyperpolarized helium-3 Magnetic Resonance Elastography (MRE), will benefit from the noninvasive nature and the sensitivity of the technique as well as from the huge hyperpolarized helium-3 signal. Recently initiated at Mayo Clinic and IR4M, this technique allows the detection of human tissue motions and the follow-up of their response to a mechanical stress in order to reveal its viscoelastic properties.

---

In their seminal experiment in 2006 [4], Mayo Clinic first developed a system model to simulate the alveolar tissue: It comprised an open-cell-foam-filled silicon tube encapsulated in a polyethylene terephthalate container filled with thermally-polarized helium-3 up to 3 bar. The system was mechanically excited and displacement fields, induced by the propagating shear wave, were recorded by helium-3 MRE along one spatial dimension. Second, they also measured the shear stiffness of excised pig lungs at different inflation volume with standard hydrogen MRE. They showed shear stiffness increase with lung inflation. Third, they performed hydrogen MRE *in vivo* on a healthy human volunteer and showed mode-converted shear waves could be induced in the lung with an external driver placed on the subject's chest. However, these advances remained partial: First, the primary assumption of gas confinement that supports helium-3 MRE was only qualitatively tested and the test was performed in high pressure non-physiological conditions. Besides, the secondary assumption of gas content independence that would support quantitative helium-3 MRE was not challenged. Second, even though the increase of the overall pig lung shear stiffness could be checked with respect to the inflation volume, regional values did not reveal any known structures of the respiratory system, like the bronchial tree, which were expected to present higher shear stiffness than others, like the distal alveolar regions. Third, *in vivo* propagation of shear waves could be checked only at the periphery of the right lung, very close to the thoracic cage, onto which the mechanical driver was fixed. In 2008 [5], they performed hyperpolarized helium-3 MRE on excised pig lungs but the recorded high value elastograms still did not sustain the expected lung anatomy nor the values previously found by Lai-Fook *et al.* [6].

This PhD work addresses the issues raised by hyperpolarized helium-3 MRE. The required elements to probe human lungs will be presented in Chapter 1. The two techniques to be merged in this work, helium-3 MRI and lung MRE, will be introduced in Chapters 2 and 3. In Chapters 4 and 5, two elaborated experimental lung models, with liquid and solid boundaries, were developed to challenge both the validity and the sensitivity of helium-3 MRE. Primary and secondary assumptions could be tested with both helium-3 and hydrogen MRE in controlled conditions where the gas content, the inflation volume, and the position of the lungs could be varied. The viscoelastic properties of the lungs were extracted from the 3D displacement fields recorded on the gas by helium-3 MRE and on the tissue by helium-3 MRE. The reconstruction of 3D maps of dynamic and loss shear moduli benefitted here from a complete, theoretically artifact-free approach [7], which differed from the 1D reconstruction otherwise carried by Mayo Clinic.

In the course of the PhD, an original means of mechanical excitation was designed to ease and homogenize the wave propagation throughout the lungs. Based on pressure waves generated from a remote loudspeaker and guided to the buccal cavity down into the respiratory system along the airways, the system set the ground for the application of helium-3 MRE *in vivo*. Shear waves, which propagate throughout the pulmonary parenchyma where inhaled helium-3 is confined, were detected. Regional shear viscoelastic moduli, inaccessible so far, were extracted in the pulmonary parenchyma. A full protocol for helium-3 lung MRE was established and patented. In Chapter 6, helium-3 MRE was successfully performed *in vivo* on small animal and human lung.

# **Chapter 1.            Probing human lungs**

The respiratory system takes care for the introduction and ejection of gas in our body. The hardest part to study in the respiratory system are the lungs, due to the complexity of both their structure and the dynamic of their function. As the action of thoracic muscles creates negative pressure, air flows in, passing first through the nose-mouth system, and then through the larger transport airways of the lungs, the bronchial tree, before reaching the more distal alveolar regions, where oxygen and carbon dioxide are exchanged with the blood vascular system and transported throughout every organs in the body.

In this chapter, before exploring the Magnetic Resonance Elastography technique, the respiratory system will be presented and descriptions will be given for some of the most common pulmonary diseases and most common techniques used to image the lung.

## **1.1. Respiratory system and human lungs**

The human respiratory system is the integrated system of organs that promotes gas intake and allows gas exchange between the organism and the environment such that it is possible to enrich the circulatory system in oxygen ( $O_2$ ) and expel carbon dioxide ( $CO_2$ ). To achieve this double function, the gas intake travels first through the extrathoracic region (superior part of the respiratory system with the oral and nasal cavities, the pharynx, and the larynx), then through the trachea and the bronchial tree (a dichotomous structure initiated at the carina at the end of the trachea) [8]. The tracheobronchial tree ends at the terminal bronchioles, which lead to the alveoli, where gas exchange with the lung capillaries can occur. The region from the terminal bronchioles to the alveoli is called lung parenchyma (Fig. 1. 1).

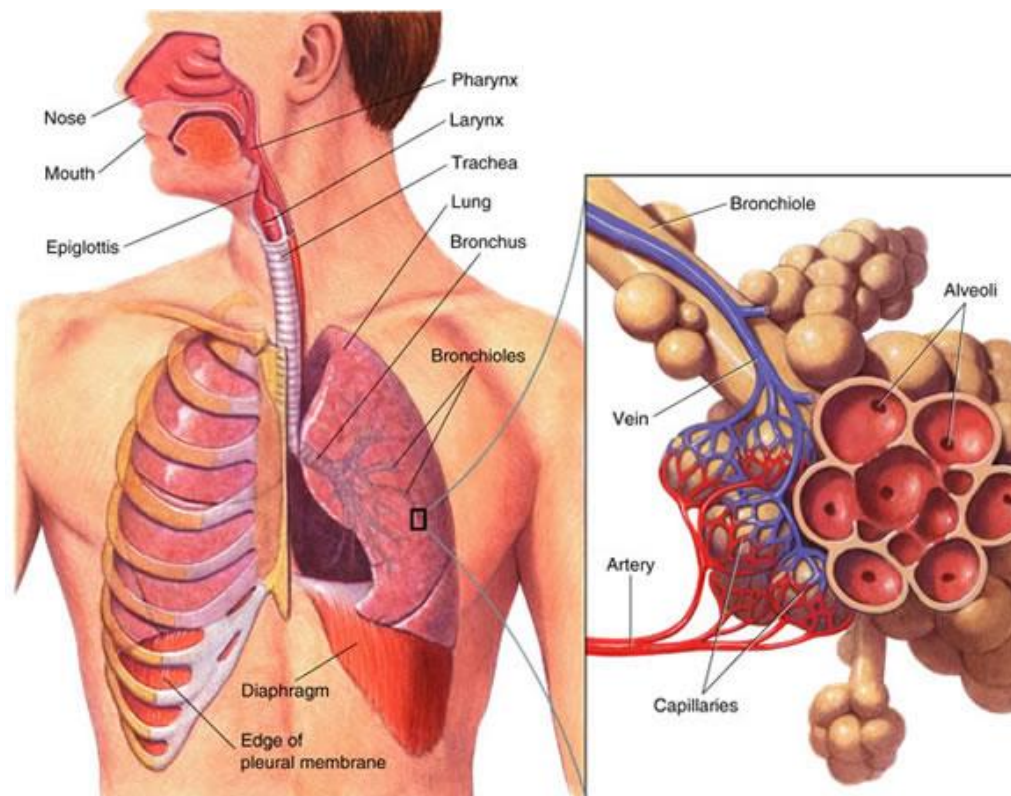


Fig. 1. 2: The respiratory system is divided into the upper airways, the extrathoracic region down to the epiglottis, the central airways defined by the tracheobronchial tree, and the distal airways, the alveolar region, where gas exchange finally takes place. (Extracted from [www.goldiesroom.org](http://www.goldiesroom.org)).

### 1.1.1. Anatomy

#### 1.1.1.1. The extrathoracic region

##### 1.1.1.1.1. The nasal and oral cavities

The gas entering the respiratory system during breathing passes first through the nasal cavity, where, thanks to the large surface of the nasal conchae, it is brought to a temperature very close to that of the body. During this passage, the air is also humidified and cleaned from dust and other particulate matter by the vibrissae, which are short and thick hairs present in the vestibule. These filtered impurities then move towards the pharynx and into the esophagus and they are digested in the stomach [9].

The oral cavity is bounded laterally and in the front by the alveolar arches with their contained teeth; behind, it communicates with the pharynx by a constricted aperture termed the isthmus faucium. It is roofed in by the hard and soft palates, while the greater part of the floor is formed by the tongue, the remainder by the reflection of the mucous membrane from

the sides and under surface of the tongue to the gum lining the inner aspect of the mandible. It receives the secretion from the submaxillary and sublingual salivary glands.

#### 1.1.1.1.2. The Pharynx

The pharynx is the part of the throat situated immediately inferior to the mouth and nasal cavities, and superior to the esophagus and larynx. The human pharynx is conventionally divided into three sections:

- nasopharynx (epipharynx)
- oropharynx (mesopharynx)
- laryngopharynx (hypopharynx).

The pharynx is part of the digestive and the respiratory systems; it is also important in vocalization.

#### 1.1.1.1.3. The Larynx

The larynx is an organ involved in breathing, sound production (it houses the vocal folds), and protecting the trachea against food aspiration. The vocal folds are situated just below where the tract of the pharynx splits into the trachea and the esophagus. The main function of the larynx is the generation of the sound since it is here where the pitch and the volume are manipulated. During swallowing, the backward motion of the tongue forces the epiglottis over the glottis opening to prevent swallowed material from entering the larynx which leads to the lungs; the larynx is also pulled upwards to assist this process (Fig.1. 1).

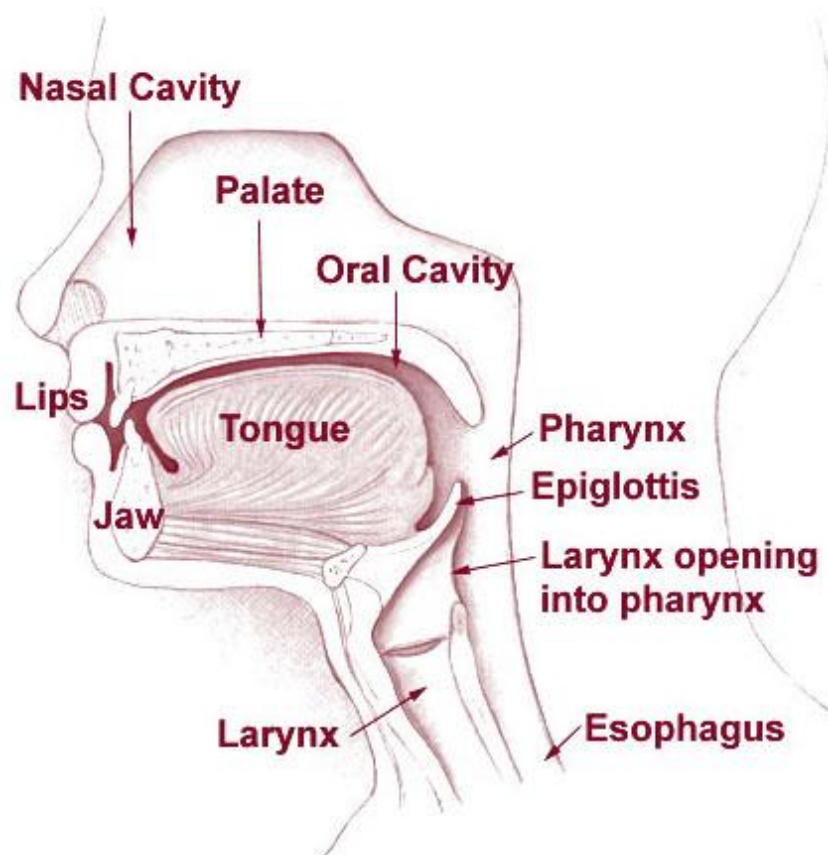


Fig.1. 1: Schematic view of the extrathoracic region in the respiratory system (Extracted from iahealth.net).

#### 1.1.1.2. The tracheobronchial and alveolar regions

##### 1.1.1.2.1. The tracheobronchial regions

The tracheobronchial tree, consisting in the first 14 to 16 bronchi generations (Fig.1. 1), is the structure from the trachea, bronchi, and bronchioles, which forms the airways that supply gas to the lungs. It fits within the neck and the chest. The structure looks like a tree because the trachea splits into the right and left main stem bronchi, which dichotomously branch into progressively-smaller structures. The lining of the tracheobronchial tree consists of ciliated columnar epithelial cells. Structurally, the trachea and the bronchi are similar, with cartilaginous rings linked to each other by a fibrous layer, and transversally by smooth muscle fibers on the extremities. The cartilages are present down to the bronchioles and the terminal bronchioles, which assure the transition towards the alveolar regions. Injuries to the tracheobronchial tree are potentially fatal because they can interfere with breathing [10]. As one goes deeper down the airway tree, the amount of cartilage decreases as the amount of smooth muscle increases.

### 1.1.1.2.2. The distal pulmonary regions

The lung distal region contains the 16<sup>th</sup> to 23<sup>th</sup> generations corresponding to the respiratory region (Fig.1. 2).

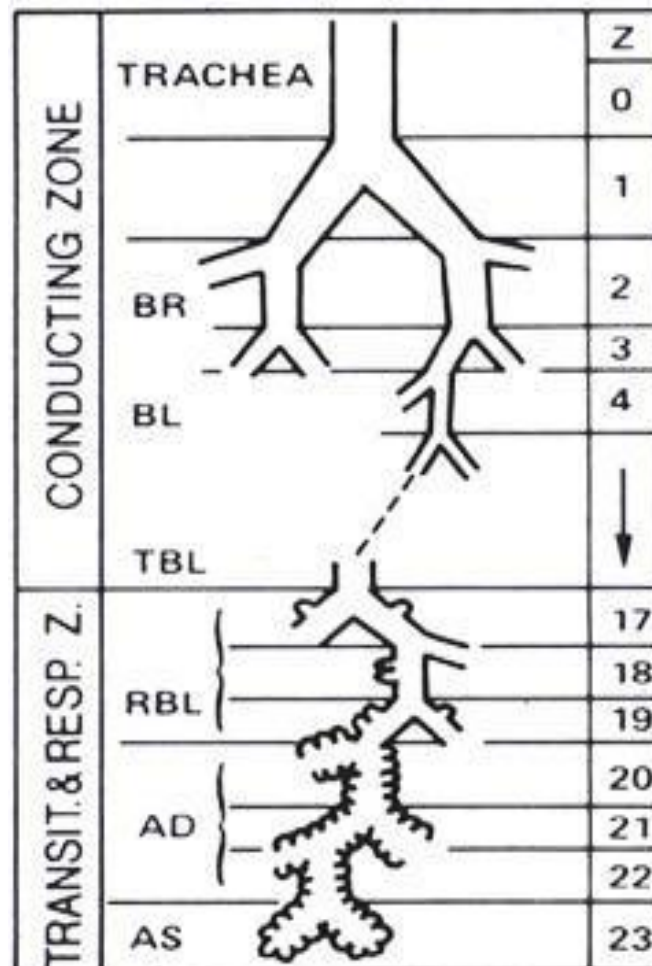


Fig.1. 2: Weibel's model of the tracheobronchial and alveolar regions [11] schematic extracted from [12]. From the trachea down to the 14<sup>th</sup> to 16<sup>th</sup> bronchial generations, the conducting zone of the respiratory system leads to the transitory and respiratory zone down to the 23<sup>rd</sup> generation, where the effective gas exchange takes place. (BR: bronchi, BL: bronchioles, TBL: transition bronchioles, RBL: respiratory bronchioles, AD: alveolar ducts, AS: alveolar sacs)

In this region, the distal bronchioles give rise to alveolar ducts which terminate in alveoli [13]. The set of distal bronchioles, alveolar ducts, and sacs defines the pulmonary parenchyma (Fig.1. 2). Here, the muscles are replaced by the collagen and elastin fibers. The elastin fibers allow the alveoli to stretch as they are filled with oxygen-rich gas during inhalation. They then spring back during exhalation as the carbon dioxide-rich gas is expelled [14].

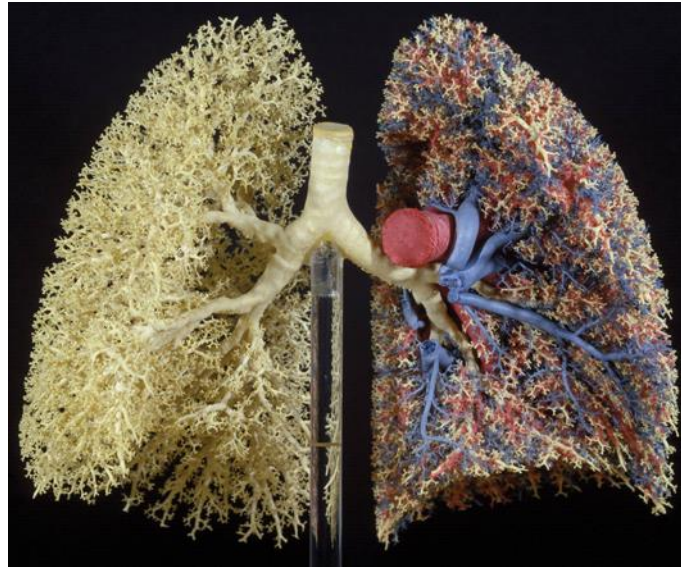


Fig.1. 3: Cast of the airways (yellow), the pulmonary arteries (red), and veins (blue) of a human lung (Extracted from Dr Ewald R. Weiber [15]).

A typical pair of human lungs (Fig.1. 3) contains about 700 million alveoli, with an average diameter of  $200\ \mu\text{m}$ , producing  $90\ \text{m}^2$  of surface area. Each alveolus is wrapped in a fine mesh of capillaries covering about 70% of its area, which yields more than  $60\ \text{m}^2$  of effective surface area for gas exchange. It is inside the alveolar respiratory units, where the gas moves in and out of the alveoli via the bronchial tree, and through the thin epithelial cells of the alveoli that gas exchange with blood occurs (Fig.1. 4). As blood moves through the capillaries in the alveolar walls, it picks up oxygen and releases carbon dioxide. The major cell types in the alveolar wall are:

- Type I squamous alveolar cells, which form the structure of an alveolar wall
- Type II great alveolar cells, which secrete pulmonary surfactant to lower the surface tension of water and allow the membrane to separate, therefore increasing its capability to exchange gases [16]. Surfactant, continuously released by exocytosis, eases the re-inflation of the alveoli.
- Macrophages that destroy foreign material, such as bacteria.

The gas exchange area may reach 130 m<sup>2</sup>, and the respiratory and vascular structures associated with it handle a volume of 12 000 L of filtered air and 6 000 L of perfused blood per day.

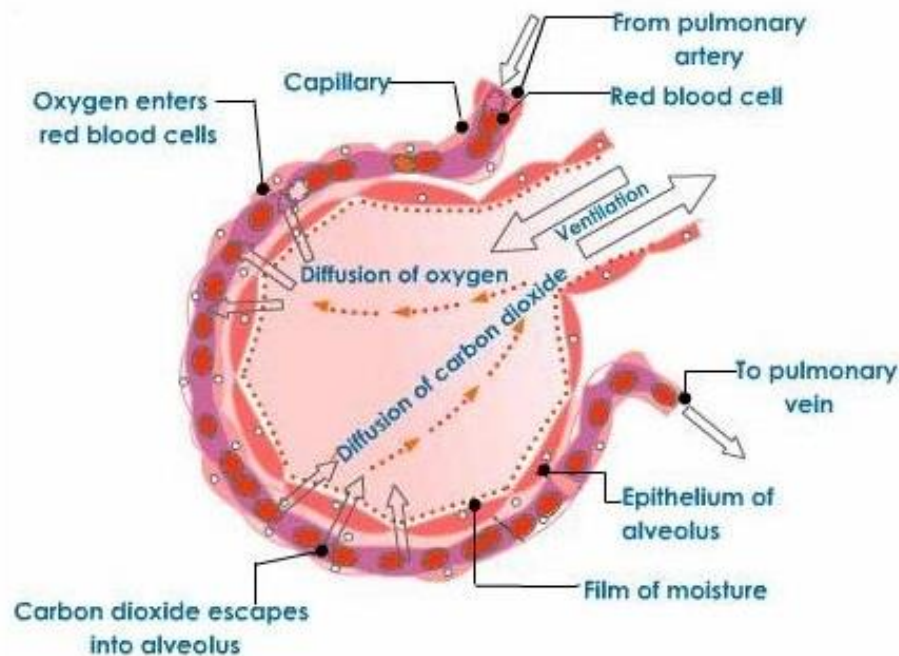


Fig.1. 4: Ventilation is the process of air movement into and out of the lungs. Once air enters the lungs, diffusion of O<sub>2</sub> and CO<sub>2</sub> occurs in the alveoli. The oxygenated blood is then perfused throughout the body where gas exchange occurs in the capillary beds. (Extracted from [17])

### 1.1.2. Diseases

Lung diseases are characterized by underlying acute and sometimes chronic inflammation. Consequently they are associated with structural changes referred as remodeling. When affected by a pulmonary disease, the tissue and structure of the lung are subjected to important changes, which mostly impact the mechanical properties of the parenchyma. The main components of pulmonary connective tissue are collagen and elastin fibers. Each tissue type has different mechanical properties. Thus their combination determines the resulting mechanical properties of the lung. These fibers form a continuous network throughout the lung and determine the passive respiration. Diseases, which alter the mechanical properties of the lung, directly act on these fibers, consequently changing both elastic and dissipative forces. The mechanical properties of the lung tissue represent an essential factor for determining the state of the organ. Here, I am not going to make an exhaustive disquisition on pulmonary pathology, nevertheless I will describe the most common and widespread obstructive and restrictive diseases that affect the lung. If we look at the lung as split into two

main parts, airways and alveoli, lung diseases could be associated to where they are localized, so that asthma and chronic bronchitis concern the airways while emphysema and interstitial lung diseases affect the alveolar and pulmonary parenchyma.

#### 1.1.2.1. Asthma

Asthma is a chronic, long-term, reversible obstructive lung disease that inflames and narrows the airways. It is characterized by rapid and important variations of the airways resistance, due to:

- Muscle contraction around the bronchi
- Wall edema and congestion of the bronchi
- Total obstruction of the bronchi by mucus

Hence the expiration becomes more difficult. As the residual volume gets higher, lung is more distended so is the total lung capacity and the lung works with an elevated volume.

It causes recurring periods of wheezing (a whistling sound when the subject breathes), chest tightness, shortness of breath, and coughing. The coughing often occurs at night or early in the morning. Asthma affects people of all ages, but it most often starts during childhood. Asthma has no cure, and even when you feel fine, you still carry the disease and it can flare up at any time. However, with today's knowledge and treatments, most people who have asthma are able to manage the disease and they can live normal, active lives and sleep through the night without interruption from asthma. As of 2010, 300 million people were affected worldwide [18]. In 2009, asthma caused 250,000 deaths worldwide [19].

##### 1.1.2.1.1. Tissue mechanics in asthmatic lung

Asthma is characterized by reversible airway obstruction, airway hyper responsiveness, and airway inflammation. As in many chronic inflammatory disorders, asthmatic airway inflammation yields tissue injury and subsequent structural changes [20]. Lung biopsies provide evidence that asthmatic inflammatory processes affect the lung parenchyma [21] and that the mechanical stress developed during asthmatic bronchoconstriction may also induce remodeling.

---

#### 1.1.2.1.2. COPD: Chronic Obstructive Pulmonary Diseases

Chronic obstructive pulmonary diseases (COPD) are lung diseases characterized by chronic obstruction of lung airflow that interferes with normal breathing and that is not fully reversible. In this group of diseases, chronic bronchitis and emphysema are the most frequent ones. These diseases are characterized by a reduction of the bronchial lumen in small airways but also by a loss of lung elasticity, with the manifestation of emphysema. It is one of the most common obstructive disease affecting both airways and alveoli. COPD is not simply a "smoker's cough" but an under-diagnosed, life-threatening lung disease [22].

##### Chronic bronchitis

Lung damage and inflammation in the large airways results in chronic bronchitis, defining a cough with sputum production during most of the days for 3 months in a year, for 2 consecutive years [23]. The main characteristic of this disease is the increased number (hyperplasia) and increased size (hypertrophy) of the goblet cells and mucous glands of the airway. This yields narrowing of the airways. Microscopically there is infiltration of the airway walls with inflammatory cells, followed by scarring and remodeling of the wall thickness resulting in airway narrowing.

##### Emphysema

The most important COPD disease is emphysema, a long-term, progressive and irreversible disease of the lungs that primarily causes shortness of breath. In people with emphysema, proximal airways and alveolar lung tissues necessary to support the physical shape and function of the lungs are destroyed, causing enlarged distal airspaces. The primary causes are tobacco [24] and long-term exposure to air pollution. Emphysema may be classified in:

- Panacinar (or panlobular) emphysema, where the area from the respiratory bronchioles to alveoli has expanded. It occurs commonly in the lower and in the anterior margins of the lungs.
- Centriacinar (or centrilobular) emphysema, where the proximal and central parts of acini have expanded, while the distal alveoli are unchanged. It more commonly occurs in the upper lobes.

When the airspaces are enlarged, their compliance increases and they inflate more easily than normal acini. Thereof, the lung is more distended and the inflated air preferably ventilates the emphysematous airspaces.

#### Tissue mechanics in emphysematous lung

Several studies suggest that, in an emphysematous lung, elastin constitutes the major target of destruction; moreover, pathophysiological changes can also result from some abnormalities in collagen matrix [25]. While collagen is stiffer and with higher failure threshold than elastin, protecting lung from rupture at high volume, in an emphysematous subject, alveolar walls failure suggest that collagen network is not normal. Elastin and collagen are the major constituents of the extracellular matrix. They determine the viscoelastic properties of the lung tissue. In normal breathing, the elastic recoil of the lung is governed by the nonlinear stress-strain properties of lung tissue [26], while the stress-bearing elements are collagen and elastin fibers [27]; between the two, elastic fiber acts more linearly than the collagen ones [28]. The hysteresivity<sup>1</sup> of the lung could be an important parameter for characterizing the state of the lung as it depends on the transpulmonary pressure and the collagen content. For a healthy subject, when the transpulmonary pressure increases, the hysteresivity decreases whereas, for an emphysematous subject, the hysteresivity remains constant for any transpulmonary pressure. It results from the inability of the lung to get deflated. In a healthy subject, the elastin-collagen ratio is positively correlated with the hysteresivity whereas, in an emphysematous subject, both hysteresivity and collagen content increase, while failure stress decreases. This means that, in an emphysematous subject, the alveolar walls and the collagen fibers become weaker, and the degradation of collagen and elastin leads to the remodeling and the loss of elastic recoil of the alveolar walls, which fail under a weaker stress. [29] [30].

---

<sup>1</sup> Hysteresivity takes its meaning from ‘hysteresis’ and it means lag. It is related to the behavior of not returning to its original state.

### 1.1.2.1.3. DPLD: Diffuse Pulmonary Lung Diseases

Diffuse parenchymal lung diseases (DPLDs) consist of disorders by known causes (collagen-vascular, environmental, or drug related origins) as well as disorders by unknown causes (including idiopathic interstitial pneumonias, granulomatous lung disorders, and other forms of interstitial lung diseases, ILD), since available data suggest that no single etiologic agent serves as a common inciting event in the pathogenesis of idiopathic pulmonary fibrosis (Fig.1. 5). The latter refers to a group of lung diseases affecting not only the interstitium (the tissue and space around the air sacs of the lungs) [31], but also alveolar epithelium, pulmonary capillary endothelium, basement membrane, perivascular and perilymphatic tissues. The group of idiopathic interstitial pneumonias includes nonspecific interstitial pneumonia, desquamative interstitial pneumonia, respiratory bronchiolitis-associated interstitial lung disease, acute interstitial pneumonia, cryptogenic organizing pneumonia, and lymphocytic interstitial pneumonia [32] (see DPLD diagram Fig.1.6).

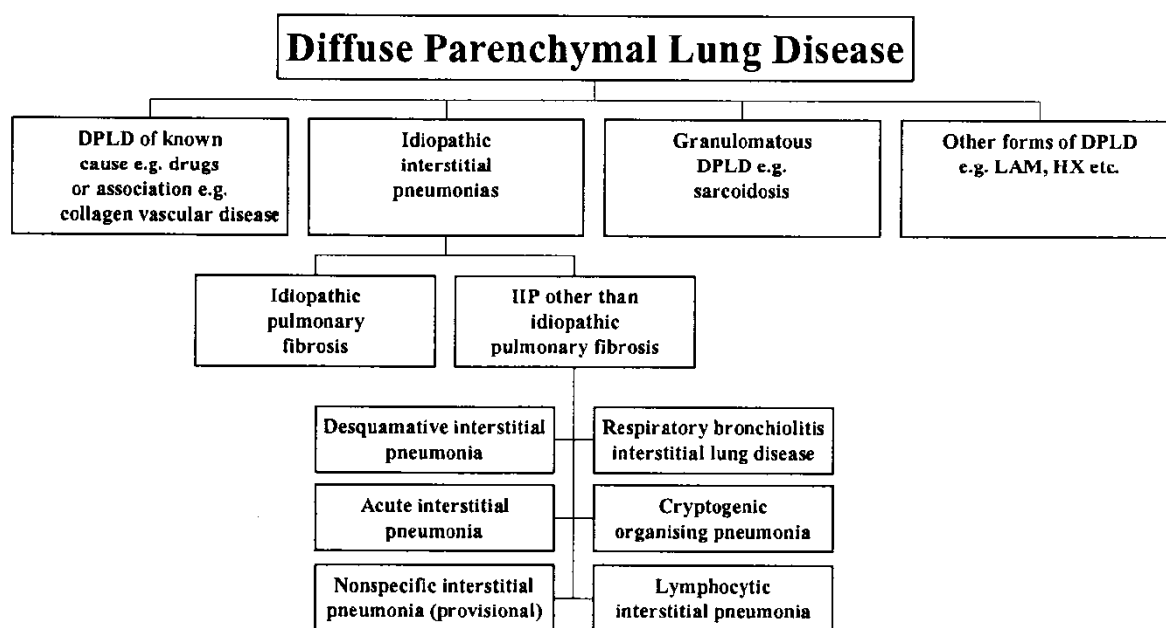


Fig.1. 5: Diffuse Parenchymal Lung Diseases. When the cause is unknown, there are three categories of possible DPLDs: idiopathic interstitial pneumonias, granulomatous lung disorders, and other forms of interstitial lung disease including lymphangioleiomyomatosis pulmonary Langerhans cell histiocytosis/histiocytosis X (HX), and eosinophilic pneumonia. The most important distinction among the idiopathic interstitial pneumonias is between idiopathic pulmonary fibrosis and other interstitial pneumonias [32].

There are several causes of interstitial lung diseases that allow classification of these diseases [33]:

- Inhaled inorganic and organic substances

- Drugs
- Connective tissue disease
- Infection
- Idiopathic
- Malignancy

Idiopathic interstitial pneumonia is one of the most common DPLD group of interstitial lung diseases.

#### 1.1.2.1.4. Idiopathic pulmonary fibrosis

Idiopathic pulmonary fibrosis (or idiopathic fibrosis interstitial pneumonia) is a chronic, progressive form of lung disease characterized by fibrosis of the supporting framework (interstitium) of the lungs. By definition, the term is used only when the cause of the pulmonary fibrosis is unknown ("idiopathic"). It primarily occurs in older adults and it is limited to the lungs.

The period for diagnosing the idiopathic pulmonary fibrosis is quite long, by a median of 1-2 years [34]. It gradually starts with dyspnea, a nonproductive cough during the first 6 months. A chest radiograph typically reveals diffuse reticular opacities but as it lacks diagnostic specificity and it is necessary to investigate deeper by other exams [32]. High-resolution computed tomography (HRCT) findings are significantly more sensitive and specific for the diagnosis of idiopathic pulmonary fibrosis. On HRCT images, usual interstitial pneumonia is characterized by the presence of reticular opacities often associated with traction bronchiectasis. As idiopathic pulmonary fibrosis progresses, honeycombing becomes more prominent [35] and the pulmonary function tests often reveal restrictive impairment and reduced diffusing capacity for carbon monoxide. The previous pathogenesis theory of the generalized inflammation progressing throughout the lung parenchyma is now replaced by the belief that epithelial injury and activation in fibroblast foci are crucial early events, which trigger a cascade of changes leading to reorganization of pulmonary tissue compartments [36].

#### 1.1.2.1.5. Tissue mechanics in fibrotic lungs

Pulmonary fibrosis is characterized by abnormal lung physiology and by the excessive production of extracellular matrix molecules such as collagen, elastin, and proteoglycans. In a fibrotic patient, during breathing, the lung is more resistive and the shape of the lung

---

pressure-volume curve is subjected to several modifications [37]. The tissue mechanical behavior is correlated with lung parenchyma inflammation and remodeling, characterized by a process of fibroelastosis. It obviously supports the idea that tissue mechanical properties are central in the lung function as they characterize the viscoelastic system and its specific components [38]

#### 1.1.2.2. Diagnosis of pulmonary diseases

The diagnosis of a pulmonary disease is not a very simple process as there are different kinds of tests to perform before narrowing down the possibilities. First, generic tests are performed by physical examination, auscultation, and pulmonary function tests, like spirometry. However, these tests remain essentially global and qualitative. They allow in most cases to monitor the organ functioning, but they do not furnish any regional nor quantitative data about the state of the lung. Second, specific imaging techniques, like chest radiography, X-ray Computed Tomodensitometry (CT), scintigraphy, or Positron Emission Tomography (PET) are performed to establish the ultimate diagnosis with consistent clinical features before prescribing a biopsy.

### 1.2. Diagnostic tool and imaging techniques

#### 1.2.1. Auscultation

Auscultation, performed with a stethoscope, is based on listening to the internal sounds of the body. Its main purpose is examining the circulatory system and respiratory system (heart sounds and breath sounds), as well as the gastrointestinal system (bowel sounds). To perform auscultation, it is necessary to possess substantial clinical experience, a fine stethoscope and good listening skills. When auscultating the lungs, breath sounds such as wheezes, crepitations, and crackles may be identified. As it is not based on an imaging method, this subjective technique does not furnish any visual information. As it is dependent upon the doctor's skill of listening and clinical experience, auscultation is able to give some local but not quantitative information about the state of the lung.

#### 1.2.2. Pulmonary function test

The most common pulmonary function test is spirometry, which is measuring lung function as the amount (volume) and speed (flow) of gas that can be inhaled and exhaled. Spirometry

is an important tool used for generating pneumotachographs, which are helpful in assessing the subject's conditions with respect to asthma, pulmonary fibrosis, cystic fibrosis, or COPD. Even though the technique is the best standard for COPD diagnosis, it is unable to furnish a quantitative assessment and a differentiation of the factors involved in the disease. The maneuver has several limitations: First, it must be repeated at least three times to assure the reproducibility; then it highly depends on the patient's collaboration and effort (including children old enough to comprehend what to do and people able to understand and follow instructions). Overall, the forced volume vital capacity (FVC) can only be underestimated, never overestimated, by pulmonary function tests (Fig.1. 6). Another major limitation is the fact that many intermittent or mild asthmatics have normal spirometry between acute exacerbation, limiting spirometry for monitoring rather than for diagnosing.

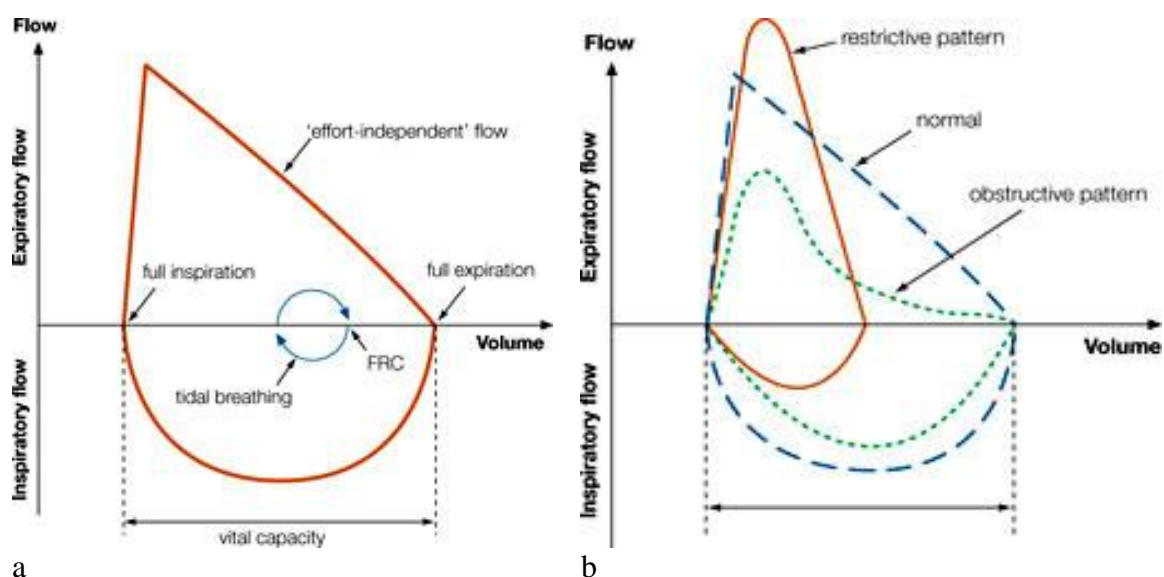


Fig.1. 6: Spirometry furnishes the forced vital capacity (FVC) and the forced expiratory volume in one second ( $FEV_1$ ) measurements, related to sex, age, and height. Spirometry is a very useful tool to exhibit ventilation deficits. (a) Typical pneumotachograph for a healthy subject. (b) Typical pneumotachograph for patients: in a subject with obstructive defect, such as asthma, the expiration flow decreases with respect to the healthy subject (green dotted line) while in subjects with restrictive pattern, such as fibrosis (red continuous line), the inspiration volume is drastically reduced (Extracted from [www.prahranmarketclinic.com](http://www.prahranmarketclinic.com)).

### 1.2.3. Imaging techniques

#### 1.2.3.1. Radiography

Using X-rays, radiography reveals the different tissue densities of the human body. Generated X-rays are effectively attenuated on their way through the body according to the density of

the tissues they cross. Hence a chest X-ray results in a 2D projected representation of all the structures superimposed on each other (Fig.1. 7).

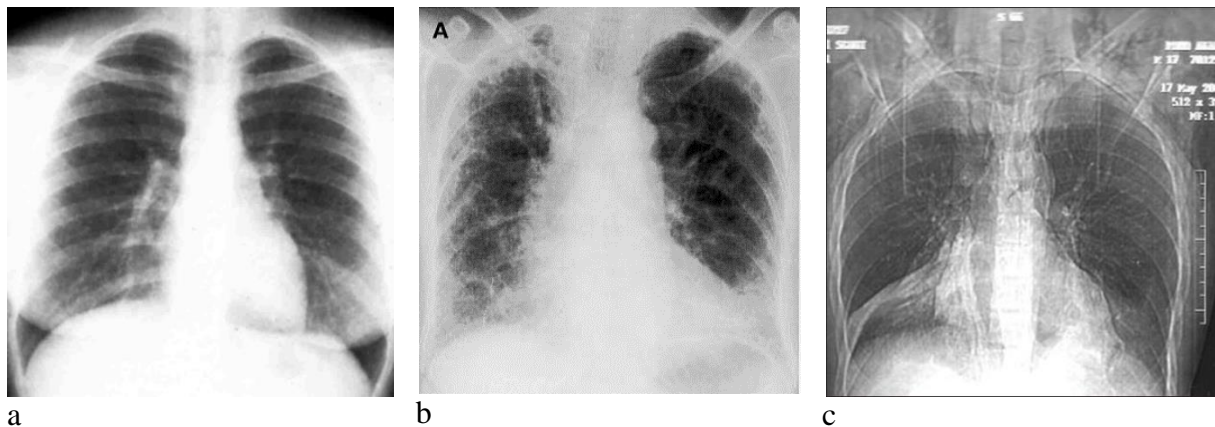


Fig.1. 7: (a) Chest X-ray, a 2D radiographic image of healthy lungs (extracted from [39]). (b) X-ray of an idiopathic pulmonary fibrotic patient with a peripheral reticular opacity (marked at the bases) with honeycombing. In idiopathic patients, chest X-ray sometimes could appear normal (Extracted from [32]). (c) Chest X-ray of an emphysematous patient, with an extensive subcutaneous emphysema and pneumomediastinum (Extracted from [40]).

#### 1.2.3.2. X-ray computed tomodensitometry

An X-ray computed tomodensitometry (CT scan) is a computerized tomography scan. It provides 3D detailed images of the human body with sub-millimeter spatial resolution. The CT scanner consists of an X-ray tube that rotates around the body while the patient is continuously moved through this rotating beam. Transmitted X-rays are analyzed by a detector on the opposite side of the subject's body. The images produced by a CT scan, called tomograms (Fig.1. 7) and more detailed than standard projection X-rays, reveal the 3D structures of internal organs, blood vessels, bones, and tumors. However, a CT scan does expose the patient to a radiation dose that is greater than for standard X-rays. Besides, CT scan can only provide a morphological image of the organ, in a short time, without any possibility to extract its functional information. Among its numerous application, it is used to diagnose emphysema in its late stages.

#### 1.2.3.3. Ultrasound imaging

In lung diagnosis, ultrasound imaging is employed only to study pleura since in the lung the water-air interfaces reflect the ultrasound waves and make impossible to properly probe the lung parenchyma [39] (Fig. 1. 3).

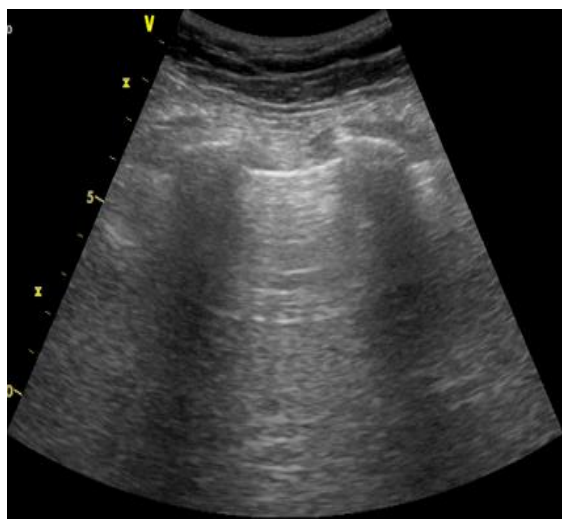


Fig. 1. 3 Ultrasound imaging of the lungs

In the figure the two rib shadows underline the image in the lungs and in between them the pleural line. Since the two ribs appear as two wings, it is usual to call it the 'bat sign' [41].

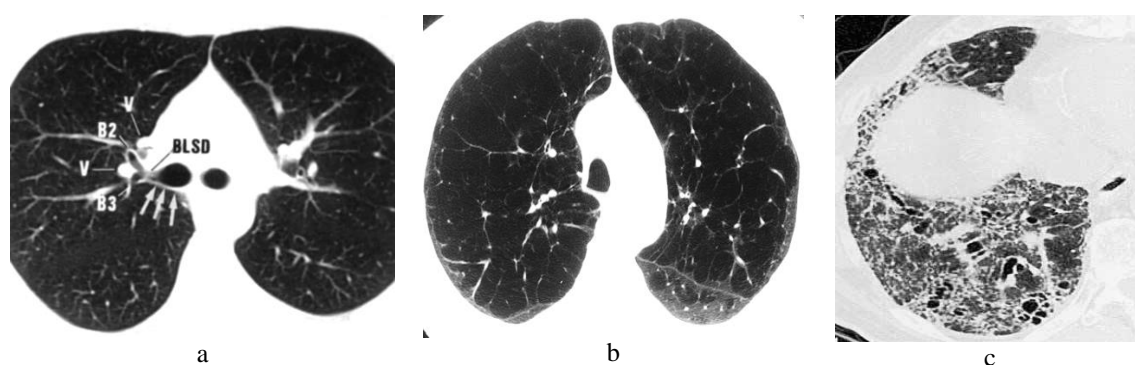


Fig.1. 8: Thorax X-ray computed tomodensitometry (a) for a healthy subject (Extracted from [39]), (b) for an emphysematous patient, with the evident destruction of the alveolar structure with the consequently loss of the elastic recoil (Extracted from [42]), (c) for a fibrotic patient, in which the severity of the disease is evident by the reticular abnormality (Extracted from [32]).

In the diagnosis of diseases like asthma, CT-scan imaging is a useful tool to detect bronchoconstrictions, while, in COPD, it is used to assess and to differentiate the disease involved factors [22]. However, a great limitation is the fact that this technique is effective only in an advanced stage of the disease. Disease-related changes cannot be detected at an early stage and proper diagnosis is not possible (Fig.1. 8). The lack of sensitivity for the tissue state does not allow to follow up drug treatment or disease progression where morphological changes may be inexistent. Early detection of pulmonary diseases is a key issue for advanced imaging techniques like the one developed in this PhD work.

#### 1.2.3.4. Scintigraphy

Scintigraphy provides 2D images of the lungs. The emitted radiation is recorded by an array of gamma cameras to form two-dimensional images Fig.1. 9. Lung scintigraphy may be used

to diagnose pulmonary embolism, to evaluate lung transplantation, before and after an operation, or to evaluate right-to-left shunts. Scintigraphy may also provide 2D maps of ventilation/perfusion ratios according to the administered tracer. During the ventilation phase, gaseous xenon-133 or nebulized technetium-99m radionuclide is inhaled by the patient through a mouthpiece or a mask. During the perfusion phase, radioactive technetium macro aggregated albumin is intravenously injected into the patient.

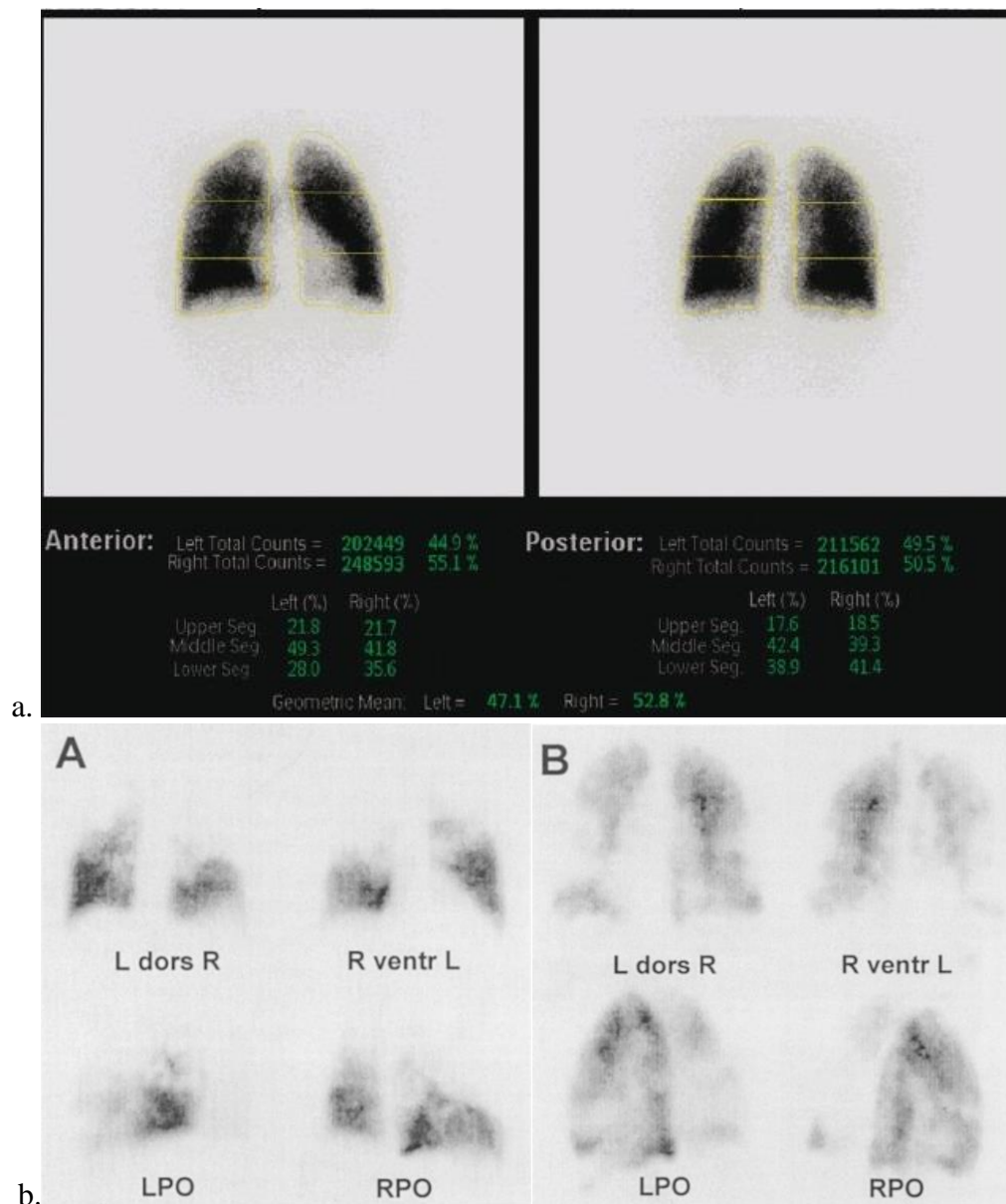


Fig.1. 9: (a) Perfusion scintigraphy image (extracted from [43]) in a healthy subject, in which the quantitative perfusion analysis reveals a contribution of 53% for the right lung and of 47% for the left lung in the total pulmonary perfusion. (b) Perfusion scintigraphy of an emphysematous patient posterior-anterior, anterior-posterior, and left and right posterior oblique views (extracted from [44]), showing a typical perfusion heterogeneity due to the disease.

The sensitivity of scintigraphy and more generally of nuclear medicine is very good but it is unfortunately limited in terms of spatial and temporal resolutions as well as by patient exposure to radiation (75 times more than the X-ray exposition). It generally reaches the centimeter in a dozen of minutes.

#### 1.2.3.5. SPECT

Single-photon emission computed tomography (SPECT) is a nuclear medicine tomographic imaging technique using gamma rays. It is very similar to conventional nuclear medicine planar imaging using a gamma camera but it provides 3D information. This information is typically presented as cross-sectional slices through the patient, but can be freely reformatted or manipulated as required. Like for lung scintigraphy, the basic technique requires inhalation or injection of a gamma-emitting radioisotope. SPECT can be applied to provide 3D representations of tumors, infections, or bones.

This imaging technique allows to obtain functional information from the inner body (Fig.1. 10), but it is very sensitive to motion artifacts or to non-uniform distribution of the radio tracer. Many image processing techniques have been developed to cope for this limitation. Motion artifacts are very frequent as the acquisition time is quite long for the patient (45 min). SPECT images reflect averages over numerous breathing cycles. Very often, SPECT is associated with a CT scan for merging anatomical and functional information (Fig.1. 11). It also contributes to discriminate between false positive and false negative findings.

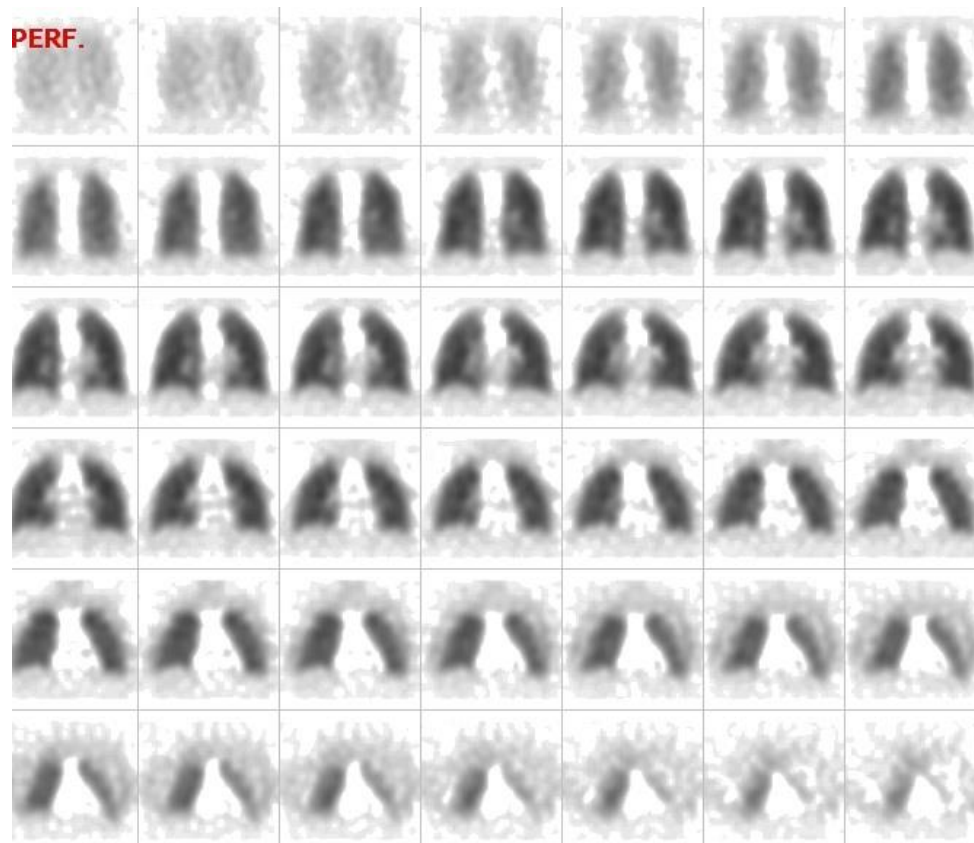


Fig.1. 10: SPECT perfusion images in a healthy subject (Extracted from [www.nuclearimaging.com.au](http://www.nuclearimaging.com.au)).

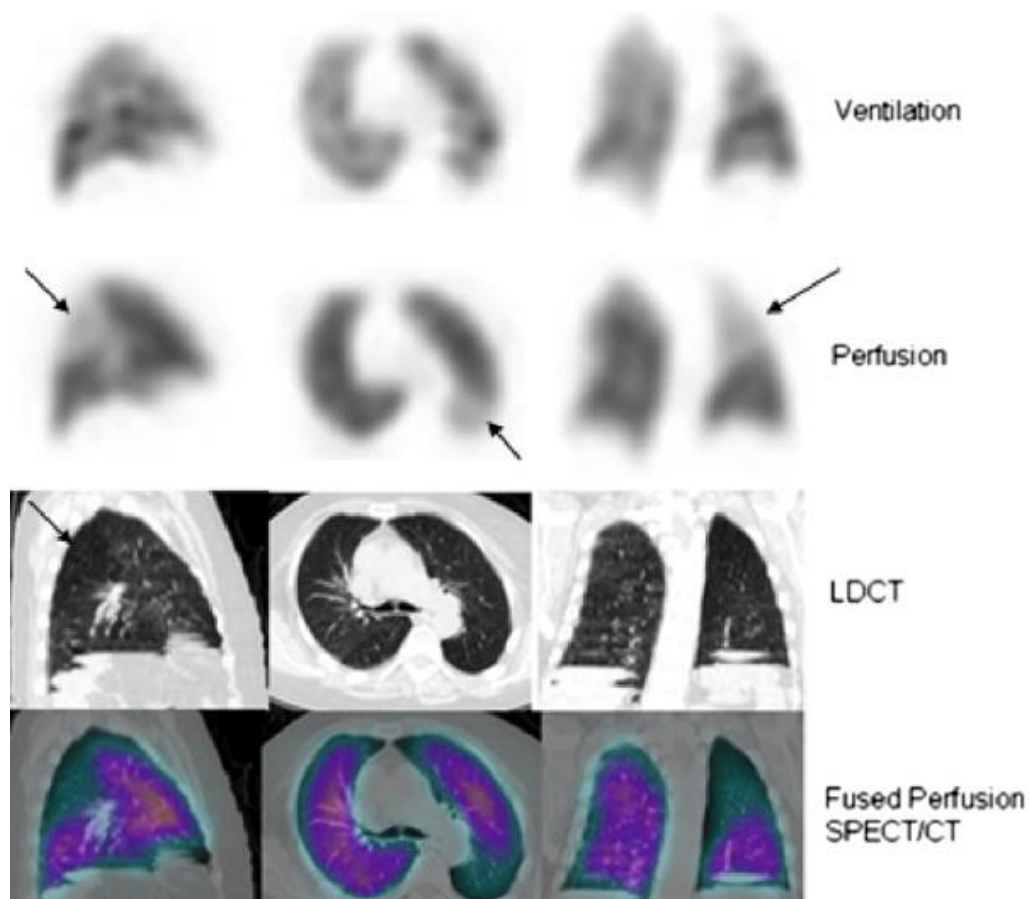


Fig.1. 11: (Top) SPECT images in an emphysematous patient. Functional information is provided both by ventilation and perfusion SPECT imaging (here non-homogenous lung ventilation and a large perfusion defect are revealed). (Bottom) Co-registered SPECT-CT images in an emphysematous patient (reduced perfusion area) where functional information corroborates anatomical information in the lung (Extracted from [45]).

#### 1.2.3.6. PET

Positron emission tomography (PET) measures 3D metabolic activity of an organ through the emissions produced by positrons from the decay of a radiolabelled material previously injected like fluorodeoxyglucose (FDG). Perfusion and ventilation may be studied with radioactive nitrogen when it passes in the respiratory airways [46]. Like SPECT, PET provides processed functional maps of the body's inner organs that can be fused with a co-registered morphological CT scan (Fig.1. 12). One of the most frequent use is therapy response and especially tumor therapy response. Therefore, oncology is one of the most important application for PET. However PET presents a rather low spatial resolution so it is difficult to detect tumors smaller than a centimeter and false negatives, or the contrary, false positives due to inflammation, are common findings.

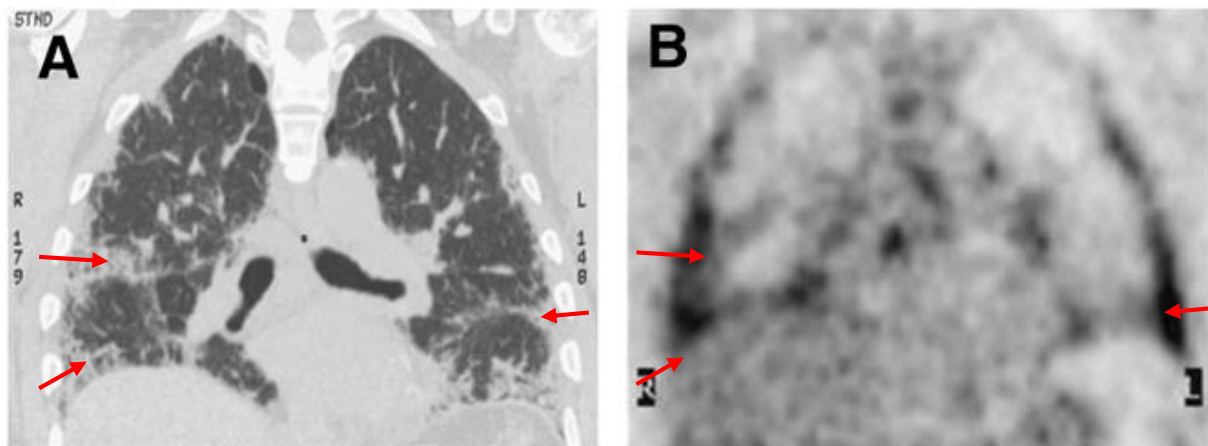


Fig.1. 12: (A) Lung CT scan (B) Lung PET image on a patient with pulmonary fibrosis. The parenchymal abnormalities on the CT scan image are reflected on the PET image, where the black areas are predominant (Extracted from [47]).

#### 1.2.3.7. Hydrogen magnetic resonance imaging of the lung

As the lung is made primarily of gas (roughly 90%) and secondarily of tissue, the organ hydrogen content is weak. Moreover the lung has irregular movements and contains 70-100 m<sup>2</sup> of tissue-air interfaces. So the signal obtained by standard MRI is very low. This technique is not often used to study the pulmonary parenchyma, but since it allows to detect tumors and ganglions it is used for the exploration of these masses [39]. Nevertheless, pulmonary perfusion MRI, without any administration of contrast agent but spin tagging, allows to obtain vascularization and real perfusion images (Fig. 1. 4). Ultra-short echo time (UTE) sequences hold today the promise to circumvent some of the limitations of standard MRI in the lung.

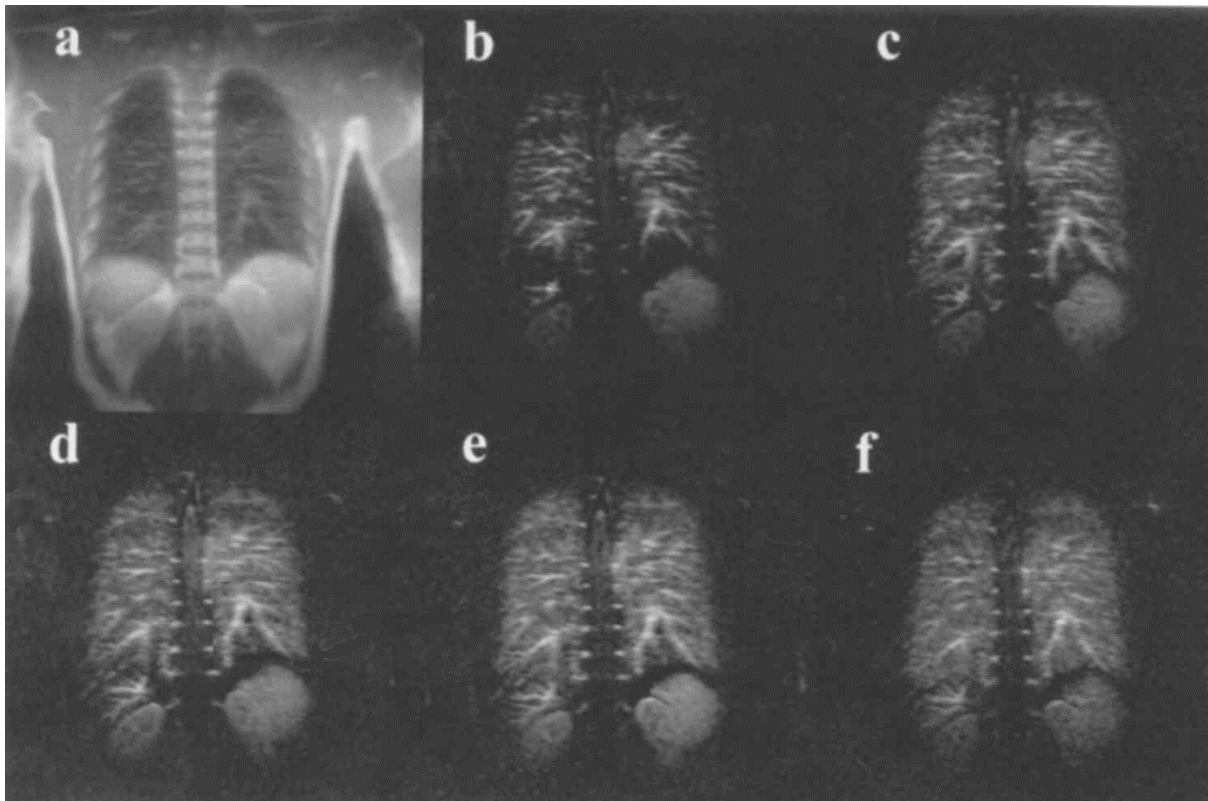


Fig. 1. 4 : Pulmonary perfusion MRI by spin tagging in a healthy volunteer without contrast agent. The reference image (a) is followed by the functional images (b-f) acquired after applying different inversion pulses [48].

All the aforementioned techniques furnish morphological or functional information about the lung. Hydrogen lung MRI, as said, is not very useful for the lack of signal but MR perfusion imaging application could be used combined with other techniques. For emphysema for example, when combining hydrogen MRI with CT scan, it is possible to follow the evolution of the disease and to evaluate the treatment outcomes [49].

Nevertheless, none of those diagnosis techniques furnishes quantitative regional information about mechanical properties of the lung. Elastography may cope for this lack of non-invasive technique as it directly tackle the problem by mapping *in vivo* the viscoelastic properties of tissues (Chapter 3). Ultrasound elastography is not a good candidate to address the issue as, due to large air-tissue mismatches within the lung, it provides useful information only at the surface of the body. Magnetic resonance elastography seems to be the solution to overcome these limitations (Chapter 3). By administering hyperpolarized gas as a tracer in the lung to cope for the lack of hydrogen MR signal, Magnetic resonance elastography may turn out to be an optimal tool to probe the mechanical properties of the lung. (Chapter 2).

## **Chapter 2.           Hyperpolarized helium-3 Magnetic Resonance Imaging**

Based on Nuclear Magnetic Resonance (NMR), Magnetic Resonance Imaging (MRI) is a powerful tool in the fields of physics, biophysics, chemistry, or biochemistry. It allows imaging of gases, liquids, and solids by probing the quantum properties of atomic nuclei. Firstly described by Isidor Rabi in 1938 [50], NMR was expanded in 1946 by Felix Bloch and Edward Mills Purcell for use on liquids and solids [51]. In 1973, the first two-dimensional (2D) image was acquired thanks to the introduction of spatial encoding by the addition of readout gradients. Three-dimensional (3D) imaging could be later achieved by adding phase encoding and slice selection gradients. It led to signal analysis by Fourier Transform [52], [53]. Rapidly relevant for medicine as a diagnostic tool and for clinical and fundamental research as a noninvasive tool, MRI provides high resolution 3D static and dynamic images of organs and tissues. It probes the anatomy as well as the function of human inner body. Continuously under development, MRI is being improved by new methods and instruments to further explore remote organs like the lung and to extract new biomarkers.

Hyperpolarized noble gas MRI was initiated in 1994 to cope with the difficulties hydrogen MRI faces when applied to the lung. The averaged low density of most of lung tissue combined with the fast transverse relaxation of NMR signal in the lungs, caused by the local gradients that appear near the extremely large air-tissue interfaces, makes signal weak and difficult to measure with standard MRI. Hyperpolarized gas MRI can provide a much higher signal thanks to induced hyperpolarization and a relatively longer lifetime. Furthermore, imaging gas, which is contained in the airspaces, directly probes unique functional information about lung ventilation, that cannot be obtained by hydrogen MRI or other imaging techniques. Magnetic Resonance Elastography (MRE) was independently initiated, nearly at the same time, to measure the mechanical properties of tissues and organs [54], [55].

The first technique will be the subject of this chapter. The second one will be described farther in the following chapter.

## 2.1. Nuclear Magnetic Resonance

### 2.1.1. A spin in a magnetic field

Every subatomic particle is characterized by a spin angular momentum,  $\vec{S}$  with an associated magnetic moment,  $\vec{\mu}$ , along the same direction:

$$\vec{\mu} = \gamma \vec{S} \quad (2.1)$$

where  $\gamma$  is the gyromagnetic ratio, which depends on the particle [56]. For nuclei of atoms like hydrogen or helium-3, with a one-half spin,  $S = 1/2$ , the quantum spin number  $S_z$  can only take two values:  $\pm \hbar/2$ , with  $\hbar = h/2\pi$  and  $h \approx 6.626 \cdot 10^{-34}$  J·s, Planck's constant. These nuclei have two spin states, sometimes referred as "up" for  $S_z = \hbar/2$  and "down" for  $S_z = -\hbar/2$  with respect to the main quantum axis given by the magnetic field  $\vec{B} = B_0 \vec{z}$  (Fig. 2. 1). The associated energies are:

$$E_{\pm 1/2} = \pm \gamma \hbar B_0 / 2. \quad (2.2)$$

It means they are split apart by the energy  $\Delta E = \gamma \hbar B_0$ , or  $\Delta E = \gamma \omega_0$ , where:

$$\omega_0 = \gamma B_0 \quad (2.3)$$

is the Larmor's pulsation, which depends on the specific nucleus. The corresponding frequency,  $f_0 = \omega_0 / 2\pi$ , is within the radiofrequency (RF) range at the current clinical standard MRI magnetic field strength of 1.5 T and 3 T.

NMR may be performed in human tissue on several nuclei of atoms like hydrogen  $^1\text{H}$ , the most plentiful, carbon-13  $^{13}\text{C}$ , fluorine  $^{19}\text{F}$ , phosphorus  $^{31}\text{P}$ , or sodium  $^{23}\text{Na}$ . For our studies of the respiratory system, the stable isotopes helium-3  $^3\text{He}$  and xenon-129  $^{129}\text{Xe}$

are the most appropriate [8]<sup>2</sup>. In this work, the stable isotope <sup>3</sup>He was used. In the table below, <sup>3</sup>He gyromagnetic ratio and resonance frequency are compared with those of hydrogen.

Nucleus	$\gamma$ (rad·T <sup>-1</sup> ·s <sup>-1</sup> )	$ f_0 $ at 1.5T (MHz)
<sup>1</sup> H	$2.675 \cdot 10^8$	63.87
<sup>3</sup> He	$-2.038 \cdot 10^8$	48.65

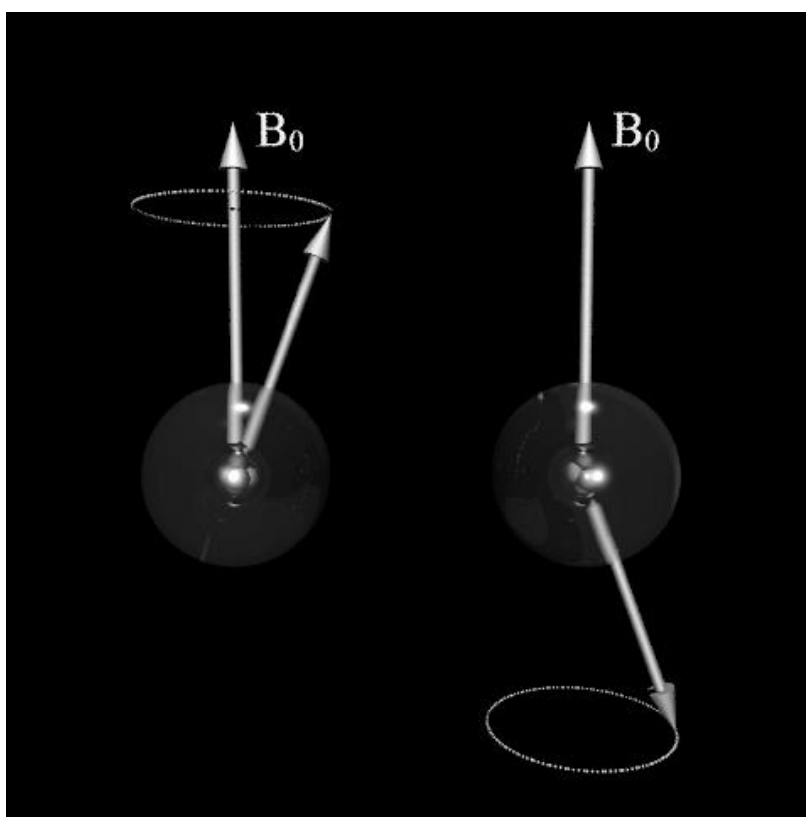


Fig. 2. 1: Classical precession (expectation value) of the magnetic moment; on the left the state parallel to the magnetic field while on the right the antiparallel one (Extracted from [57]).

---

<sup>2</sup>By extension, later in this manuscript, spin will indifferently addresses the nucleus of spin  $\vec{S}$ , or the atom with a nucleus of spin  $\vec{S}$ .

Nucleus	$\gamma$ (rad·T <sup>-1</sup> ·s <sup>-1</sup> )	$ f_0 $ at 1.5T (MHz)
<sup>1</sup> H	$2.675 \cdot 10^8$	63.87
<sup>3</sup> He	$-2.038 \cdot 10^8$	48.65

Table 2. 1: Gyromagnetic ratios and resonance frequencies for hydrogen and helium-3 used in this work [58]. A negative sign of the gyromagnetic ratio indicates precession in the opposite direction as compared to those with a positive value.

When a macroscopic sample, which contains a large number of atomic nuclei, experiences a magnetic field, the spins tend to get oriented along the direction of the directing field, because the system spontaneously tends to its configuration of least energy. Nevertheless, at room temperature, due to thermal motion, the nuclei are always redistributes into the two spin states. At thermal equilibrium, the spin populations in the two energy levels are ruled by the Boltzmann distribution [57]. The relative population difference defines the nuclear polarization  $P$ :

$$P = \frac{N_{+1/2} - N_{-1/2}}{N_{+1/2} + N_{-1/2}} \quad (2.4)$$

$$P \approx \frac{\gamma \hbar B_0}{2k_b T}, \quad (2.5)$$

where  $k_b$  is the Boltzmann constant and  $T$ , the temperature. At room temperature and standard 1.5 T, the hydrogen nuclear polarization is of the order of  $5 \cdot 10^{-6}$ . The above equation implies that the polarization could be enhanced either by decreasing the temperature of the sample or by increasing the magnetic field. For human *in vivo* experiments, the only obvious way has been followed, within the technological limits and the patient's safety, to reach field strengths of 3 T for clinical routine and, recently, 7 T for research developments. Nuclear polarization yields a macroscopic magnetization  $M_0$ , as a result of all elementary magnetic moments per unit volume, parallel and antiparallel with the magnetic field  $\vec{B}_0$ . The magnetization  $M_0$  is given by:

$$M_0 = \frac{\gamma \hbar}{2} n_s P, \quad (2.6)$$

where  $n_s$  is the density of nuclei in the sample.

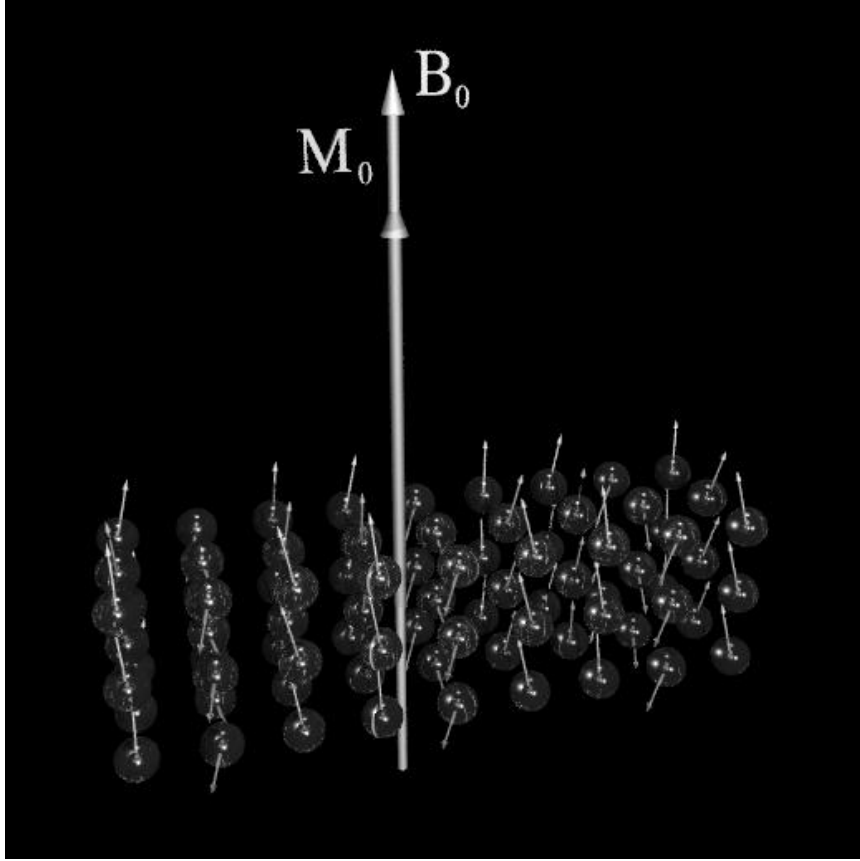


Fig. 2. 2: Representation of the longitudinal or net magnetization  $M_0$  of spins in a volume  $V$ , at equilibrium in a constant magnetic field  $B_0$  (Extracted from [57]). Standard NMR is performed on the basis of the magnetic field polarization at the thermal or Boltzmann equilibrium.

At thermal equilibrium, the magnetization  $\vec{M}(M_x, M_y, M_z)$  points along the main magnetic field direction:  $\vec{M} = M_0 \vec{Z}$  in the orthonormal system  $(0, \vec{X}, \vec{Y}, \vec{Z})$ . If the system is perturbed out of this thermal equilibrium state, it returns to equilibrium according to the Bloch equation [59], which describes the evolution of  $\vec{M}$  in an orthonormal system  $(0, \vec{X}, \vec{Y}, \vec{Z})$  as follows:

$$\frac{d\vec{M}}{dt} = \gamma \vec{M} \wedge \vec{B} + \frac{M_0 - M_z}{T_1} \vec{Z} - \frac{M_x \vec{X} + M_y \vec{Y}}{T_2}, \quad (2.7)$$

where  $T_1$  is the relaxation time of the longitudinal component of the magnetization (along  $\vec{Z}$ ) and  $T_2$  is the relaxation time of the transverse component of the magnetization (in the plane normal to  $\vec{Z}$ ).

To perturb or excite the system, an RF field, at the Larmor's frequency  $\omega_0$ ,  $\vec{B}_1 = B_1 \cos(\omega_0 t) \vec{X} - B_1 \sin(\omega_0 t) \vec{Y}$ , is applied orthogonally to the static field  $\vec{B}_0 = B_0 \vec{Z}$  during a time  $\tau$  such that  $\vec{M}$  is tipped by the nutation angle  $\alpha = \gamma B_1 \tau$  (Fig. 2. 2).

With the excitation, the magnetization precesses back to equilibrium around the magnetic field  $\vec{B}_0$  at the Larmor's frequency with characteristic relaxation times  $T_1$  and  $T_2$  (Fig. 2. 3). After a nutation of  $90^\circ$  at  $t = 0$ , the components of the magnetic moment are given by:

$$M_z = M_0 \left[ 1 - e^{\left(-\frac{t}{T_1}\right)} \right] \quad (2. 8)$$

$$M_t = M_0 \left[ e^{\left(-\frac{t}{T_2} + i\omega_0 t\right)} \right] \quad (2. 9)$$

with  $M_t = M_x + iM_y$  the complex expression of the magnetization in the transverse plan [8], [57].

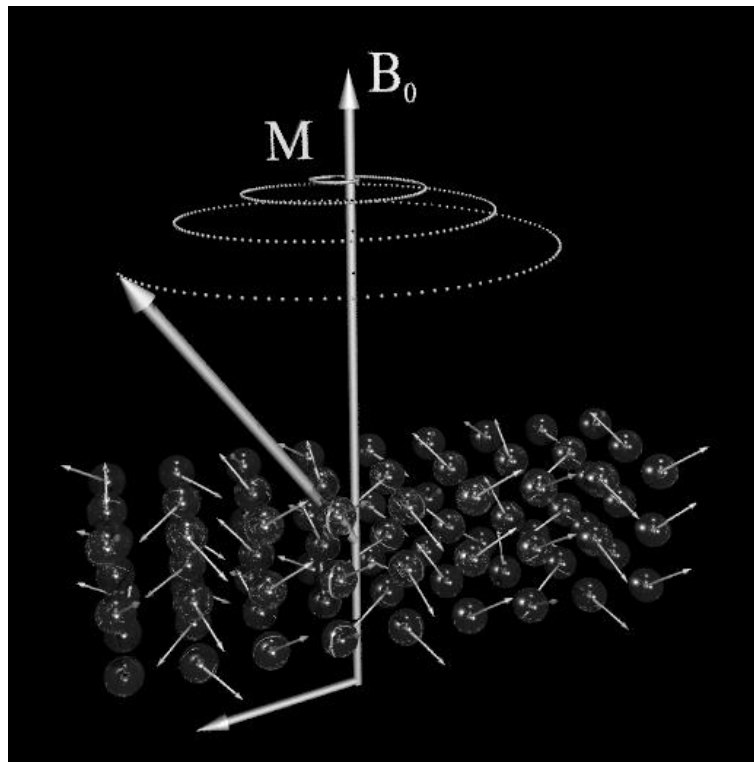


Fig. 2. 3: Tipping of the magnetization by the application of a transverse excitation RF  $\vec{B}_1$  field. (Extracted from [57]).

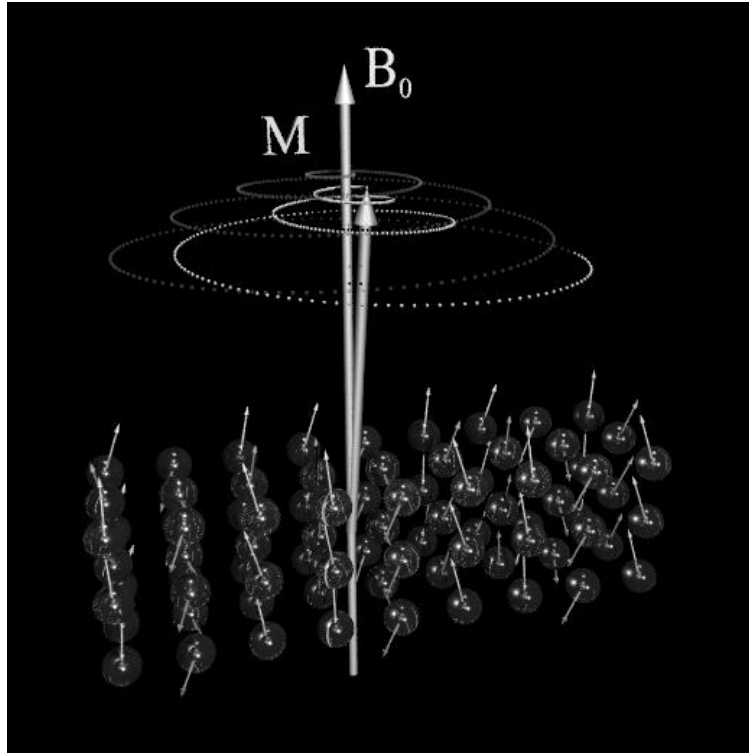


Fig. 2. 4 : Free precession of the magnetization back to equilibrium after RF excitation [57].

### 2.1.2. NMR signal acquisition

As shown in Fig. 2. 3, during relaxation, the magnetization vector precesses around the directing magnetic field till the transverse magnetization has completely relaxed and the longitudinal magnetization, recovered. During this process, the magnetic field of the magnetization vector, proportional to  $M_t$ , is detected by a resonant circuit, a coil, and a free induction decay (FID) may be monitored along the time (Fig. 2. 1).

In complex form it can be written as:

$$S(t) \propto \omega_0 M_0 \sin \alpha e^{\left(-\frac{t}{T_2} + i\omega_0 t\right)} \quad (2.10)$$

where  $\alpha$  is the flip angle and it is given by

$$\alpha = \gamma B_1 \tau \quad (2.11)$$

with  $\tau$  the duration of the excitation RF pulse.

An RF coil, tuned at the Larmor frequency, is an RLC circuit with a characteristic quality factor  $Q_c = \omega_0 L_c / R_c$ , where  $L_c$  and  $R_c$  are the inductance and the resistance of the system. Practically,  $Q_c$  is the ratio between the Larmor frequency and the bandwidth at -3 dB:  $\Delta\omega_0 = \omega_0 / Q_c$  [8].

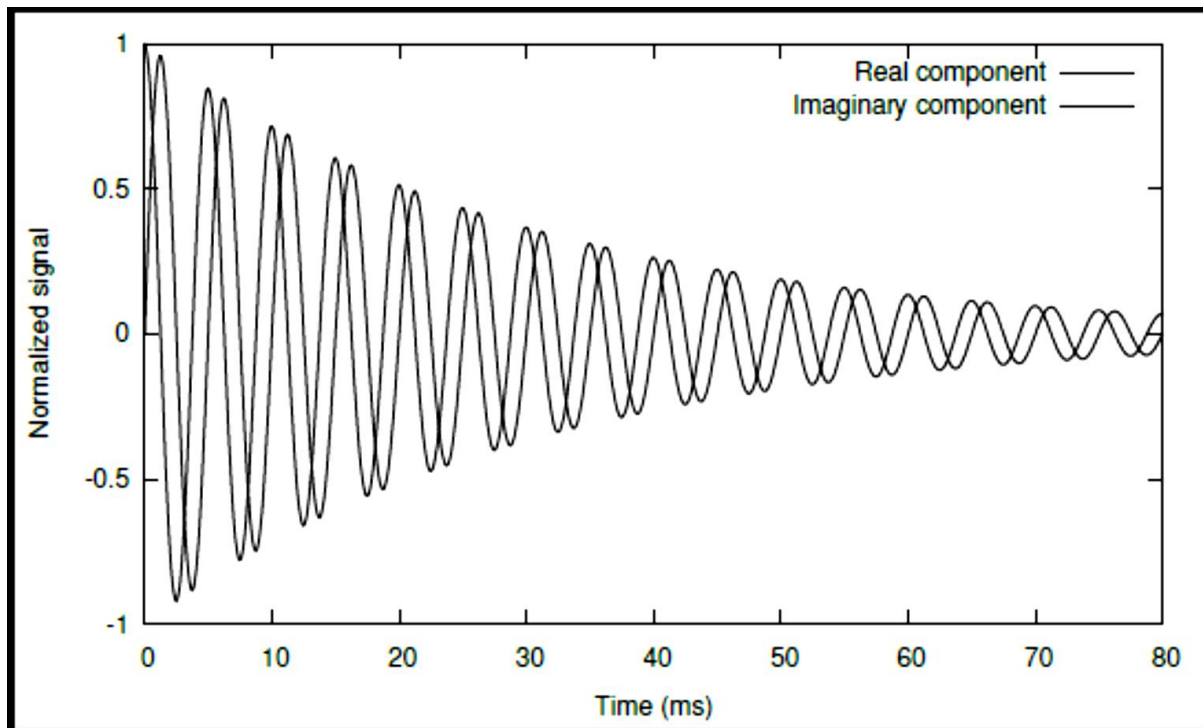


Fig. 2. 1 : Free induction decay (FID) detected by a set of two RF coils, orthogonal to the directing field  $\vec{B}_0$ , during the precession of the magnetic moment.

## 2.2. Magnetic Resonance Imaging

Once we know how the NMR signal comes out from the sample, we have to figure out from where it comes to make an image out of it. The raw MRI data is in what is called k-space or Fourier space, the Fourier transform of the image. Every features in an MR image have their origin in the raw data of k-space. Between the NMR signal and this k-space image, sequential spatial encoding process is applied by spatially varying the static magnetic field intensity with the help of constant magnetic field gradients along the different spatial dimensions. This process relates the resonance frequency of the spins, hence of the NRM signal, to the position of the spins themselves through the local magnetic field strength.

### 2.2.1. k-space and gradients

In MRI, the longitudinal component of the static magnetic field  $\vec{B}_0 = B_z \vec{Z}$  may be varied by implementing a gradient field  $\vec{G} = \overrightarrow{grad} B_z$  to localize the origin of the NMR signal. Under a spatial variation  $\vec{r}$ ,  $B_z$  changes the resonant frequency accordingly. At the position  $\vec{r}$  we have:

$$B_z = B_0 + \vec{G} \cdot \vec{r} \quad (2.12)$$

When the gradient field is applied during  $t$ ,  $\vec{k}$  is defined as:

$$\vec{k}(t) = \gamma \int_0^t \vec{G}(\tau) d\tau. \quad (2.13)$$

When relaxation effects are neglected and the sensitivity of the detection is considered homogenous, for an elementary magnetization  $m(\vec{r})$  distribution of an elementary volume  $d\nu$  at position  $\vec{r}$ ,  $m(\vec{r})$ , the measured signal is:

$$S(\vec{k}) \propto \sin(\alpha) \int_V m(\vec{r}) e^{i\vec{k} \cdot \vec{r}} d\nu \quad (2.14)$$

where  $\alpha$  is the flip angle. On the targeted volume  $V$ ,  $S(\vec{k})$  is the Fourier Transform ( $FT$ ) of the spatial distribution of the magnetic moment so that by an Inverse Fourier Transform ( $FT^{-1}$ ) and enough recorded information on  $S(\vec{k})$  at different positions throughout the  $k$ -space, it is possible to obtain  $m(\vec{r})$ . Three types of space-sensitizing gradients may be implemented in an MRI pulse sequence to encode the origin of the NMR signal onto the acquired signal: frequency, phase, and slice encoding gradients.

#### 2.2.1.1. Frequency encoding gradient

In frequency-encoding, the NMR signal is encoded by assigning a unique Larmor frequency to each spin isochromat (cluster of spins precessing at the same frequency) at a distinct spatial location along the gradient direction, which is applied during data readout. Thus, the time-domain NMR signals are emitted in a range of frequencies, which correspond to the different spatial locations. Each frequency corresponds to a spatial location along the gradient direction. The frequency-encoding gradient may have a positive or negative polarity.

#### 2.2.1.2. Phase encoding gradient

In phase encoding, a constant gradient pulse is applied while the magnetization is in the transverse plane before data readout. Hence, the magnetization phase, namely the signal

phase angle accumulated from the original tipping RF excitation, is linearly and stepwise varied along the spatial dimension of the applied gradient pulse. The amount of the accumulated phase is proportional to the gradient pulse time integral, as given by Eq. 2. 13. Phase-encoding is usually implemented to encode the spatial information along one or two directions orthogonal to the frequency-encoding direction.

#### 2.2.1.3. Slice selection gradient

In slice selection, every isochromats but the ones present in a slice may be set off-resonance by applying a constant gradient orthogonally to the chosen slice during a bandwidth limited RF excitation pulse. Then, only the isochromats in the slice are at resonance and will be excited by the RF pulse. A slice-selection gradient is also implemented in MR imaging for other selective RF pulses like refocusing, inversion, and spatial presaturation of magnetization [60], [61]. For the RF pulse excitation, a slice-rephasing gradient lobe follows the slice-selection gradient. This gradient is employed to translate the band of frequency into the targeted spatial location, corresponding to the selected slice. The slice thickness is determined by the gradient amplitude and the RF pulse bandwidth.

#### 2.2.1.4. Fourier space acquisition

Each of the three different spatial encoding mechanisms (frequency encoding, phase encoding, and slice selection) discussed in the previous sections, can only code spatial information in one dimension: any of them alone can provide at most a one-dimensional profile of the sample in a given direction. The creation of an image, which requires spatial encoding in two or three directions, is performed by sequentially combining frequency and phase encoding (and often slice selection).

A standard image acquisition method – a gradient echo pulse sequence – is shown in Fig. 2.

5

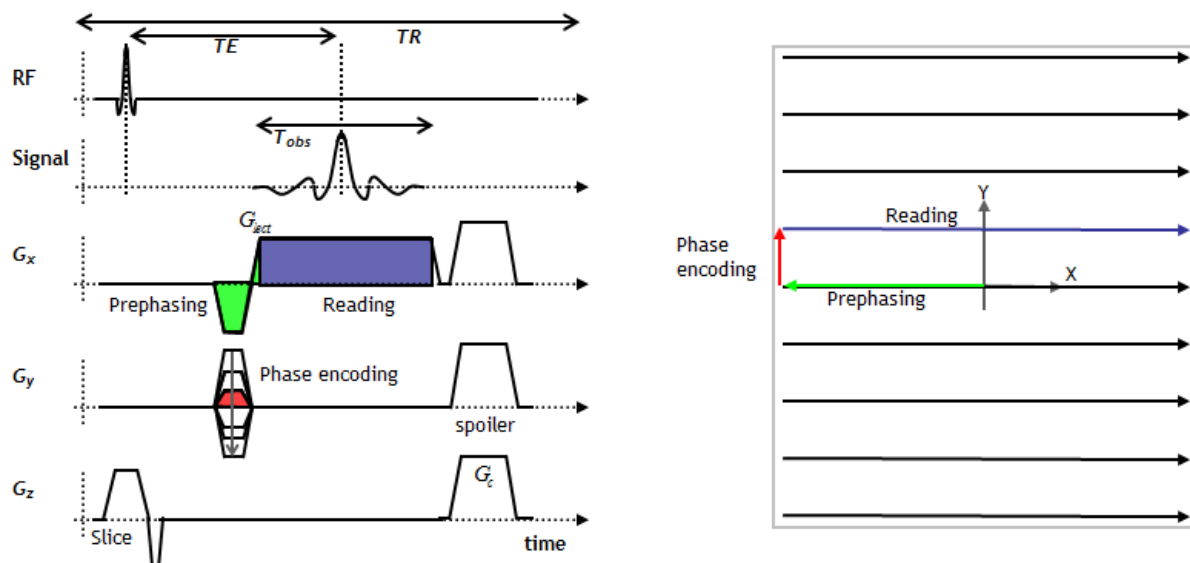


Fig. 2. 5 : Chronogram of a standard gradient echo pulse sequence (left) with corresponding trajectory in the Fourier plane (Extracted and adapted from [62]).

The acquisition of the image involves several iterations, in each of them once transverse magnetization has been created by RF excitation, the phase encoding gradient is applied before the frequency encoding gradient for data sampling. Each repetition of this process is performed with identical frequency encoding parameters, and different phase encoding gradient strength. The corresponding sets of acquired data points correspond to lines in one direction of k-space. This direction is called “read” or “readout” direction and is conventionally labelled as the  $k_x$  axis of the k-space. The direction orthogonal to the readout direction, called the phase encoding direction, is conventionally labelled as the  $k_y$  axis. Additional spatial encoding to include the third spatial coordinate, either by slice selection (2D and multi-slice, MS, imaging) or additional phase encoding (3D imaging) is performed in the third axis orthogonal to  $k_x$  and  $k_y$ , which is called the slice direction  $k_z$ . The process of repeatedly sampling with varying gradients, till all the data points needed to construct the image have been acquired, is usually referred in common MRI parlance as “k-space filling”. The correspondence of k-space coordinates (read, phase, and slice) with space coordinates ( $x$ ,  $y$ , and  $z$ ) depends on the chosen orientation of the field of view (coronal, axial, sagittal, oblique).

In the gradient echo sequence, the magnetization is dephased before being-rephased by the spatial encoding gradients along the readout direction. The maximum signal measured when rephasing occurs is called “echo”. It is the source of the name to the sequence. Other types of

sequences, in which additional dephasing-rephasing mechanisms are involved are called accordingly (such as spin echo, stimulated echo) but the gradient echo generally remains at the core of the acquisition sequence.

### 2.3. Hyperpolarized helium-3 Nuclear Magnetic Resonance

Hydrogen-based MRI prevails in most of the medical applications as water is the main constituent element of human tissue. The airways are an exception with close to 6% water vapor in a light gaseous medium. The lung parenchyma also presents a low density with a mean water density of  $0.2 \text{ g}\cdot\text{cm}^{-3}$  [63]. It is a spongy tissue with a very large interface, close to  $80 \text{ m}^2$ , between gas and tissue. In the MRI static magnetic field, it results in strong local magnetic field gradients that leads to short NMR relaxation times, hence short signal lifetime and weak NMR signal. Standard MRI does not provide bright images of the lung (Fig. 2. 6-a). Even though X-ray tomodensitometry furnishes very detailed anatomical images of the organ (Fig. 2. 6-b), it cannot provide any functional information.

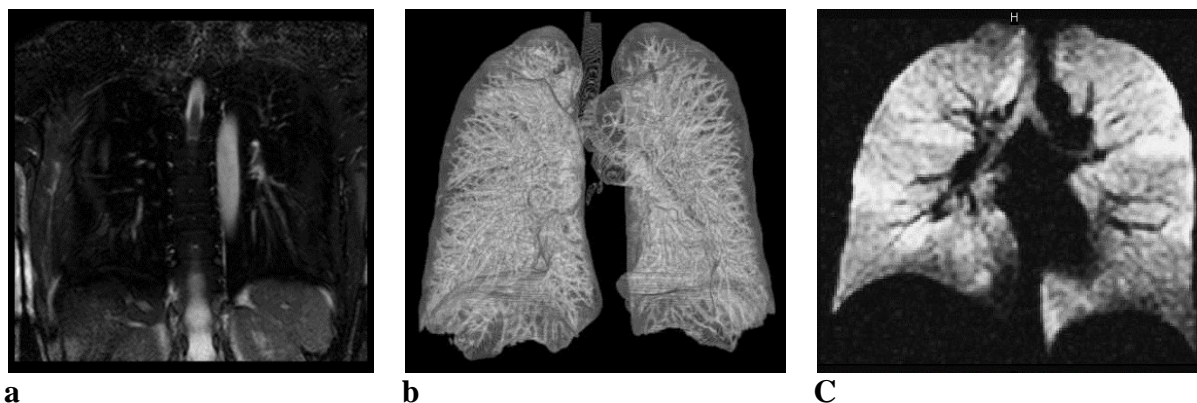


Fig. 2. 6: (a)  $^1\text{H}$  MRI of the human thorax with hydrogen nuclear polarization  $P \approx 5 \cdot 10^{-6}$ , (b) X-ray tomodensitometry of the lung, (Extracted from [57]), and (c) hyperpolarized helium-3 ventilation image with  $P \approx 1 \cdot 10^{-1}$ . The images a and c were acquired at IR4M.

To circumvent these limiting issues, artificially increasing the polarization of a tracer gas to be administered or inhaled in the airways came as a possible solution from atomic and nuclear physics. Initiated in 1994 [64], in the United-States [65], in Germany [66], and in France [67], hyperpolarized noble gas MRI involves polarizations of helium-3 or xenon-129 species greater by five orders of magnitude than thermal polarizations used in standard MRI. By this technique, it is possible to obtain lung ventilation 3D images [67], dynamic images of the respiratory function [68], or diffusion maps [69], [70], and to explore both lung anatomy and function.

### 2.3.1. Hyperpolarized helium-3

One of the isotopes of helium, rare on Earth, is helium-3 ( $^3\text{He}$ ). Helium-3 nucleus is composed by two protons and one neutron and has a spin  $\frac{1}{2}$ . Helium-3 is a light, non-radioactive isotope of helium. It is highly demanded for its use in nuclear fusion research. Main physical and chemical features of helium-3 are given in Table 2. 2. With five orders of magnitude gain in achievable polarization, three orders of magnitude loss in relative density, hyperpolarized helium-3 at atmospheric pressure may provide 2 orders of magnitude of signal gain with respect to standard MRI at thermal equilibrium. Moreover, the artificial magnetization is prepared by optical pumping techniques outside the MR imaging bore, hence, it is independent of the MRI magnetic field strength.

Two main routes have been followed to polarize helium-3. Both approaches make use of optical pumping techniques developed in atomic physics. The first one is based on spin exchange with optically-pumped alkali atoms [71]. The second one, we used here, is based on metastability exchange with optically-pumped metastable helium-3 [72].

Name	Helium-3 ( $^3\text{He}$ )
Atomic number	2
Molecular mass	$3.016 \text{ g}\cdot\text{mol}^{-1}$
Density at 21° (air=1)	0.1
Water solubility	Insoluble
Ebullition point	3.19 K
Self-diffusion coefficient	$2\cdot 10^{-4} \text{ m}^2\cdot\text{s}^{-1}$
Dynamic viscosity (at 293K)	$17 \text{ }\mu\text{Pa}\cdot\text{s}$

Table 2. 2 : Main physical and chemical features of helium-3

### 2.3.1.1. Metastability exchange hyperpolarization

This method relies on collisions between optically-pumped helium-3 atoms prepared in the metastable state  $2^3S_1$  and helium-3 atoms in the ground state  $1^1S_0$  [72], [73]. The four main steps of metastability exchange optical pumping are:

1. A continuous RF field establishes a plasma in a low pressure helium-3 gas such that atoms are greatly excited and some of them are prepared in the metastability state  $2^3S_1$  (Fig. 2. 7).
2. In the metastable state, the atoms are electronically oriented by optical pumping in a small directing magnetic field, *via* the infrared transition  $2^3S_1-2^3P$ , with an ytterbium-doped fiber laser at a wavelength of  $\lambda=1083$  nm. By hyperfine coupling, the electronic polarization is transferred to the nuclear spin (Fig. 2. 7 and Fig. 2. 9).
3. In the collision between an atom in the ground state  $1^1S_0$  and a nuclearly and electronically polarized atom in the metastable state  $2^3S_1$ , the electronic energy, the metastability, is exchanged [73]. In this way, atoms in the ground state are prepared with a definite nuclear polarization.
4. The polarized gas is dynamically compressed from the low pressure plasma up to atmospheric pressure or eventually completed with a buffer gas in a storage cell.

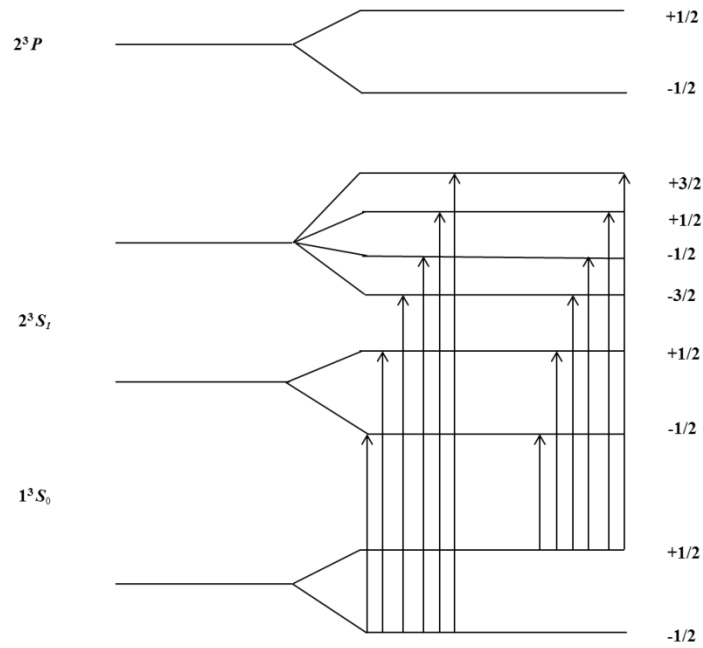


Fig. 2. 7: Energy levels of helium-3 for the ground state  $1^3S_0$ , the metastable state  $2^3S_1$ , and the excited state  $2^3P$ . Transitions from the ground state  $1^3S_0$  to the metastable state  $2^3S_1$  are shown. The degeneracy of the sublevels in the metastable state  $2^3S_1$  is lifted with a small directing magnetic field (adapted from [74] Chapter 1).

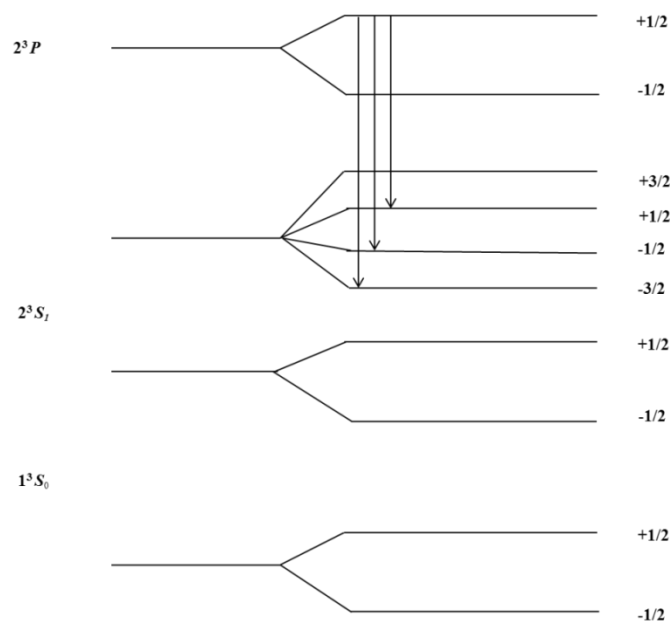


Fig. 2. 8: The atoms in the excited state  $2^3P$  fall back indifferently in the allowed sublevels of the metastable state  $2^3S_1$  by spontaneous emission (adapted from [74] Chapter 1).

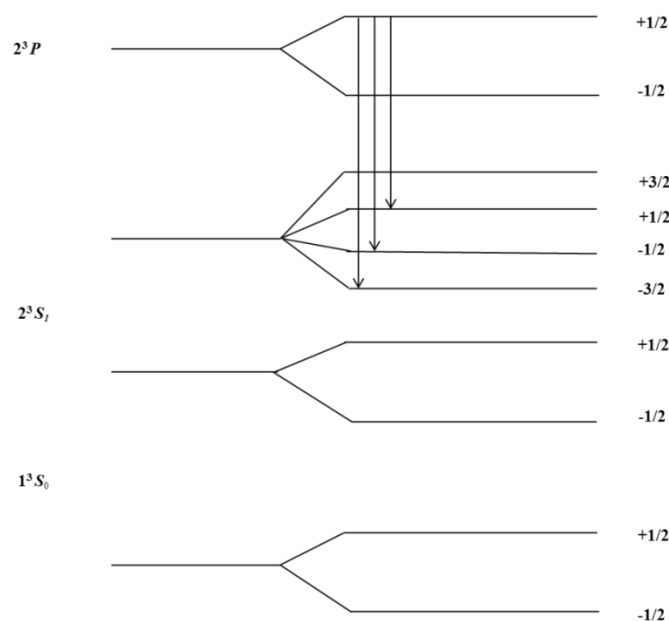


Fig. 2. 9: The atoms in the excited state  $2^3P$  fall back indifferently in the allowed sublevels of the metastable state  $2^3S_1$  by spontaneous emission (adapted from [74] Chapter 1).

The metastable state  $2^3S_1$  possesses two hyperfine levels  $F = 3/2$  and  $F = 1/2$  with a separation of 6.74 GHz in a magnetic field of a few milliTesla; it means six Zeeman energy sublevels ( $A_i$ , with  $i=1,\dots,6$ ). The  $2^3P$  level has five hyperfine levels (two  $F = 1/2$  levels, two  $F = 3/2$ , and one  $F = 5/2$ ); it means eighteen energy increasing sublevels by Zeeman effect ( $B_j$ , with  $j=1,\dots,18$ ). Helium-3 optical pumping is performed at room temperature in a static magnetic field of a few milliTesla. Optical pumping is optimal, both for the achieved static nuclear polarization and for the production of total magnetic moment, for the transition  $C_8$  ( $2^3S_1$ ,  $F = 1/2 \rightarrow 2^3P_0$ ,  $F = 1/2$ ), when the gas pressure is lower than 1 mbar, and for the transition  $C_9$  ( $2^3S_1$ ,  $F = 3/2 \rightarrow 2^3P_0$ ,  $F = 1/2$ ), when the gas pressure is higher [74], [75]. In the latter case, 80-90% of nuclear polarization can be expected by laser optical pumping with metastability exchange [75]–[80]. The magnetization production rate per unit time largely depends on the incident laser intensity and the RF discharge power to generate the plasma.

The metastability exchange hyperpolarization is very effective. In a few tens of seconds, polarizations up to 90% can be achieved. It does not require any additional compounds like alkali atoms necessary for spin exchange optical pumping [8], [74], [77], [81]. The production rate may also be very high but it relies on non-magnetic, non-depolarizing compression systems.

### 2.3.1.2. Centralized production and gas delivery

Hyperpolarized  $^3\text{He}$  used in the course of this work was both produced on site at 10% and imported from the Physics Department, University of Mainz, Mainz, Germany, where it was polarized at 69–71% by metastability exchange optical pumping. Once polarized, the gas was compressed up to 3 bar in glass cells contained in a special transport box [82] that creates an homogeneous magnetic field inside in order to conserve hyperpolarization and mechanically protects the cells from external shocks (Fig. 2. 10).



Fig. 2. 10: Transport *spin box*, containing three glass cells of hyperpolarized gas at 3 bar.

The spin box is built to preserve the cell from the mechanical external shocks and to create an homogeneous magnetic field inside in order to keep hyperpolarization for a few days ( $T_1 \approx 270$  h).

Finally, it is transported by airplane from Germany to our laboratory (CIERM, Le Kremlin Bicêtre, France). Actually, the gas can be shipped everywhere in the world. It has already been delivered throughout Europe but also in the United-States and Australia.

### 2.3.1.3. On-site production and administration

#### 2.3.1.3.1. Table top polarizer

Helium-3 hyperpolarization is also performed in our laboratory, with a compact system for on-site production originally developed by Pierre-Jean Nacher and Geneviève Tastevin (Laboratoire Kastler Brossel, Paris) [83]. To obtain a consistent dose of hyperpolarized helium-3, it is dynamically polarized and accumulated in a storage glass cell. In a low horizontal magnetic field, 1.5 mT, the gas is injected in a cylindrical Pyrex optical pumping cell, 50 cm long and 5 cm diameter (Fig. 2. 11), where an RF discharge ( $\sim 3$  MHz) maintains the plasma while a laser beam (2-5 W) (Keopsys, Lannion, France) optically pumps the

metastable atoms. A compact peristaltic compression system [84] is employed to extract the polarized gas from the optical pumping cell to a 500 cm<sup>3</sup> storage cell, made of pure quartz, with low magnetic impurities (Fig. 2. 12). The polarization in the storage cell is monitored by acquiring low angle FIDs with a dedicated NMR device. Polarization of 30-40% could be achieved with this system. However, the gas was routinely polarized at 10% over 30 min to produce a dose of 60 cm<sup>3</sup> of fully polarized helium-3 at atmospheric pressure.

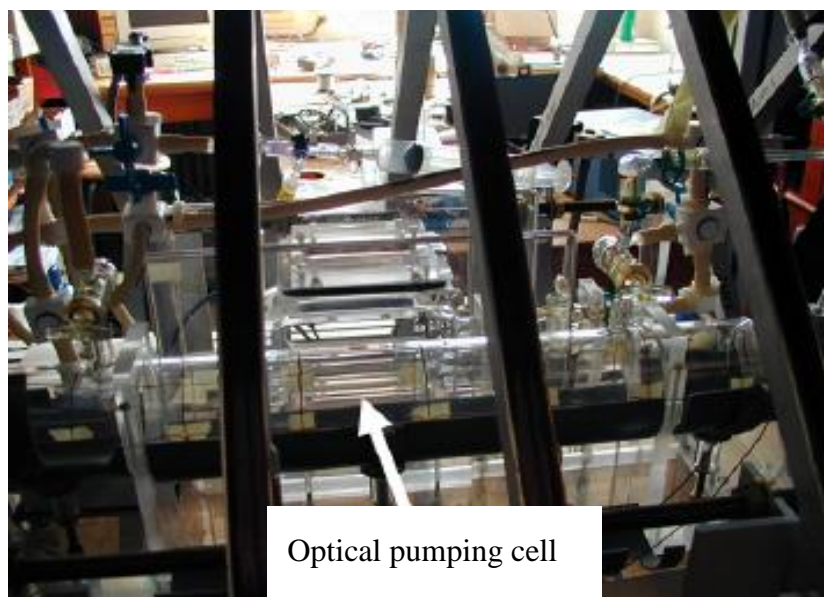


Fig. 2. 11: Table top polarizer at IR4M. The gas is injected in the optical pumping cell where a plasma is maintained by an RF discharge.

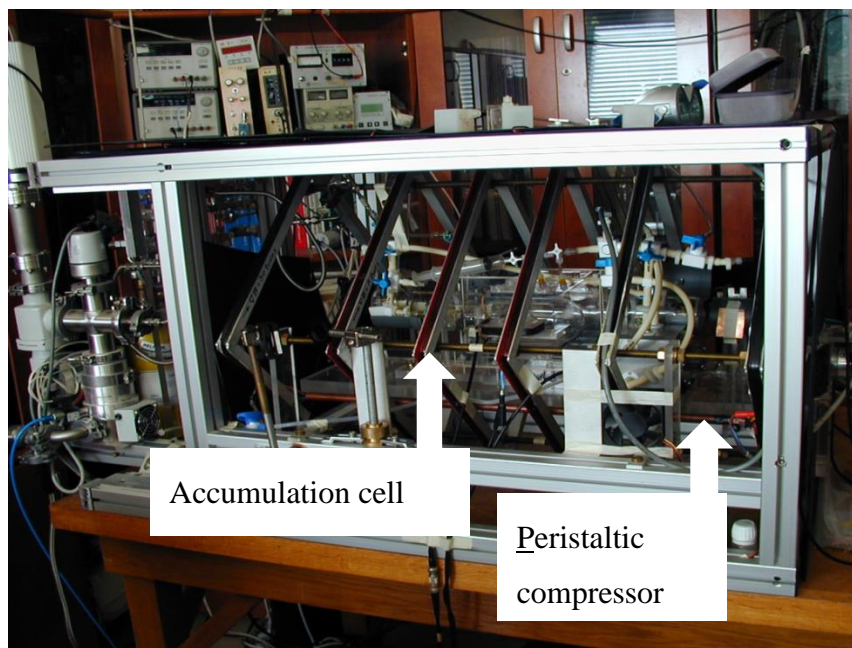


Fig. 2. 12 : Table top polarizer at IR4M. View of the accumulation cell (left) and the peristaltic compressor (right). The set of 6 coils around the polarization and accumulation cells creates a weak directing magnetic field of 1.5 mT.

#### 2.3.1.3.2. Human gas administration

One of the simplest way to ultimately transport hyperpolarized helium-3 from the table top polarizer or the high pressure cell to the subject and to administer doses to the subject is to use a Tedlar<sup>®</sup> bag (Fig. 2. 13) where  $T_1$  is around 20 min. Hyperpolarized gas can be transferred from the storage glass at 3 bars to atmospheric pressure. It can also be mixed with a buffer gas. This bag is manually closed by a valve and transported to the subject in the scanner. With the correct adaptors, the gas could be inhaled either directly from the bag by the volunteer, or after controlled and monitored administration [62].



Fig. 2. 13: Tedlar bag for transportation and administration of hyperpolarized helium-3. It is closed by a non-magnetic valve.

To prevent any human error and to ease the synchronization between the subject's inhalation and the start of the acquisition, an administrator for humans was adapted at IR4M from an original design developed by the University of Mainz [85]. It allowed to control and monitor the administration and ventilation parameters, such as gas pressure, volume, and flow rate.

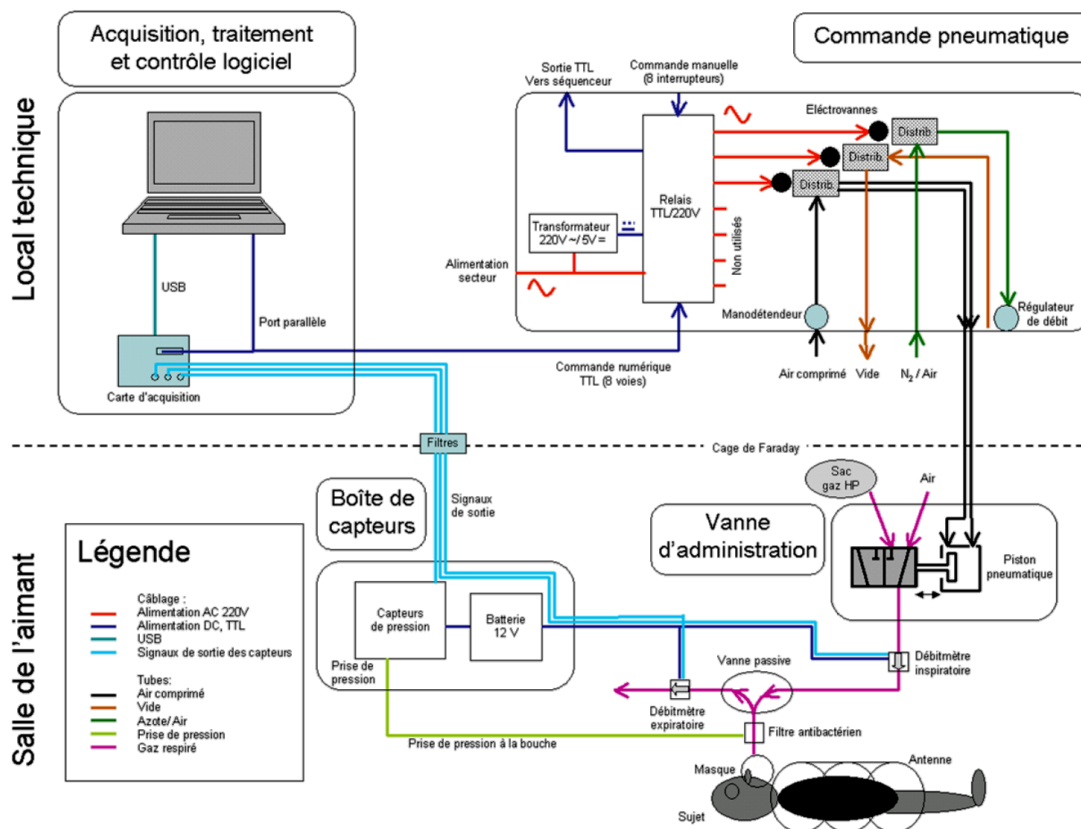


Fig. 2. 14: Schematic of gas administration for humans at IR4M. Three sensors are set to monitor mouth pressure, inspiratory and expiratory flow rates. The whole system is controlled by a computer (Extracted from [62]).

Its main function is to administer and control helium-3 gas volume and flow *in vivo* and *in vitro*. It includes basic spirometry control and synchronization with MRI. The system was MR-compatible, non-depolarizing, and safe for human use. A schematic of the human administrator is presented on Fig. 2. 14 [62].

### 2.3.1.3.3. Small animal gas administration

For small animals, the administration of the gas is generally associated to the animal ventilation, as the animal is anesthetized and the respiratory cycle is mechanically controlled. In our laboratory, a new MR-compatible ventilator was designed for animal ventilation, gas mixture, hyperpolarized gas, and aerosol administration: SAGAS (Small Animal Gas Administration System). The SAGAS software was programmed by José Manuel Perez Sanchez (Fig. 2. 15), while the SAGAS hardware was built by Mathieu Sarracanie *et al.* [8] (Fig. 2.17). It was successfully applied to aerosol deposition mapping with phase contrast

hyperpolarized  $^3\text{He}$  MRI [86]–[88] and for Apparent Diffusion Coefficient (ADC) and  $T_2^*$  mapping [89].

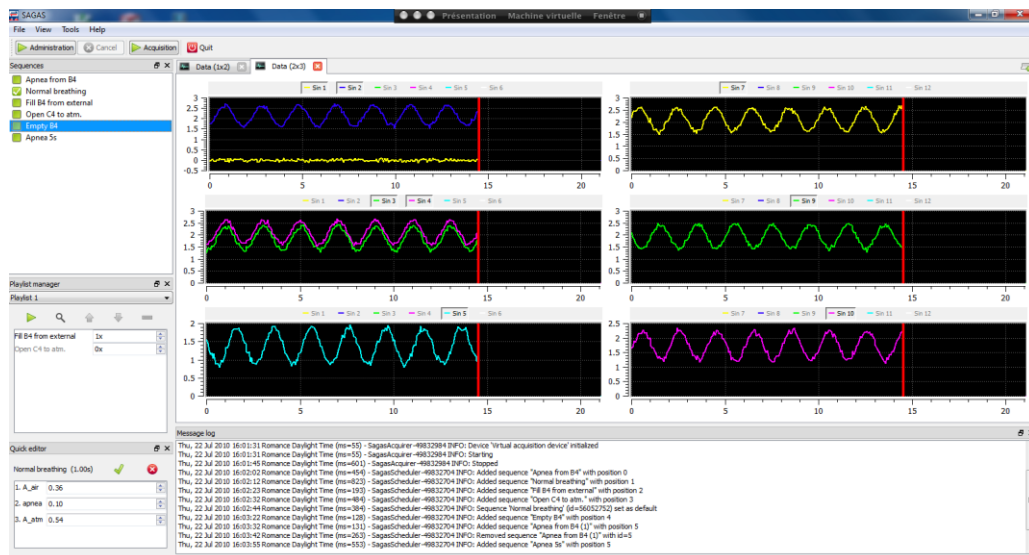


Fig. 2. 16: Screen shot of the software interface written in Python™ programming language. Here, the outcomes of six pressure sensors are displayed during normal mechanical breathing (extracted from [8]). The message log windows shows the implemented SAGAS sequences, which include system cleaning, normal breathing, helium-3 administration, apnea, etc... which can be uploaded from a library or generated *via* the interface.

After first experimental tests *post-mortem* (Fig. 2. 17) and *in vivo*, very reliable results were obtained with SAGAS for gas diffusion and aerosol deposition mapping, along the projects conducted by Kyle Hill, José Manuel Perez Sanchez, and Mathieu Sarracanie [8].

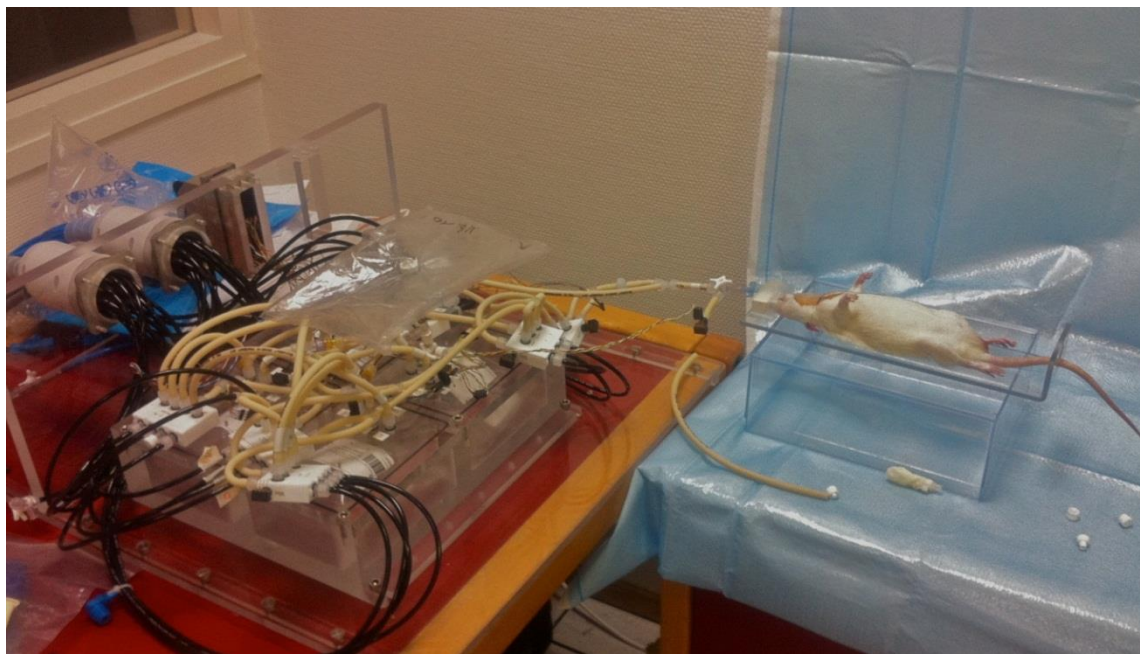


Fig. 2. 17: SAGAS system before the MRI scanner room. Initial ventilation tests were performed *post-mortem* (extracted from [90]).

### 2.3.2. Helium-3 imaging

#### 2.3.2.1. Total magnetic moment

The recorded signal of hyperpolarized gases highly depends on the applied RF excitation as it determines the amount of the total magnetic moment tipped in the transverse plane as well as the remaining total magnetic moment in the longitudinal axis for the following excitation. Besides, over the total acquisition time, the longitudinal relaxation, governed by  $T_1$ , drives the available total magnetic moment from the hyperpolarized state to the thermal equilibrium state, five orders of magnitude smaller, which is negligible and safely considered as zero in the following. Along equation (2.7), the corresponding Bloch equation for the total magnetic moment  $\vec{M}$  of hyperpolarized gas is thus given by:

$$\frac{d\vec{M}}{dt} = \gamma \vec{M} \wedge \vec{B} - \frac{M_z}{T_1} \vec{Z} - \frac{M_x \vec{X} - M_y \vec{Y}}{T_2}, \quad (2.15)$$

where the longitudinal magnetization is characterized by an exponential decay towards the thermal equilibrium with characteristic time  $T_1$ .

#### 2.3.2.2. RF depolarization

Hyperpolarization produces a very large but non-renewable total magnetic moment, which decays towards the negligible thermal equilibrium total magnetic moment. For MRI, any RF excitation, with the corresponding flip angle  $\alpha$ , induces  $M_0 \sin \alpha$  in the transverse plane and reduces the available total magnetic moment  $M_0$  along the longitudinal axis by a factor  $\cos \alpha$ . As a consequence, a single  $90^\circ$  pulse provides the highest NMR signal possible but it makes use of all the available magnetic moment; and the application of subsequent small angle RF excitations allows hyperpolarized gas MRI but it promotes the decay of the available magnetic moment, resulting in continuous attenuation of the subsequent NMR signals. It means that a compromise is to be made between the required number,  $N$ , of RF excitations for filling the k-space and the applied flip angle,  $\alpha$ . To optimize the overall image acquisition,  $\alpha$  is often chosen so the accumulated RF depolarization is limited to  $(\cos(\alpha))^{N-1} = \exp(-1)$  [91]. Variable flip angle approaches may also be followed to relieve the k-space filtering from the RF depolarization weighting.

### 2.3.2.3. Longitudinal relaxation

Intrinsically, the longitudinal relaxation is related to the interaction between the spins and the lattice. For hyperpolarized helium-3, this would lead to a very long intrinsic relaxation time. The effective longitudinal relaxation for hyperpolarized helium-3 is mainly governed by four other relaxation channels:

- 1) the gas interaction with some impurities embedded in the wall of the necessary container [85], [92];
- 2) the gas diffusion in the inhomogeneous magnetic field [92], negligible at atmospheric pressure in the center of the scanner but predominant at low pressure in the stray field or during the application of a large imaging gradient;
- 3) the interaction between helium-3 atoms [93], [94];
- 4) the interaction with gas impurities like oxygen, which is paramagnetic [94].

The characteristic time,  $T_1$ , of the resulting longitudinal relaxation, is then given by:

$$\frac{1}{T_1} = \frac{1}{T_1^{Wall}} + \frac{1}{T_1^{gr}} + \frac{1}{T_1^{dd}} + \frac{1}{T_1^{O_2}} \quad (2.16)$$

where  $T_1^{Wall}$  is the longitudinal relaxation time due to the wall impurities,  $T_1^{gr}$  is associated to gas diffusion in magnetic field inhomogeneities,  $T_1^{dd}$  stands for the interaction between the helium-3 atoms, and  $T_1^{O_2}$ , for the oxygen content.  $T_1^{Wall}$  can be between five minutes in plastic syringes and 20 minutes in Tedlar<sup>®</sup> bags to a few hundreds of hours in refined glass cells.  $T_1^{dd}$  is theoretically greater than 800 hours [92]. Finally,  $T_1^{O_2}$ , between fifteen to thirty seconds in human lungs, is the dominant relaxation time *in vivo* [85]. It sets the available time for performing hyperpolarized helium-3 lung MRI [8].

### 2.3.2.4. Transverse relaxation

Theoretically, for hyperpolarized gas in a perfectly homogenous magnetic field, the transverse relaxation time,  $T_2$ , is similar to the longitudinal relaxation time. Practically, in the MRI scanner, the homogeneity of the magnetic field is limited both by the global inhomogeneities of the MRI static magnetic field and by the local magnetic field gradients inferred in the lungs by the magnetic susceptibility differences between the gas in the airways and the surrounding tissues. At 1.5 T, the effective transverse relaxation time,  $T_2^*$ , ranges between 5 and 30 ms but its value highly depends on the magnetic field strength, the degree

of inflation of the subject's lungs, and the measurement technique, including the imaging effective voxel size and reconstruction method [74], [95]–[98].

#### 2.3.2.4.1. $T_2^*$ and voxel size

Apparent transverse relaxation with a time constant  $T_2^*$  shorter than  $T_2$  results from spin dephasing caused by magnetic field inhomogeneities. Spins contributing to the signal in a voxel precess at different angular pulsation due to the differences in magnetic field across the voxel. Since spins move according to molecular diffusion, the phase, that each of them accumulates, depend on the magnetic field pattern across the voxel and the trajectory they follow between the RF excitation and the signal acquisition. In turn, the magnetic field pattern in the voxel is determined by its spatial location and size. In hydrogen MRI, the distance covered by the spins during this time interval typically is about two orders of magnitude smaller than the voxel size and the effect of diffusion on  $T_2^*$  is negligible. In these conditions, the voxel location only determine the local voxel  $T_2^*$ . The picture is completely different in gas MRI, in which the distance covered by the spins between the RF excitation and the signal acquisition due to diffusion is often comparable to the voxel size and sometimes larger due to the higher molecular mobility of gases. In this case, the ratio of the diffusion length to the voxel size influences how much phase is differently accumulated by the spins contributing to the signal in a single voxel. The extreme case occurs when the spins sample most of the image voxels between excitation and acquisition such that they all effectively experience an average magnetic field over the field of view. The spatial magnetic field inhomogeneities across voxels are averaged by motional narrowing and the spins accumulate similar net phases over time. This can result in longer apparent transverse relaxation times. In gas MRI,  $T_2^*$  and diffusion are intermingled.

## **Chapter 3.           Magnetic resonance elastography of the lungs**

Exploring objects from outside by mechanical excitation and subsequent observation of their behavior is something we, humans, instinctively do. We are able to tap on something to check if it is hollow or solid, or to identify materials by the sound they produce under impact or mechanical stress. We often do this using one of our hands as a mechanical excitation device and our ears as receptors. We learn how to successfully execute this procedure at a rather early age.

The medical procedure known as auscultation is a refined implementation of the skill we have just described, in which hearing capabilities are extended by the use of a stethoscope and the professional is trained to properly judge what he or she hears back through the device; often the patient herself or himself creates the mechanical excitation by following some maneuvers (for example deep breathing) or excitation spontaneously happens through some physiological process taking place inside the body, such as heartbeat. Auscultation may be used as a raw tool to detect abnormalities in the lungs. This simple non-invasive test is only qualitative and it can provide only very rough regional information. It is unable to discern the disease by which the lungs are affected or quantify the mechanical properties of the organ.

Palpation is another primitive non-invasive test based on the mechanical properties of an organ or tissue. It is commonly applied on the liver for example. Basically, the organ or tissue is stimulated from outside at the surface of the body and its elastic “reaction” is studied. In this case, the reception device are the physician's hands and the tactile receptors we all have on the skin. Like auscultation, this test remains coarse and qualitative. It does not provide any definite diagnosis but rather some initial indications. Besides, it is not applicable to any remote organs as it is limited to organs accessible to palpation.

The recent technique known as elastography may be considered as a medical imaging based implementation of palpation and auscultation. Like its primitive counterparts, elastography is based on the response of viscoelastic tissues to a mechanical stress or a mechanical excitation. In elastography, the displacement field induced by the applied mechanical stress or by the propagation of the generated mechanical wave in the tissue is encoded in the acquired image or set of images. It is then possible to reconstruct a map of the mechanical properties of the tissue or organ through a suitable mathematical algorithm.

### 3.1. Basics of elastography

In elastography, it is fundamental to mechanically stress the targeted tissue or organ, by applying a time changing external pressure for example, and to study the resulting deformation. For a solid, the viscoelastic behavior is defined by two complex moduli: the compression and the shear moduli. Generally, soft tissue are considered quasi-incompressible, with a bulk compression modulus close to the one of water; but unlike water, they may be sheared.

The bulk compression modulus,  $K$ , expressed in kPa, is defined by the relationship between the pressure and volume variations,  $\Delta P$  and  $\Delta V$  respectively:

$$\Delta P = -K \frac{\Delta V}{V_0}, \quad (3. 1)$$

when compressive pressure is applied perpendicular to all surfaces of the observed system and where  $V_0$  is the initial volume (Fig. 3. 1).

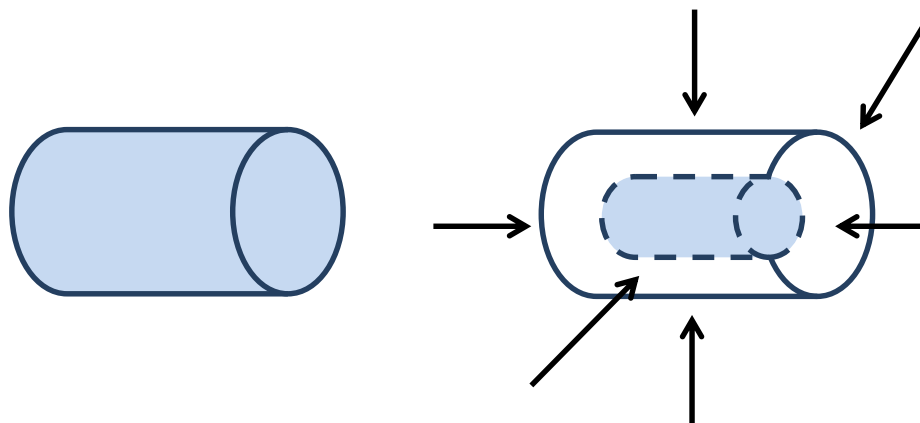


Fig. 3. 1: The bulk compression modulus,  $K$ , sets the proportionality between the pressure and the volume variations when a perpendicular pressure is applied everywhere on the boundary of the observed system.

In other words, it determines how much a system can be compressed under a defined uniform external pressure [6]. The bulk modulus, providing global information, cannot furnish any local properties concerning the tissue structure. For instance, in the lung, the bulk modulus information cannot be ascribed completely to the parenchyma mechanical properties nor to the bronchial tree [99].

Similarly, the shear modulus,  $\mu$ , also expressed in kPa, is defined by the linear relationship between inferred shear stress,  $\sigma$ , and applied strain,  $\gamma_s$  (Fig. 3. 2):

$$\mu = \frac{\sigma}{\gamma_s}, \quad (3. 2)$$

This modulus, also named Lamé's second parameter, is linked to the intracellular connection forces. Hence, the shear modulus may be a relevant indicator of tissue changes after infection, genetic defect, or environmental stress.

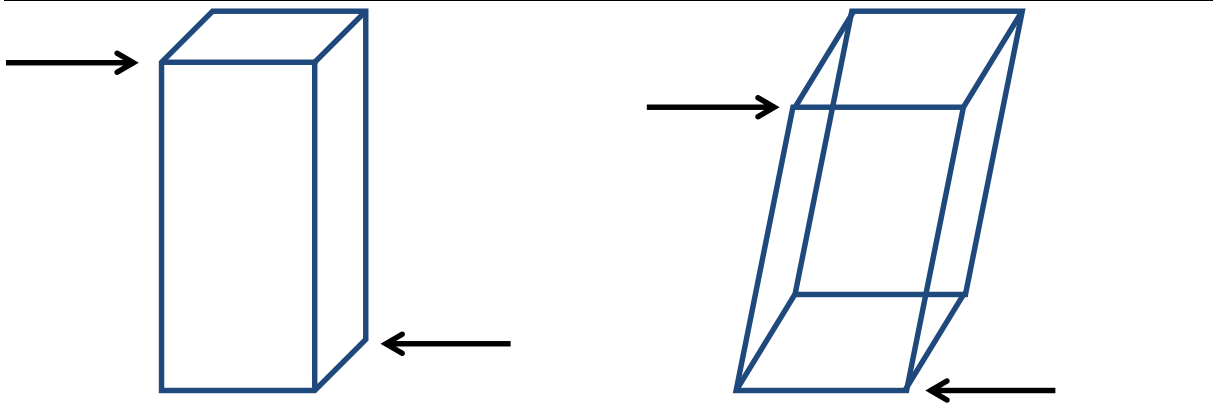


Fig. 3. 2: The shear modulus,  $\mu$ , sets the proportionality between the shear stress applied to a system and the resulting strain. Shear occurs when the system experiences a force parallel to one of its faces and an opposite force on the opposite face (left). Shear results in a deformation of the shape of the system (right).

For homogenous, isotropic materials, the shear modulus may be evaluated by measuring the Young's modulus  $E$ , which describes the response of the system to a linear stress (like pulling on the ends of a wire or putting a weight on top of a column). They are linked with the Poisson's ratio by:

$$\nu = - \epsilon_{\text{trans}} / \epsilon_{\text{longitudinal}} \quad (3. 3-a)$$

where  $\epsilon_{\text{trans}}$  is the transversal strain and  $\epsilon_{\text{longitudinal}}$  the longitudinal one. In isotropic and homogeneous materials, the equation becomes:

$$\mu = \frac{E}{2 \times (1 + \nu)} \quad (3. 4-b)$$

### Linear elasticity reminders [100]

The 3D **Hooke's law** of linear elasticity sets the relationship between the stress,  $\sigma$ , and strain,  $u$ , tensors:

$$\sigma = 2\mu u + \lambda_L \text{Tr}(u)I \quad (\text{III } 1)$$

where  $\mu$  is the shear modulus,  $\lambda_L$ , Lamé's first parameter,  $I$ , the identity matrix, and  $\text{Tr}$ , the trace function.

- **The Poisson's ratio,  $\nu$** , is the negative ratio of transverse to axial strains. It relates the shear and Young's moduli in isotropic systems:

$$\mu = E / (2 \times (1 + \nu)) \quad (\text{III } 2)$$

Consequently

$$\nu = \frac{E}{2\mu} - 1 \quad (\text{III } 3)$$

- **Lamé's first parameter,  $\lambda_L$** , is expressed in terms of the Young's modulus and the Poisson's ratio:

$$\lambda_L = \frac{E \times \nu}{(1 + \nu) \times (1 - 2\nu)} \quad (\text{III } 4)$$

#### 3.1.1. Static elastography

The most basic technique to probe the shear modulus of tissues or organs relies on imaging the latter before and during the application of a stress. It may be implemented with ultrasound first by acquiring a pre-compression image of the selected region of interest (ROI), second, by acquiring a post-compression image of the same ROI while applying a slight compression of the regional tissue using an ultrasound array.

The two sets of pre- and post-compression images are then compared by cross-correlation techniques to evaluate the differences of the arrival times of the echoes such that displacement maps can be obtained and strain maps, elastograms, derived [101]. This approach relies on the assumptions that, first, the applied stress is uniform, second, the tissue response is linear. The first assumption is difficult to fulfill in tissues and organs located deeply in the body. The experience puts in evidence that the second assumption usually fails at the boundaries of the targeted tissue or organ such that related artifacts are embedded in the elastograms [102].

An example of static elastography using ultrasound is set up in the Hitachi<sup>®</sup> ultrasound system (Hitachi, Tokyo, Japan) [103]. For the detection of mammalian tumor, this system was found more specific than the standard ultrasound technique [104], which, however, remains more sensitive. Some limitations of this technique are that the deformation maps are influenced by the pressure used to compress the tissues and that there is a lack of objective criteria for diagnosis.

### **3.1.2. Dynamic elastography**

Dynamic elastography techniques probe the propagation of shear waves. The following section describes different approaches of the technique.

### **3.1.3. Continuous elastography**

A first approach was already devised in 1987 by pulsed Doppler ultrasound to record the displacement gradients induced by sinusoidal external vibrations and to quantitatively measure the shear wave propagation in tissue<sup>3</sup> [105] but it suffered from excessive sensitivity to the phenomena of diffraction and reflection.

### **3.1.4. Transient elastography**

A second approach was based on a transient excitation [106] to alleviate these biases and extract more precise values of viscoelastic moduli in soft tissues. It was advantageously applied in one dimension (1D) for the development of the Fibroscan<sup>®</sup> (Echosens, Paris,

---

<sup>3</sup> The frequency shift obtained by Doppler effect is proportional to the velocity amplitudes.

---

France) [107]. Another application of this approach is the Aixplorer® system (SuperSonic Imagine, France). It is based on shear wave elastography technique (SWE) to overcome the disadvantages of other elastography techniques<sup>4</sup>. It efficiently provides stiffness estimation in patients' liver with chronic hepatitis [109].

By ultrasound, only 1D and 2D elastography is currently possible and 3D elastography is being developed. The 3D approach by MRI seems to be a promising alternative solution to get full information on the 3D displacement field inferred by the wave induced in remote tissues and to limit issues with imposed assumptions and reconstruction artifacts.

### **3.2. Magnetic Resonance elastography**

In the mid 1990's, the first Magnetic Resonance Elastography (MRE) images were obtained for continuous mechanical excitation [110]. Like ultrasonography, MRE is based on three fundamental pillars: motion generation, motion encoding, and motion processing. Even though the MR implementation is effectively more complex than for ultrasound, it has turned out to be the starting point for a broad range of applications [111]–[114] as MRE can provide unique 3D displacement field maps so to allow a complete, theoretically artifact-free reconstruction of the viscoelastic properties of the targeted tissue or organ.

Basically, propagating mechanical waves are generated at a given frequency in the targeted tissue or organ by a transducer that is driven by an electronically-generated waveform. MRI motion sensitizing gradients, synchronized with the mechanical excitation, are applied during the MR acquisition. Hence the phase of the MRI signal is shifted proportionally to the displacement field amplitude.

#### **3.2.1. Motion generation**

The first fundamental pillar on which MRE is based is mechanical excitation. MRE furnishes images (snapshots) of the displacement field in the medium at a precise moment of the

---

<sup>4</sup> SWE is based on supersonic shear wave imaging, an ultrasound technique employed for real-time visualization of elastic properties of soft tissues [108].

excitation cycle. Hence, the mechanical excitation must be continuous and the wave generated into the targeted tissue or organ must fulfil the following conditions:

- The induced shear wavelength must be smaller than the targeted tissue or organ. Hence the excitation frequency must be high enough.
- The induced shear wavelength must be larger than the implemented spatial resolution of the MRE acquisition in order to properly extract local information (see paragraph 3.2.11).
- The induced wave amplitude must be greater than the measurement error on the signal phase. It must be smaller than the critical elasticity threshold where the linearity assumption does not hold anymore. Typically, wave amplitude are expected between 1 and 100  $\mu\text{m}$ .

The related shear wavelength in the medium is given by:

$$\lambda = \frac{1}{f_v} \cdot \sqrt{\frac{\mu}{\rho}},$$

where  $\mu$  is the shear modulus and  $\rho = 1000 \text{ kg}\cdot\text{m}^{-3}$  is the volumetric mass. The choice of the excitation frequency of the induced wave is a trade of between better spatial resolutions (higher excitation frequencies but stronger attenuations and lower excitation amplitudes) and greater induced wave amplitudes (lower excitation frequencies but longer wavelengths and longer acquisition time). The excitation frequencies,  $f_v$ , are usually between 20 and 200 Hz for humans and between 100 Hz and 1000 Hz for small animals [123].

For optimal data processing and final extraction of the shear moduli, the excitation frequency must be accurately controlled and the waves must be generated into the tissues, within physiological limits, with minimal attenuation, diffraction, or reflection (see paragraph 3.2.3).

At the present time, the mechanical excitation devices commonly used are of three types: piezoelectric, electromechanical, and electropneumatic transducers.

#### 3.2.1.1. Piezoelectric transducers

In the piezoelectric stack driver system, the movement generation is based on the piezoelectric properties of the materials [115], [116]. With these devices, vibrations can be induced at frequencies between 100 Hz – displacement amplitudes of 24-40  $\mu\text{m}$  were recorded in phantoms [117], [118] – to 300 Hz [119]. The choice of the optimal frequency is

done considering the organ or tissue dimensions. A particular example is a dedicated rat liver vibration device by Piezo System, Inc (Cambridge, Ma, USA) (Fig. 3. 3) [120, pp. 119–139]. In this case, the excitation frequency was 300 Hz in order to adapt the wavelength to the dimensions of the rat liver.

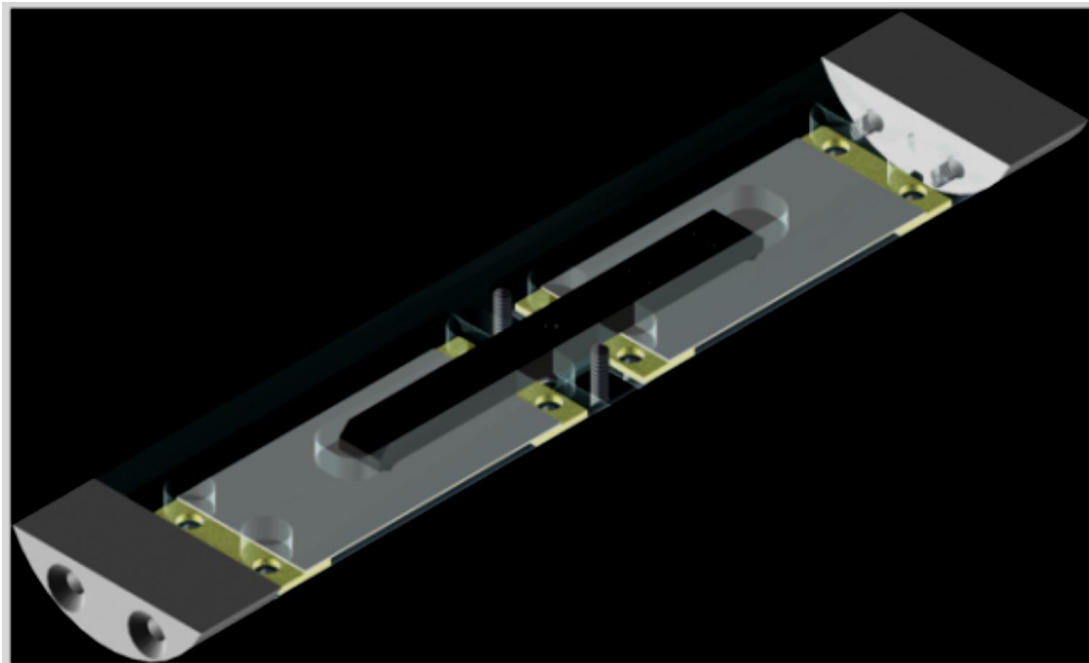


Fig. 3. 3: Two piezoelectric plates (grey) linked via a Bakelite bridge (brown). A piston (not shown) is taped in the middle of the bridge and coupled to the liver (Extracted from [120]).

#### 3.2.1.2. Electromechanical transducers

The electromechanical transducers are based on the Lorentz force and the static magnetic field of the MRI scanner [110], [121]. One of the electromechanical devices used during this project is a home built MR-compatible transducer implemented in an altuglas<sup>®</sup> bridge. In the transducer, a coil is energized by an alternating electrical current thanks to its coupling with a pulse-generator, triggered by the MR spectrometer. As the coil magnetic moment is coupled to the main field of the scanner, it provokes a net torque  $N$ . The pulse-generator generates a sinusoidal current that runs through the coil, which oscillates at the set frequency within the bore of the magnet (Fig. 3. 4). The achievable frequency range is determined by the coil moment of inertia. Here, in particular, the frequencies ranged between 50 and 400 Hz with an oscillation amplitude of the order of several 100  $\mu\text{m}$  [122].

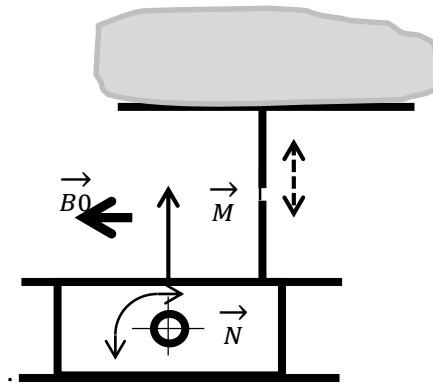


Fig. 3. 4: Scheme of the home-made electromechanical transducer where  $B_0$  magnetic field is perpendicular to the coil axis of the transducer. This coil produces a magnetic moment,  $M$ , which, coupled with  $B_0$ , generates the net-torque  $N$ . The movement generated by the transducer induces only the longitudinal (with respect to the transversal plane through the tissue) component of the oscillation in the tissue.

For human lung MRE acquisitions, the home-made transducer (Fig. 3. 5a-b) was fixed between the volunteer's chest and the helium-3 thorax coil to maximize vibration coupling to the thorax and to minimize additional low frequency movements.

For pig lung MRE acquisitions, an electromechanical transducer for human liver (Philips Healthcare, Hamburg, Germany) was adapted by the addition of a Teflon<sup>®</sup> extender at the extremity of the piston (Fig. 3. 5c) such that the transducer could be fixed outside the MR coil in order to avoid interferences between the coil and the device (Fig. 3. 5d).

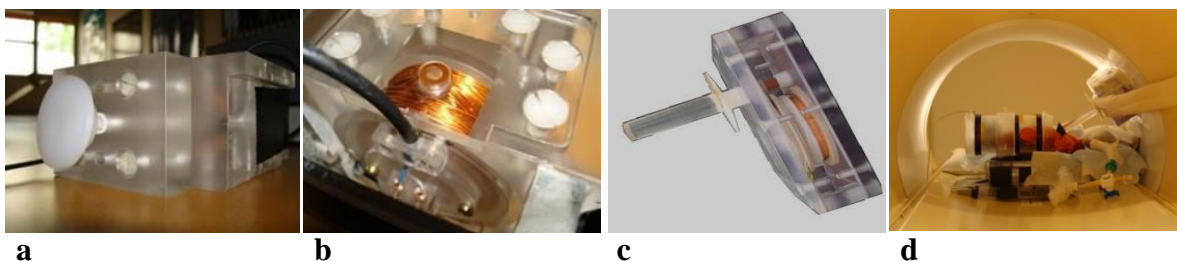


Fig. 3. 5: Electromechanical transducers used at IR4M for human lung MRE (a,b) and excised pig lung MRE (c,d). The end of the piston of the home-made device (a) allows a large contact on the subject's chest. The driving coil in the electromechanical transducer has to be set up orthogonally to the MRI static magnetic field (b). The piston of the Philips liver transducer was extended (c) to remotely vibrate excised pig lungs (d).

### 3.2.1.3. Electropneumatic transducers

For electropneumatic transducers, the vibration is driven, like for electromechanical devices, by the Lorentz force but it is remotely generated in a dedicated static magnetic field [124], [125]. Typically, an active driver, a loudspeaker, controlled by a function generator, is coupled, *via* a guiding hose, to a passive driver, a flexible membrane, to transmit the remotely emitted acoustic waves into the subject's body (Fig. 3. 6)

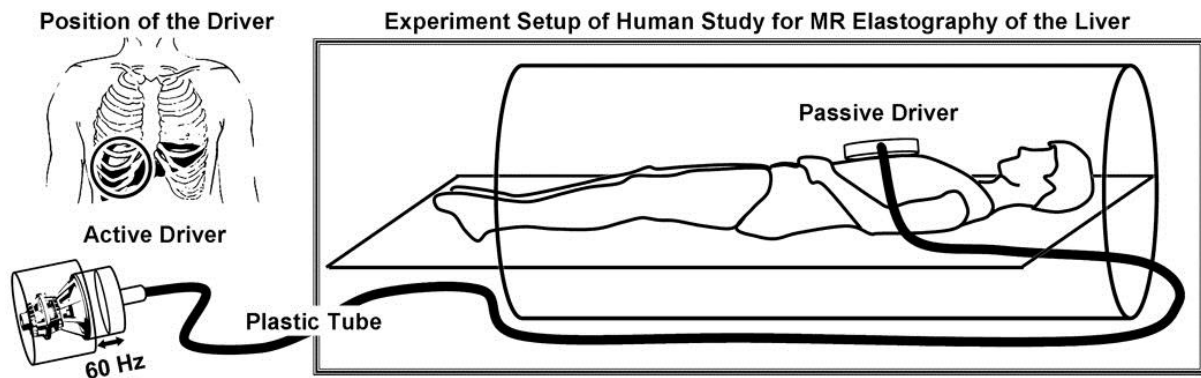


Fig. 3. 6: The loudspeaker (active driver), out of the scanner, generates acoustic pressure waves at 60 Hz, which are transmitted through a plastic tube to the pneumatic transducer (passive driver) onto the patient's abdomen (where the liver is located). (Extracted from [124])

#### 3.2.1.4. Electropneumatic transducers and guided pressure waves

To address far more remote and protected organs like the lungs, the emitted acoustic waves may be guided through the buccal cavity along the airways down to the distal alveolar spaces. This original approach, patented in 2010 [126] was shown to be very efficient not only for the lungs, when the subject breathes through the mouth [127], but also for the brain, when the subject breathes through the nose [128], [129]. It was advantageously developed and implemented in the course of this PhD work.

While the subject is lying in the MRI scanner (Fig. 3. 7-f), a function generator (Tektronix AFG 3021B), (Fig. 3. 7-b), triggered by the MRI scanner (Fig. 3. 7-a), generates a burst of sinusoidal forms that are amplified by an audio amplifier before driving a loudspeaker, which generates a pressure wave, sent through a waveguide (Fig. 3. 7-d) to the subject's mouth. The waveguide is a rigid tube connected to the loudspeaker cabinet (Fig. 3. 7-c), with adapting hoses at both ends. The length and diameter of the waveguide can be selected according to the desired frequency of the pressure wave such that the attenuation remains minimal along the way to the buccal cavity. Finally, the amplitude of the pressure wave is set at the function generator to compensate for losses between the loudspeaker and the subject's mouth. At the extremity of the waveguide, a flexible silicone hose (Fig. 3. 7-e) is connected to a breathing filter and a mouth piece to match the subject's buccal cavity inlet. A fiber pressure sensor is connected onto the breathing filter to monitor the pressure wave amplitude at the subject's mouth. The frequency range of the acoustic wave varies between 20 Hz and 500 Hz.

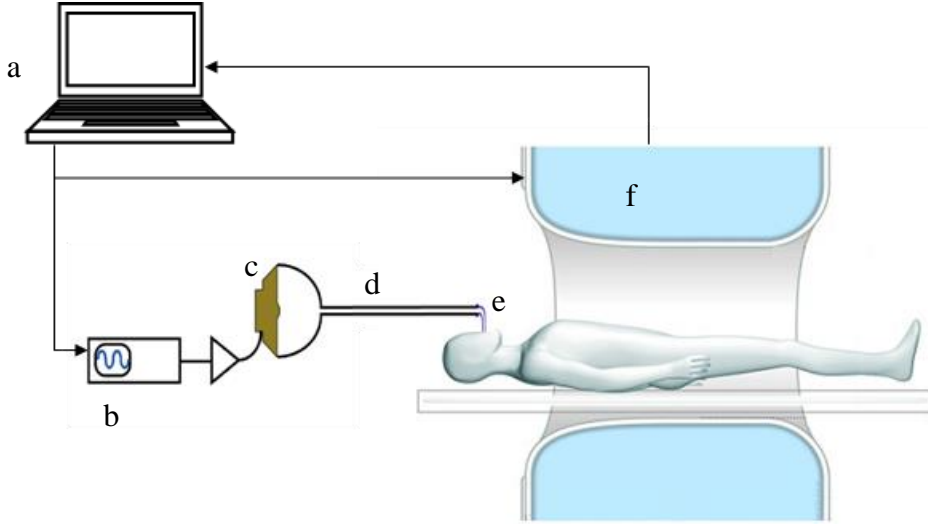


Fig. 3. 7: Setup for lung MRE with guided pressure waves. a: MRI console; b: function generator; c: loudspeaker; d: waveguide; e: flexible silicone hose; f: MRI system.

### 3.2.2. Motion encoding

Once compression and shear waves propagate through the targeted tissue or organ, the resulting displacement field may be mapped by a MR motion encoding phase-contrast technique [130]. In MRE, motion sensitizing gradients are synchronized with the mechanical wave such that the MR signal phase accumulates with the tissue oscillatory motion. These motion sensitizing gradients are sequentially implemented along the three spatial directions ( $i = \{M,P,S\}$  for Measurement, Phase, and Slice directions) at different time offsets with respect to the mechanical excitation to fully map the 3D mechanical wave over a time oscillation [131]. The resulting MR phase shift  $\Phi(T)$  over one period  $T$  of the mechanical wave is given by:

$$\Phi(T) = \gamma \int_0^T \vec{G}_i(t) \cdot \vec{s}(t) dt, \quad (3. 5)$$

where  $\gamma$  is the gyromagnetic ratio of the detected nucleus,  $\vec{G}_i(t)$  is the motion sensitizing magnetic field gradient applied along  $i$ , and  $\vec{s}(t)$ , the position of the corresponding atoms. When the atoms are submitted to a mechanical wave,  $\vec{s}(t)$  can be written as:

$$\vec{s}(t) = \vec{s}_0 + \vec{A}_0 \cos(\vec{k} \cdot \vec{s} - \omega_m t + \alpha_e) \quad (3. 6)$$

where  $\vec{s}_0$  is the mean position of the atoms,  $\vec{A}_0$  is the displacement amplitude,  $\vec{k}$  is the wave vector,  $\omega_m$  is the mechanical pulsation,  $T = \frac{2\pi}{\omega_m}$ , and  $\alpha_e$  is the initial phase offset. Considering the following sinusoidal gradient function:

$$\vec{G}_i(t) = \begin{cases} \vec{G}_i \cos(\omega_m t), & t \in [0, NT] \\ 0 & \text{otherwise} \end{cases} \quad (3. 7)$$

with  $N$  the number of encoding gradient cycles, then the final encoded phase shift is

$$\Phi(\vec{s}, \alpha_e) = \frac{2\gamma NT(\vec{G}_i \cdot \vec{A}_0)}{\pi} \cos(\vec{k} \cdot \vec{s} + \alpha_e) \quad (3. 8)$$

$\Phi(\vec{s}, \alpha_e)$  is proportional, first, to the scalar product of the displacement amplitude vector  $\vec{A}_0$  and the gradient vector  $\vec{G}_i$ , second, to the mechanical period and the number of gradient cycles,  $N$ . It finally depends on the initial offset  $\alpha_e$ . Such a motion measurement encoded onto the signal phase can be made sensitive to very small-amplitude oscillatory motion, on the micrometer scale, by accumulating phase shifts over  $N$  cycles of mechanical excitation and motion sensitizing gradient [131]. Standard 3D phase unwrapping techniques yield absolute displacement field maps over the mechanical time period from which the displacement amplitude vectors  $\vec{A}_0$  can be extracted after temporal sinusoidal fits [4], [5].

MRE may be implemented in different MR imaging sequences, each with its own advantages and limitations. Depending on the application, MRE pulse sequences were developed on the basis of spin-echo (SE), gradient recalled echo (GRE), balanced steady-state free precession, and echo planar imaging techniques [132]–[135].

In the framework of this original doctoral work, to match specific requirements of the two atomic species, MRE experiments were carried out with basic gradient echo pulse sequences for hyperpolarized helium-3 MR acquisitions and basic spin-echo pulse sequences for hydrogen MR acquisitions. The use of a gradient echo pulse sequence in hyperpolarized helium-3 experiments is dictated both by the gas fast diffusion, which makes spin refocusing detrimental, and by the overall lifetime of the hyperpolarization, which calls for short acquisition times (hyperpolarized helium-3  $T_1$  in the lungs is of the order several seconds – see Chapter 2). Besides, to limit artifacts from breathing motion *in vivo*, apneas are commonly used, which enforces the need for the faster imaging acquisition mode as provided by the simple gradient echo approach.

### 3.2.2.1. Gradient Echo or Fast Field Echo sequence

Fig. 3. 8 shows the diagram of a typical gradient recalled echo (GRE) or fast field echo (FFE) sequence implemented for hyperpolarized helium-3 acquisitions. In this diagram, a GRE sequence is modified to include a motion encoding gradient (MEG) for sensitizing the

sequence to the harmonic tissue motion and to generate synchronous pulses for triggering the mechanical motion. The sensitivity to the mechanical motion is very high: Motion amplitudes of the order of a few hundreds of nanometers can be probed by MR Elastography. The period and the number of MEG pulse are adjustable to the period of the mechanical motion and to the required phase accumulation. MEGs are sequentially applied along the three axes of the field of view, labeled here {M,P,S}. The sequence repetition time, TR, is chosen to ensure the continuous synchronicity between MEGs and the mechanical wave. The MR sequence is successively delayed by several time offsets (four or eight snapshots over the mechanical period  $T$ ) to record the temporal evolution of the displacement field. This series is implemented as dynamic scans.

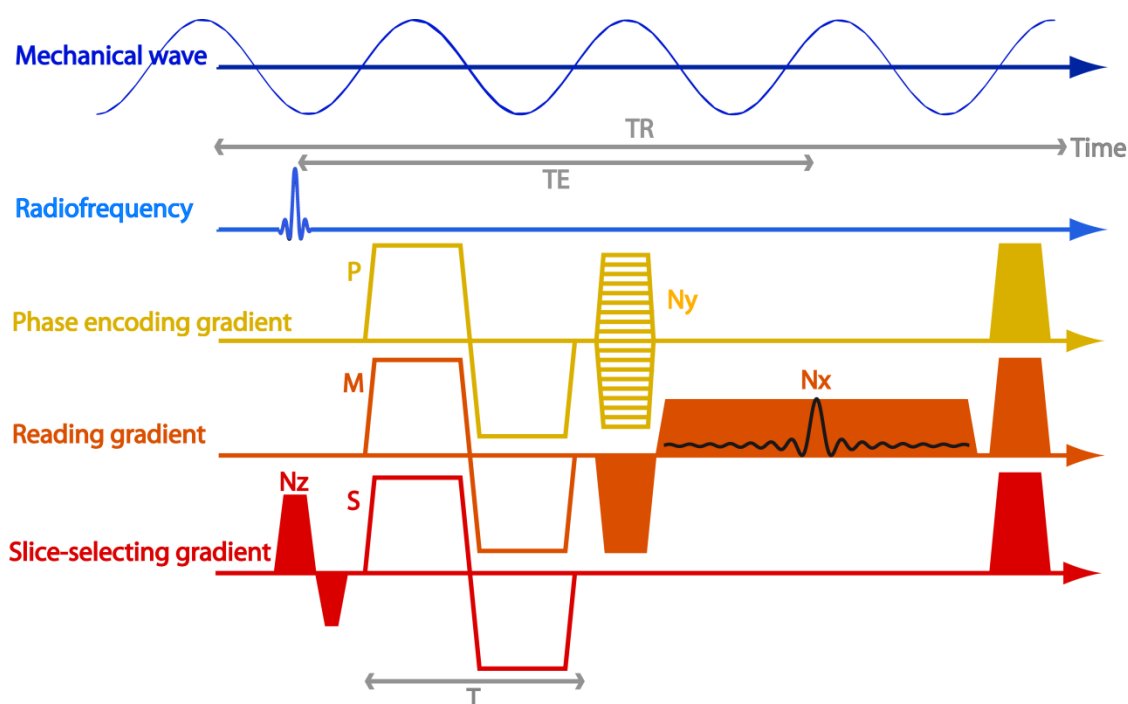


Fig. 3. 8: MRE sequence based on gradient recalled echo (GRE) or fast field echo (FFE) pulse sequence with motion encoding gradients (MEGs). MEGs are sequentially placed after the RF excitation and before the phase encoding and measurement of the MR signal along the three axes {M,P,S} during a single mechanical oscillation so  $N = 1$ . The repetition time, TR, is a multiple of the mechanical wave period. The echo time, TE, is taken as short as possible to minimize  $T_2^*$  weighting.

### 3.2.2.2. Spin Echo or Refocused Field Echo sequence

Fig. 3. 9 shows the diagram of the spin echo (SE) or refocused field echo (RFE) pulse sequence implemented for hydrogen MRE. MEGs are sequentially applied along the three axes of the field of view {M,P,S}. They are synchronized before and after the refocusing RF  $\pi$ -pulse with the mechanical wave. The repetition and echo times, TR and TE, are chosen to

ensure the continuous synchronicity between MEGs and the mechanical wave. Like for the FFE based sequence, the RFE sequence is successively delayed by several time offsets (four or eight snapshots over the mechanical period  $T$ ) to record the temporal evolution of the displacement field. This series is implemented as dynamic scans.

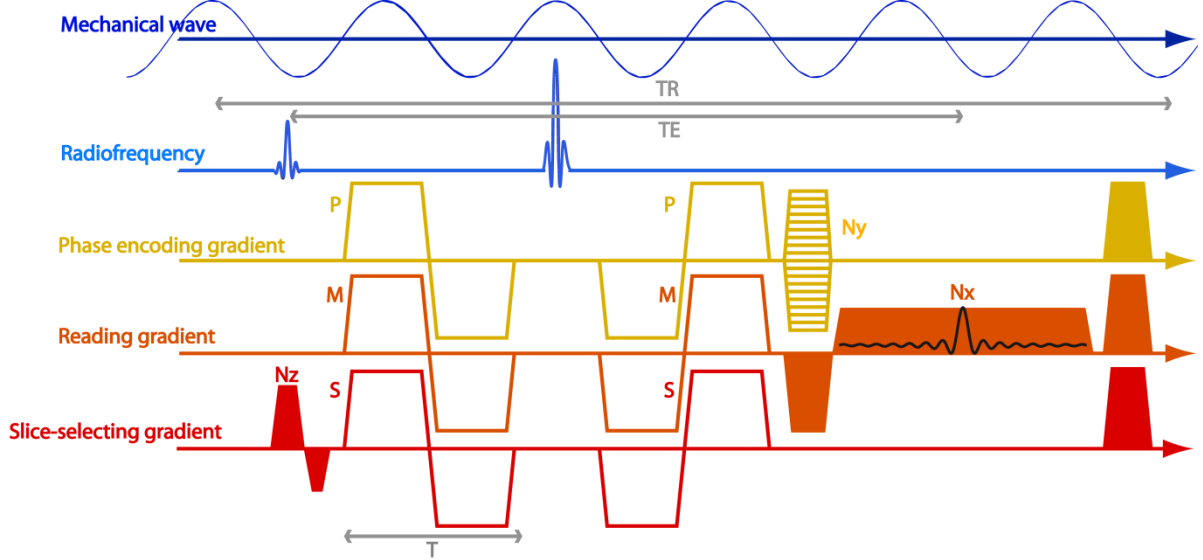


Fig. 3. 9: MRE sequence based on a spin echo (SE) or refocused field echo (RFE) pulse sequence with sequential motion encoding gradients (MEG) along the three axes {M,P,S}. MEGs are placed before and after the refocusing radiofrequency  $\pi$ -pulse over a single mechanical oscillation so  $N = 2$ . TR is a multiple number of the mechanical wave period, and the refocused  $\pi$ -pulse is at TE/2 time from the initial RF excitation pulse.

### 3.2.3. Image processing

#### 3.2.3.1. Equation of motion

If the living tissues were purely elastic and mechanically isotropic, from the generalized Hooke's law given above in eq.  $\sigma = 2\mu \mathbf{u} + \lambda_L \text{Tr}(\mathbf{u})\mathbf{I}$  (III 1, the relationship between the components of the stress,  $\sigma$ , and strain,  $\mathbf{u}$ , tensors would be as follows:

$$\sigma_{ik} = 2\mu u_{ik} + \lambda \delta_{mn} u_{mn}. \quad (3. 9)$$

Under the simplifying assumptions of an infinite linear and isotropic medium, the wave equation may be written as:

$$\rho \partial_t^2 \vec{u} = \mu \nabla^2 \vec{u} + (\lambda + \mu) \nabla (\nabla \cdot \vec{u}), \quad (3. 10)$$

where the two Lamé's parameters  $\lambda$  and  $\mu$  are scalars.

Biological tissues are generally viscoelastic and anisotropic such that the wave equation must be extended to [106]:

$$\rho \partial_t^2 u_i = \lambda_{iklm} \frac{\partial^2 u_m}{\partial x_k \partial x_l} + \eta_{iklm} \frac{\partial^3 u_m}{\partial_t \partial x_k \partial x_l}, \quad (3. 11)$$

where Einstein summation convention of summing on repeated indices holds for the elasticity  $\lambda$  and viscosity  $\eta$  tensors, the displacement field  $u$ , and the spatial derivation  $\partial x$  [120].

However, at spatial resolutions greater than the millimeter scale achieved here with MRE, there is no preferred mechanical directions in the lung such that isotropy could be assumed. Besides, local homogeneity was assumed thus the wave equation could finally be simplified to the following partial differential equation [136]:

$$\rho \partial_t^2 \vec{u} = \mu \nabla^2 \vec{u} + (\lambda + \mu) \nabla (\nabla \cdot \vec{u}) + \zeta \partial_t \nabla^2 \vec{u} + (\xi + \zeta) \partial_t \nabla (\nabla \cdot \vec{u}), \quad (3. 12)$$

where,  $\rho$  is the tissue density,  $\mu$  is the shear elasticity modulus,  $\lambda$  is the first Lamé's parameter,  $\zeta$  and  $\xi$  are the shear and compression viscosity moduli.

### 3.2.3.2. Inverse problem

In MR elastography processing, we must perform an algebraic inversion of the partial  $\partial_t^2 u = \mu \nabla^2 u + \lambda + \mu \nabla \nabla u + \zeta \partial_t \nabla^2 u + \xi + \zeta \partial_t \nabla \nabla u$ , (3. 12) describing the propagation of the mechanical wave to finally extract the viscoelastic parameters. First of all, in a soft medium, the Helmholtz decomposition can be applied onto the displacement field, so the displacement field can be split into a curl free component (corresponding to the compression wave) and a divergence free component (corresponding to the shear wave). The displacement field can thus be decomposed as:

$$\vec{u} = \vec{u}_p + \vec{u}_s = \vec{\nabla} \Phi + \vec{\nabla} \times \vec{\Psi}, \quad (3. 13)$$

$\partial_t^2 u = \mu \nabla^2 u + \lambda + \mu \nabla \nabla u + \zeta \partial_t \nabla^2 u + \xi + \zeta \partial_t \nabla \nabla u$ , (3. 12) is split into two equations describing the propagation of the shear and the compression waves at their respective velocities  $C_T$  and  $C_L$ . The compression velocity ( $C_L$ ) is much greater by three orders of magnitude than the shear velocity ( $C_T$ ). These velocities depend on the mean density  $\rho$  and the first and second Lamé's coefficients:

$$C_T = \sqrt{\frac{\mu}{\rho}} \quad \text{and} \quad C_L = \sqrt{\frac{\lambda+2\mu}{\rho}}$$

Practically, the compression wave has time to propagate, reflect several times (getting converted into shear wave) and attenuate, before shear wave propagation really starts. It means that, at the boundaries and interfaces, both waves are intermingled by mode conversion. By considering the divergence free displacement field only ( $\vec{u} = \vec{u}_S$ ), the  $\partial_t 2u = \mu \nabla^2 u + \lambda + \mu \nabla \nabla u + \zeta \partial_t \nabla^2 u + \xi + \zeta \partial_t \nabla \nabla u$ , (3. 12) becomes negligible. To evaluate the contribution of the second term, we have to consider the term  $\nabla(\nabla \vec{u})$  in the Helmholtz decomposition with:

$$\nabla(\nabla \vec{u}) = \nabla(\nabla(\vec{u}_P + \vec{u}_S)) \quad (3. 14)$$

$$\nabla(\nabla \vec{u}) = \nabla(\nabla(\vec{u}_P))$$

$$\nabla(\nabla \vec{u}) = \nabla^2 \vec{u}_P$$

$$\nabla(\nabla \vec{u}) \approx k_P^2 \vec{u}_P = \left(\frac{\omega}{c_P}\right)^2 \vec{u}_P \approx (1 - 2\sigma_p) \vec{u}_P \quad (3. 15)$$

where  $k_P$  is the compression wave vector, and  $\sigma_p \cong 0.4999999$  is the Poisson's ratio.  $\nabla(\nabla \vec{u})$  is very small but the Young's modulus E in organic tissues is in the range of a few  $\partial_t 2u = \mu \nabla^2 u + \lambda + \mu \nabla \nabla u + \zeta \partial_t \nabla^2 u + \xi + \zeta \partial_t \nabla \nabla u$ , (3. 12) cannot be easily neglected as the large magnitude of the second Lamé's coefficient  $\lambda$  balances the small magnitude of the  $\nabla u$  term. The second term on the right-hand side of  $\partial_t 2u = \mu \nabla^2 u + \lambda + \mu \nabla \nabla u + \zeta \partial_t \nabla^2 u + \xi + \zeta \partial_t \nabla \nabla u$ , (3. 12) is as important as the first term. To simplify the problem, we could excite the targeted tissue or organ with a shear wave only, which is almost impossible due to the complexity of living tissues where shear and compression waves are often mode converted. We could instead apply the curl-operator  $\partial_t 2u = \mu \nabla^2 u + \lambda + \mu \nabla \nabla u + \zeta \partial_t \nabla^2 u + \xi + \zeta \partial_t \nabla \nabla u$ , (3. 12) to obtain:

$$-\rho \omega^2 \vec{q} = \mu \nabla^2 \vec{q} + i\omega \zeta \nabla^2 \vec{q}, \quad \vec{q} = \nabla \times \vec{u}, \quad \vec{q} \in \mathbb{C}^3 \quad (3. 16)$$

The two shear viscoelastic parameters  $\mu$  and  $\zeta$  can then be extracted at the cost of solving an  $\omega 2q = \mu \nabla^2 q + i\omega \zeta \nabla^2 q, \quad q = \nabla \times u, \quad q \in \mathbb{C}^3$  (3. 16).

$\omega 2q = \mu \nabla^2 q + i\omega \zeta \nabla^2 q, \quad q = \nabla \times u, \quad q \in \mathbb{C}^3$  (3. 16) consists of six equations (three for the real part and three for the imaginary part of  $\vec{q}$ ) and can be written in a complex form as:

$$-\rho\omega^2\vec{q} = G^*\nabla^2\vec{q}, \quad \vec{q} \propto e^{i\vec{k}\vec{x}}, \quad \vec{q} \in \mathbb{C}^3 \quad (3.17)$$

Where  $\vec{k}$  is the wave vector and  $G^* = G_d + iG_1$  is the complex shear modulus (3.18), with the real part  $G_d$  as shear elasticity modulus ( $\mu$ ) and the imaginary part  $G_1$  divided by the circular frequency  $\omega = 2\pi\nu$  as the shear viscosity modulus ( $\zeta$ ) [137].

Equation (3.17) can be rewritten as:

$$-\rho\omega^2\vec{q} = -G^*k^2 \cdot \vec{q} \quad (3.18)$$

and finally

$$G^* = \frac{\rho\omega^2}{k^2}. \quad (3.19)$$

The complex wave vector can be written as:

$$k = \beta + i\alpha \quad (3.20)$$

where  $\beta$  represents the propagation and  $\alpha$ , the attenuation. We can express the shear elasticity ( $G_d$ ) and the shear viscosity ( $G_1$ ) as a function of the wave propagation and attenuation.

Rewriting equation (3.19) with  $\beta$  and  $\alpha$ , and multiplying by the complex conjugate, we have

$$G^* = \frac{\rho\omega^2}{(\beta+i\alpha)^2} \cdot \frac{(\beta-i\alpha)^2}{(\beta-i\alpha)^2} \quad (3.21)$$

and finally

$$G^* = \frac{\rho\omega^2 \cdot (\beta^2 - \alpha^2 - 2i\alpha\beta)}{(\beta^2 + \alpha^2)^2} \quad (3.22)$$

As  $\beta = 2\pi/\lambda$ ,  $G_d$  and  $G_1$  are respectively:

$$G_d = \rho\omega^2\lambda^2 \cdot \frac{(4\pi^2 - \alpha^2\lambda^2)}{(4\pi^2 + \alpha^2\lambda^2)^2} \quad (3.23)$$

$$G_1 = -i\rho\omega^2\lambda^3 \cdot \frac{4\pi\alpha}{(4\pi^2 + \alpha^2\lambda^2)^2} \quad (3.24)$$

In the lung, the density  $\rho$  is not homogenous and it is usually much lower than the water density,  $\rho = 1$ . As a consequence, density mapping is necessary to properly evaluate the viscoelastic moduli. Density correction could be performed accordingly during processing, or later, directly onto the extracted shear viscoelastic moduli.

---

### 3.3. Magnetic Resonance Elastography of the lung

Initiated by Ehman's group at Mayo clinic in 2006, MR elastography of the lungs was born with two great intrinsic issues related, first, to the visualization of the organ by NMR and, second, to the extrapolation of the tissue shear moduli from the gas displacement field. For the first issue, the solution followed here was the implementation of hyperpolarized helium-3 MRI, even though it brings up other issues like the hyperpolarized signal life and the gas diffusion. The second issue comes as a real challenge to prove the feasibility of the technique.

#### 3.3.1. Hydrogen Magnetic Resonance Elastography

In 2006, Mayo Clinic applied hydrogen MRE technique on an excised pig lung. First, while applying a shear movement onto the excised lung for three different inflation volumes, given by 4, 11.5, and 19.5 cmH<sub>2</sub>O at the lung inlet, they measured the corresponding increasing stiffness in the parenchyma (0.8, 1.53, and 3.2 kPa, respectively). Second, they performed hydrogen lung MRE *in vivo* on a healthy volunteer to demonstrate the presence of mode-converted shear waves while a mechanical excitation was being applied onto the lung with an external driver placed on the subject's chest [4]. However, in spite of the beautiful proof of concept with a clear increase of the overall pig lung shear stiffness with respect to the inflation volume, the extracted regional values throughout the lung did not reveal any expected structures of the respiratory system, like the bronchial tree, which is supposed to be stiffer than the alveolar region. Moreover, the *in vivo* propagation of shear waves could be checked only on the peripheral right lung, where the mechanical driver was fixed.

#### 3.3.2. Helium-3 Magnetic Resonance Elastography

In 2006, in their first experiments, Mayo Clinic also performed MRE in a phantom with thermally polarized helium-3. The goal was to demonstrate the basic assumption of gas confinement supporting helium-3 MRE in the lungs [4]. The phantom was a silicon tube, filled with open-celled foam, inserted into a polyethylene terephthalate bottle. It was filled by thermally polarized helium-3, which diffused in the bottle and in the tube, while shear waves were generated by a device coupled to the container top. The results showed that even though the gas signal was lower in the foam-filled silicon tube than outside the tube in the bottle – as it was expected for the lower gas density inside the tube – it was possible to obtain an image [4]. However, the assumption on gas confinement still remained partially open, as it was only qualitatively tested and, even if the gas was confined in the foam, the pressure was

345 kPa, rather far from physiological conditions. Moreover, a secondary assumption on gas content independence was not tested.

In 2008, on an excised pig lung, they performed hyperpolarized helium-3 MRE, monitoring the shear wave propagation along the four phase offsets, measuring the wave propagation far from the excitation driver source. In the resulting elastograms, the measured elasticity was much higher, up to 15 kPa, than the values measured in previous *ex vivo* experiments by Lai-Fook *et al.* [6], where the shear modulus was found smaller than 1.6 kPa [5]. Those elastograms did not sustain the expected lung anatomy.

## **Chapter 4.           Validity of helium-3 Magnetic Resonance Elastography**

### **4.1. Introduction**

Helium-3 MRE relies on the primary assumption that the motion of the tracer gas faithfully reflects the motion of the surrounding tissue. In other words, we assume the gas is confined enough in the airways such that the mechanical vibrations induced in the lung parenchyma linearly drive the gas molecules in the respiratory system into a similar oscillatory motion. This assumption is true either as long as the timeframe of the gas motion itself, which is induced by the gas own diffusivity, is longer than the period of the oscillatory motion of the airway walls – probably in the larger airways – or as long as the gas diffusion is fast enough so the gas motion itself is averaged out– especially in the alveolar spaces – over a mechanical oscillation period to a single mean position.

Helium-3 MRE holds over the respiratory cycle and any respiratory situations if the composition of the gas in the airways, which is artificially changed by the adjunction of a tracer gas and which naturally, in lesser proportions, varies. This means helium-3 MRE also relies on the secondary assumption that the mechanical properties of the respiratory system are not affected by the gas content of the airways. This assumption should hold as long as the spatial resolution of the MRE acquisition remains larger than the involved airway spaces, namely as long as the local density is governed by the tissue density so the measured local gas-tissue density is not significantly changed by an even radical shift of the gas density. The viscoelastic properties of the lung parenchyma are then expected to only depend on tissue mechanics.

In this chapter, we demonstrate in controlled conditions, with an experimental lung model, the validity of helium-3 MRE by proving first the fluid/structure coupling is effective in the airways, then the mechanical properties of the lung parenchyma do not depend on the gas content. Hence both helium-3 and hydrogen MRE were performed on the exact same system model to compare the mechanical properties of the lung parenchyma as extracted from gas and tissue MRE. The composition of the gas inside the system model was varied while performing hydrogen MRE.

The mechanical properties of the respiratory system highly depend on the biological condition of the organs involved. As we will see in the next chapter, they obviously depend on the degree of lung inflation, hence on the phase within the respiratory cycle. They also depend on the subject's physical condition and position. All these conditions are difficult to control and to reproduce *in vivo*. A system model had to be developed to ensure that mechanical conditions may be controlled and reproduced and that gas content may be changed.

The complex pulmonary structure, a fully interconnected porous medium with one single input for a few hundred million ending alveolar spaces, is quite hard to reproduce as it looks like a tree with the bronchial ramifications, surrounded by a spongy tissue in the distal area, constrained in the pleural cavities. Such a system is not artificially available. So the model system we developed used excised lungs placed either (i) in a container filled with a mixture of water and a surfactant to simulate the *in vivo* boundary and pressure conditions of the lungs in the chest or (ii) confined in a silicone mold. In the first design with liquid boundary conditions, pressure waves, generated by a remote loudspeaker, were guided down to the trachea lumen to induce mechanical waves throughout the lung. In the second design with solid boundary conditions, mechanical waves were coupled to the lungs by the application of an oscillating piston directly onto the silicon mold. In such system models, we could reproduce, with high confidence, pressures, volumes, and positions of the imaged lung over the numerous acquisitions required for hydrogen and helium-3 MRE in various imposed conditions and with various buffer gases.

---

## 4.2. Primary assumption for helium-3 MRE: Gas confinement in the lung

### 4.2.1. Introduction

The assumption of alveolar confinement of the gas is necessary for helium-3 MRE. In this work, the viscoelastic properties of an excised pig lung were quantitatively evaluated and compared both with helium-3 and hydrogen MRE.

### 4.2.2. Materials and methods

Every experiment was performed on a system model specifically designed to achieve the same physical conditions (pressure, volume, position) for both MRE modalities when the lung is filled with hyperpolarized helium-3 or with air. The system model is based on a BioQuest<sup>®</sup> excised pig lung (Nasco International, Fort Atkinson, Wisconsin). Once excised, the pig lung is processed following non-standard fixation techniques [138] in order to preserve organic tissue with viscoelastic properties close to the original ones *in vivo*. The process includes a two-week curing of the lung in a cooled tank with constant circulation of brine that is eventually replaced over by propylene glycol.

The left lung of the BioQuest<sup>®</sup> model was inserted in a rigid altuglas<sup>®</sup> cylinder sealed on both ends (Fig.4. 1). The cylinder was filled with a preserving mixture of water and propylene glycol to avoid degradation of the specimen and, at the same time, to simulate the liquid boundary in the pleural cavities around the lungs in physiological conditions. The trachea was connected, on the inner side of one of the two end caps of the casing, to a feedthrough tube (Fig.4. 1-4), in order to let gas in and out of the organ. A second feedthrough tube, controlled with a tap (Fig.4. 1-5), on the second end cap, was connected to a second vertical altuglas<sup>®</sup> cylinder to supply the liquid boundary surrounding the lung in the casing and to control the lung volume, pressure and gas filling. The partially-filled cylindrical tank was marked with volume scales in milliliters and centimeters (Fig.4. 1-1). Its upper end could be opened to the atmosphere or to a vacuum line (Fig.4. 1-3) in order to impose a positive or negative pulmonary pressure to either deflate or inflate the lung by pushing gas out or letting gas in through the open trachea (Fig.4. 1-2). Once a given lung inflation state was reached, the tap on the connecting line could be closed to simulate an arbitrary-long apnea (Fig.4. 1-7).

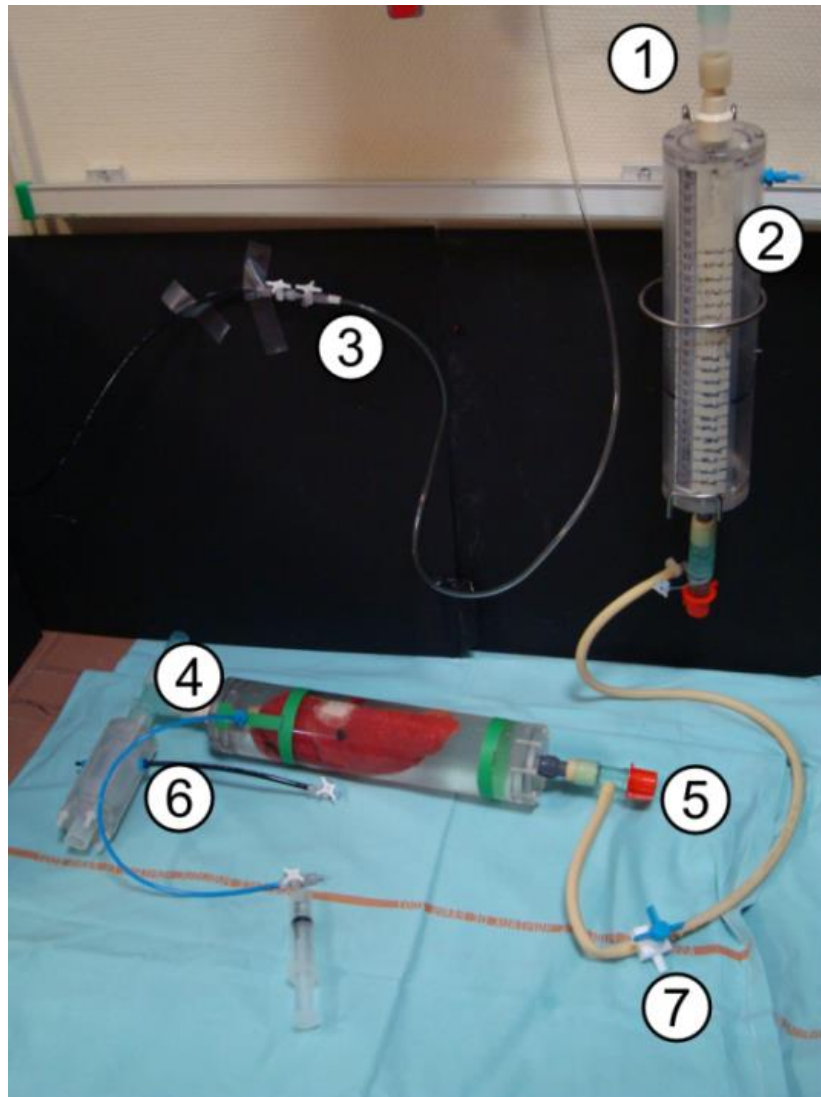


Fig.4. 1: Setup for a system model with liquid boundary conditions based on a BioQuest<sup>®</sup> excised pig lung. 1. Atmospheric pressure releasing valve 2. Vacuum valve 3. Vacuum line 4. Tracheal port 5. Outer lung pressure line 6. Constriction valve for helium-3 administration 7. Safety tap

#### 4.2.2.1. MRE sequence acceleration

A motion-sensitized spin-echo sequence was used for hydrogen MRE and a motion-sensitized gradient-echo sequence was used for helium-3 MRE. To reduce the total acquisition time for both modalities and enhance the available helium-3 NMR signal in each acquired k-line, the k-space was only partially acquired, 52%, along the phase direction (Half-Scan, HS). To furthermore enhance the helium-3 NMR signal, the k-space was also partially acquired, 52%, along the measurement direction (Partial-Echo, PE).

Potential artifacts on the outcomes of such partial-acquisition approaches were tested beforehand on a polyvinyl alcohol (PVA) cylinder of 20 cm high and 20 cm diameter. It was mechanically excited by a pressure wave guided directly onto its surface at a low resonant frequency of the pressure excitation system, 57 Hz. Hydrogen MRE was performed with partial acquisitions, over the range of 52% and 100%, along both phase and measurement directions (HS and PE). Zero-filling was applied to the partial k-space data for both reduced dimensions before images were reconstructed. The resulting image phase maps were compared to the image phase map of the reference full acquisition (HS = 100% and PE = 100%).

#### 4.2.2.2. Hydrogen MRE

The pig lung phantom was placed, orthogonally to the bore axis, in the center of a 1.5 T Achieva scanner (Philips Healthcare, Best, The Netherlands) equipped with multi-nuclei capability. Two dual Flex-M coils were fitted around the containing cylinder, parallel and orthogonal to its axis. The lung was inflated to the set volume imposed by the extraction of 400 mL of liquid and an apnea was forced by closing the safety tap. The pressure waveguide was connected to the tracheal port and the MRE acquisitions triggered the function generator for the synchronization of the propagation of the exciting mechanical wave at 118 Hz. The spin-echo sequence was implemented with 19 slices in a FOV of  $(320 \times 80 \times 76)$  mm<sup>3</sup> with an isotropic 4 mm spatial resolution for  $f_0 \approx 63.8$  MHz,  $\alpha = 90^\circ$  and  $TE/TR = 30/804$  ms. Motion sensitizing gradients were applied with an intensity of  $21 \text{ mT}\cdot\text{m}^{-1}$  along the three spatial FOV dimensions. Eight snap-shots of the propagating wave during one oscillatory cycle were acquired. With an acceleration factor close to 1.6 (HS = 0.62 and PE = 0.62), the overall acquisition time for each motion encoding direction was 79 s.

An additional anatomical scan was acquired in the same conditions with the same FOV but an improved 2 mm isotropic voxel and  $TE/TR = 7.6/220$  ms to establish relative density-weighted maps of the imaged lung.

Finally, a generic high resolution anatomical scan was acquired once the lung was partially inflated with 200 ml of air to reveal the inner anatomical structures of the BioQuest<sup>®</sup> pig lung phantom with a 0.5 mm isotropic voxel and  $TE/TR = 30/3234$  ms.

#### 4.2.2.3. Hyperpolarized helium-3 MRE

The excised pig lung phantom was set up for helium-3 MRE in the center of the 1.5 T Achieva scanner in the same way as it was for hydrogen MRE. Dual Flex coils were replaced by a home-made double bracelet Helmholtz coil (Fig.4. 2-a).

The lung was inflated with a gas mixture containing 100 mL of polarized helium-3 and an estimated dose of 300 mL of sulfur hexafluoride ( $SF_6$ ) up to the total 400 mL volume of liquid extracted from the phantom container.  $SF_6$  was employed here as a heavy buffer gas to minimize gas diffusion of the resulting mixture  $^3He-SF_6$ , namely, to minimize signal attenuation due to diffusion in the strong motion-sensitizing gradient of the MRE sequence, and, to consequently maximize the SNR of hyperpolarized helium-3 MRE.

Helium-3 gas was polarized up to 69–71% by metastability exchange optical pumping at the Physics Department of Mainz University, Germany. It was then stored in 3 bar glass cells and put in a special transport box [82] that mechanically protects the cells and magnetically maintains with a permanent internal magnetic field the gas hyperpolarization over a couple hundreds of hours (Fig.4. 2-b). It was finally shipped by airfreight to CIERM, Le Kremlin-Bicêtre, France. Batches of 100 mL of hyperpolarized helium-3 were transferred on site from the glass cells to a transport Tedlar<sup>®</sup> bag (SKC, Eighty Four, PA, USA) and mixed with sulfur hexafluoride. The transport bag was then connected to the non-magnetic, non-depolarizing, pressure-controlled constriction valve in the scanner (Fig.4. 1-6). The prepared dose was administered to the pig lung phantom through the tracheal port and an apnea was forced just before launching the MRE acquisition.

The gradient-echo sequence was implemented, with the same parameters as for hydrogen MRE, over 19 slices,  $FOV = (320 \times 80 \times 76)$  mm<sup>3</sup> with an isotropic 4 mm spatial resolution, but at  $f_0 \approx 48.6$  MHz and with  $\alpha = 10^\circ$  and  $TE/TR = 13/17$  ms. Four snap-

shots of the propagating wave were acquired per oscillatory cycle along the three spatial directions; for each spatial direction, a bolus of 100 mL of helium per volume was transferred. With the same 1.6 acceleration factor ( $HS = 0.62$  and  $PE = 0.62$ ), the overall acquisition time of each motion encoding direction was reduced to 7 s.

After each acquisition, the safety tap and the releasing valve were open to let the lung deflate. The expired gas was recovered for later recycling the depolarized helium-3 once compressed and sent back to Mainz University.



Fig.4. 2 (a) Home-made double bracelet Helmholtz RF coil used for hyperpolarized helium-3 experiments at  $f_0 \approx 48.6$  MHz. (b) Glass cells of 1 L at 3 bar pressure in the transport box where a homogenous permanent magnetic field preserves the gas hyperpolarization.

For every MRE and MRI acquisitions, the measurement axis was along the longest lung head-feet dimension while the phase axis was along the lung antero-posterior dimension and the slice axis, along the lung right-left dimension. Hence, according to the organ position *in vivo* in the body, sagittal slices of the pig lung phantom were recorded.

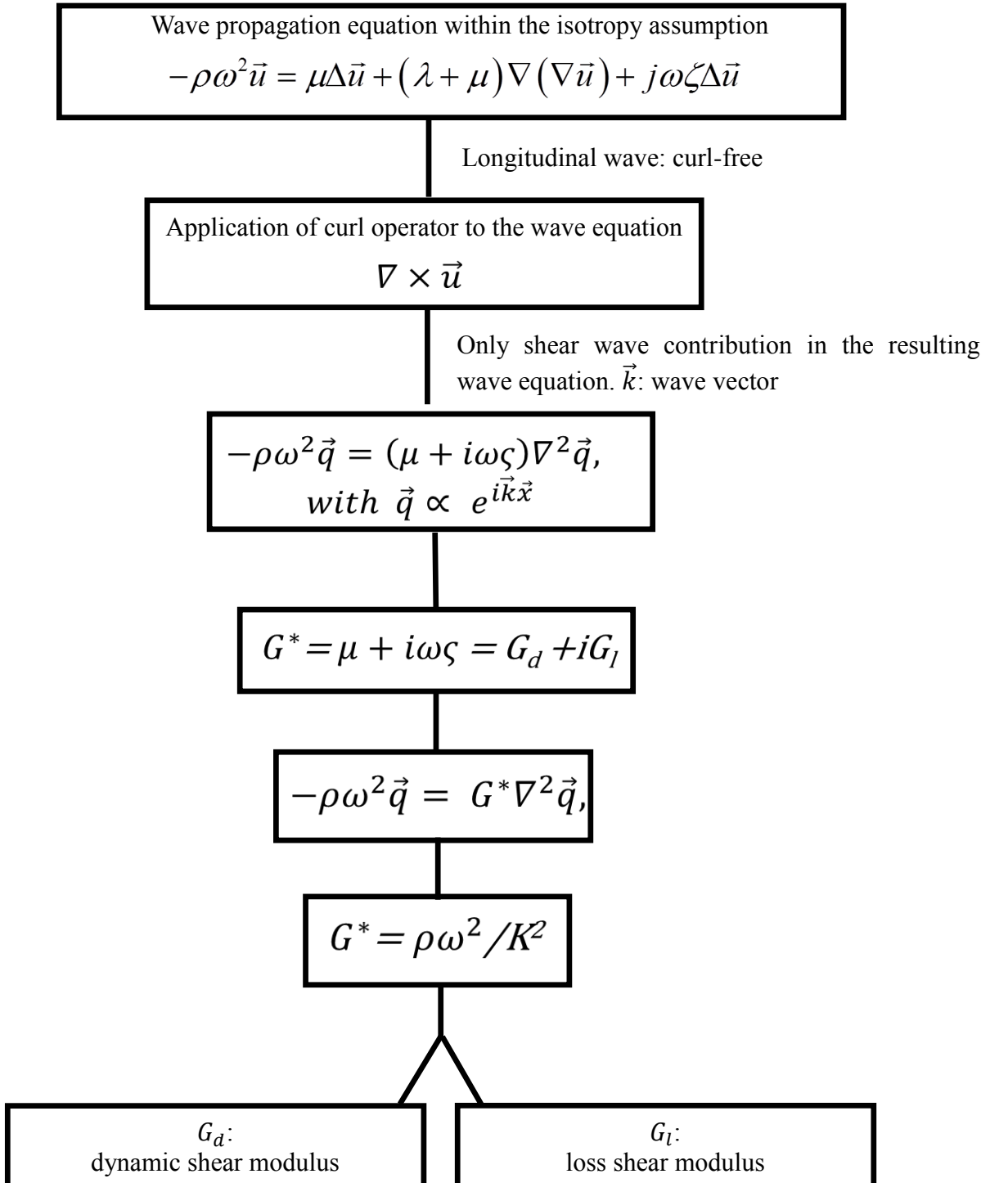
#### 4.2.2.4. MRE data processing

Two masks were applied before reconstruction. First, by thresholding the mean magnitude of the sets of images acquired in the three spatial directions, a common 3D mask of the lung was defined for hydrogen and helium-3 MRE data. Second, the large airways, down to a few bronchial generations, were manually segmented and removed from the former mask to generate a 3D mask of the pulmonary tissue. For both hydrogen and helium-3 MRE, the 3D maps of the tissue density were calculated from the high resolution magnitude of hydrogen density-weighted anatomical scans.

Raw MRE complex data were masked, density-weighted, and processed by a dedicated software [136], [137]. Raw phase maps were unwrapped in two dimensions for each slice before the resulting unwrapped 2D phase maps were aligned in time and in the third spatial dimension. The 3D displacement field was then calculated from the unwrapped 3D phase maps along the three motion-encoded directions according to Eq. (3. 19). Maps of the

amplitude and phase of the 3D displacement field were inferred along each spatial direction from fitting its temporal evolution over the acquired snapshots at selected time offsets. Visualization of shear wave propagation was enhanced on temporally-extrapolated displacement field fits. The related tissue mechanical properties were subsequently inferred along the scheme below: 3D maps of the shear wavelength ( $\lambda$ ), the dynamic ( $G_d$ ) and loss ( $G_l$ ) shear moduli.

Data processing and equation inversion scheme:



Mean values and standard deviations of the shear wavelength and the shear viscoelastic moduli were then calculated over the two masks, with and without the large airways, for the whole lung and for each slice using Matlab<sup>®</sup>.

### 4.2.3. Results

#### 4.2.3.1. MRE sequence acceleration

Phase maps of the central slice of the cylindrical PVA phantom are given in Fig. 4. 3 for a full acquisition (Fig. 4. 3-a) and for a partial acquisition (Fig. 4. 3-b) with an acceleration factor close to 1.6 (HS = 60%) as an example. A few artifacts appeared along abrupt phase changes, typically when the phase is wrapped as clearly delineated on the phase error map (Fig. 4. 3-c). Otherwise, the results show that a twofold acceleration (HS = 52%) is easily achieved while keeping any introduced small phase errors. Similar results were obtained for partial echo acquisitions down to PE = 52% with negligible added phase errors. Even though the acquisition times are not significantly reduced with partial echo acquisitions – the acceleration factor is close to 1 for any PE values – the echo time is efficiently reduced so hyperpolarized helium-3 NMR signal is improved thereafter.

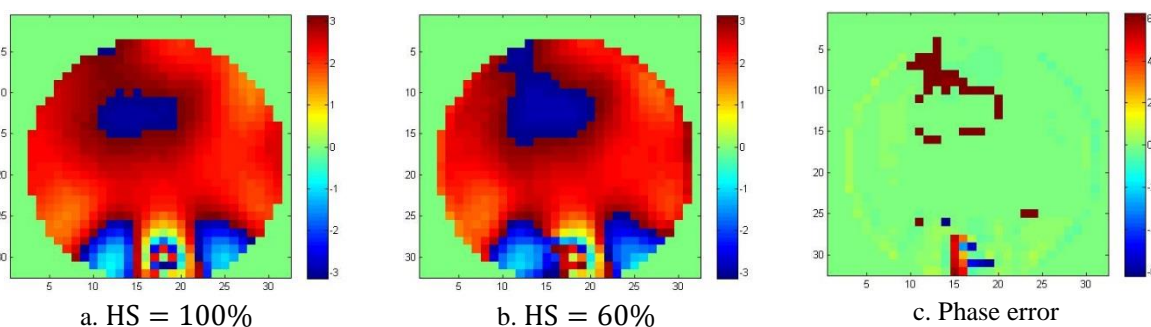
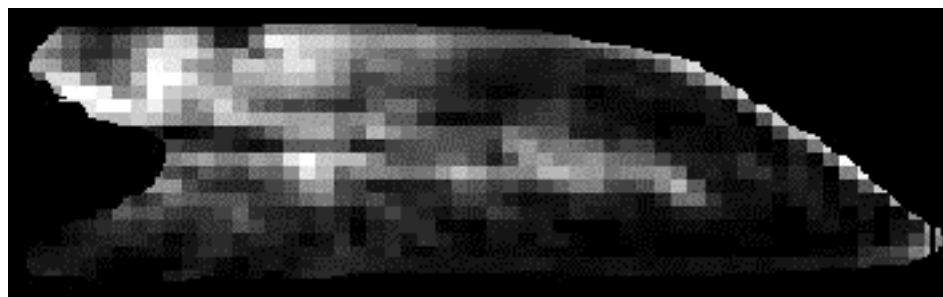


Fig.4. 3: Phase maps of the central slice of the cylindrical PVA phantom for the reference full acquisition (a) and for a partial acquisition with a 1.6 acceleration factor (HS = 60%) (b). Phase error map (c) as phase difference between (a) and (b).

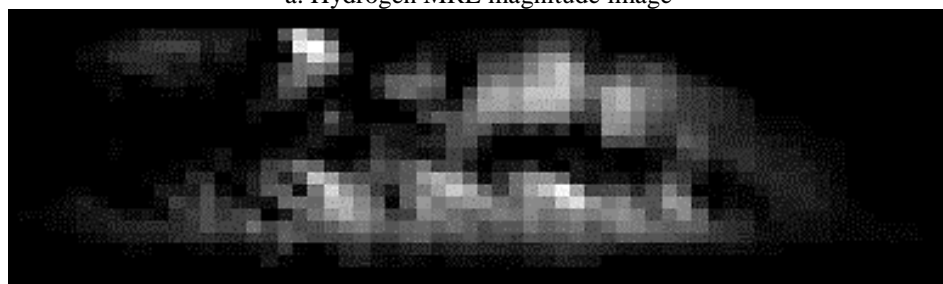
#### 4.2.3.2. Hydrogen and helium-3 MRE

Fig.4. 4 shows the masked mean magnitude images of the central slice of the pig lung phantom for hydrogen MRE (Fig.4. 4-a) and helium-3 MRE (Fig.4. 4-b) when the motion encoding gradient was applied along the measurement direction, i.e. the horizontal axis of the image, and (Fig.4. 4-c) the corresponding MRI anatomical scan. While acquisition times differ for the two MRE modalities by an order or magnitude: 79 s for hydrogen MRE and 7 s

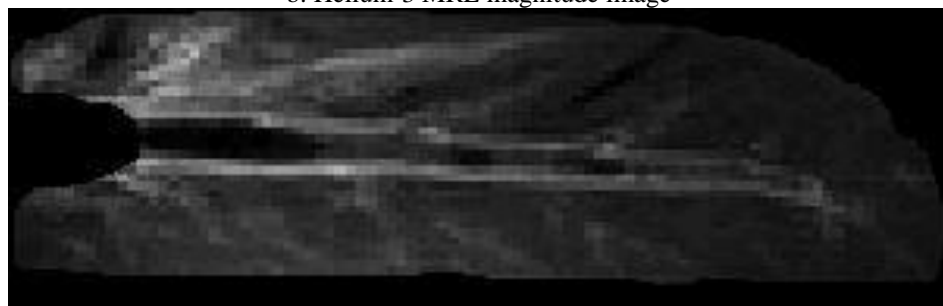
for helium-3 MRE, global mean signal to noise ratios are very similar: 23 for hydrogen and 21 for helium-3.



a. Hydrogen MRE magnitude image



b. Helium-3 MRE magnitude image

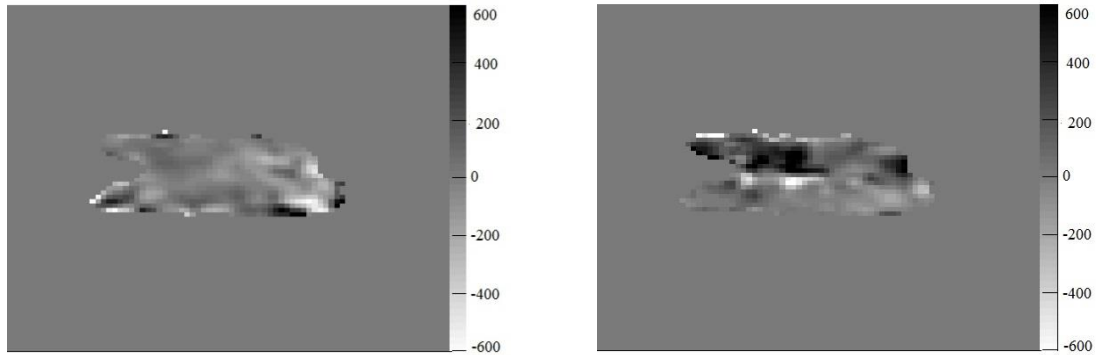


c. Anatomical MRI magnitude image

Fig.4. 4 Magnitude images of a preserved pig lung (central slice) with FOV =  $(320 \times 80 \times 76)$  mm<sup>3</sup> and isotropic 8 mm voxels. (a) Magnitude image of the central 4 mm thick slice of the pig lung obtained by hydrogen MRE for motion encoding gradient along the measurement axis, the image horizontal dimension. (b) Magnitude image of the central 4 mm thick slice of the pig lung obtained by helium-3 MRE for motion encoding gradient along the measurement axis, the image horizontal dimension. (c) Magnitude image of the averaged two central 2 mm thick slices of the pig lung obtained by <sup>1</sup>H MRI. The acquisition time was of 568 s.

The intensity of the hydrogen MRE signal magnitude reflects the tissue density. It is higher for the walls of the larger airways and it is lower in the distal alveolar regions of the lung. On the contrary, for helium-3 MRE, like for a negative image, the distal alveolar regions of the lung, where the gas usually ends up, show higher signal intensity while the large airways, where the signal is impaired by gas diffusion, barely show any signal. The airway structure, revealed on the anatomical, matches the signal amplitudes of the above images. The normalized magnitude was used as a tissue density map for MRE reconstructions.

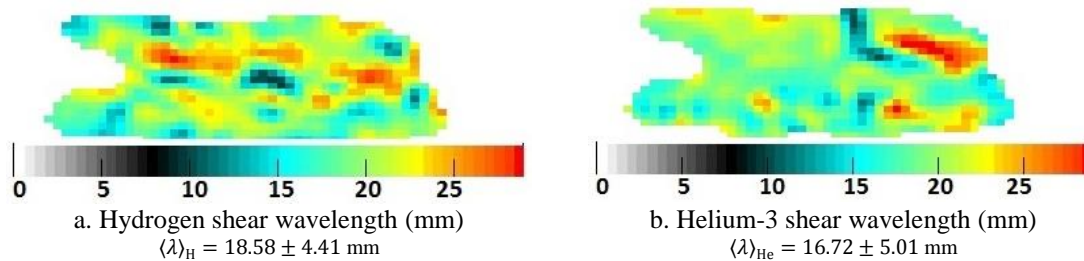
A snapshot of the 3D shear displacement field maps in the tissue and in the gas are also presented for the central slice in Fig.4. 5-a and b, respectively. The calculated wavelength maps ( $\lambda$ ) in the tissue and in the gas follow in Fig.4. 6.



a. Hydrogen shear displacement map ( $\mu\text{m}$ )

b. Helium-3 shear displacement map ( $\mu\text{m}$ )

Fig.4. 5: Shear displacement maps for a given phase offset in the 4 mm thick central slice of a BioQuest<sup>®</sup> pig lung phantom (a) for hydrogen MRE and (b) for helium-3 MRE.



a. Hydrogen shear wavelength (mm)

b. Helium-3 shear wavelength (mm)

$$\langle \lambda \rangle_{\text{H}} = 18.58 \pm 4.41 \text{ mm}$$

$$\langle \lambda \rangle_{\text{He}} = 16.72 \pm 5.01 \text{ mm}$$

Fig.4. 6: Shear wavelength maps in the 4 mm thick central slice extracted from a BioQuest<sup>®</sup> pig lung (a) for hydrogen MRE and (b) helium-3 MRE.

The differences in shear wavelength between the two modalities come from the origin of the NMR signal, which is weighted by the tissue density in hydrogen MRE, dominated in large airways by stiffer tissue, and by the gas density in helium-3 MRE, dominated in distal airways, where the gas is confined, by compliant tissue.

The reconstructed maps of shear dynamic and loss moduli,  $G_d$  and  $G_l$ , of the pig lung phantom are presented on Fig.4. 7.

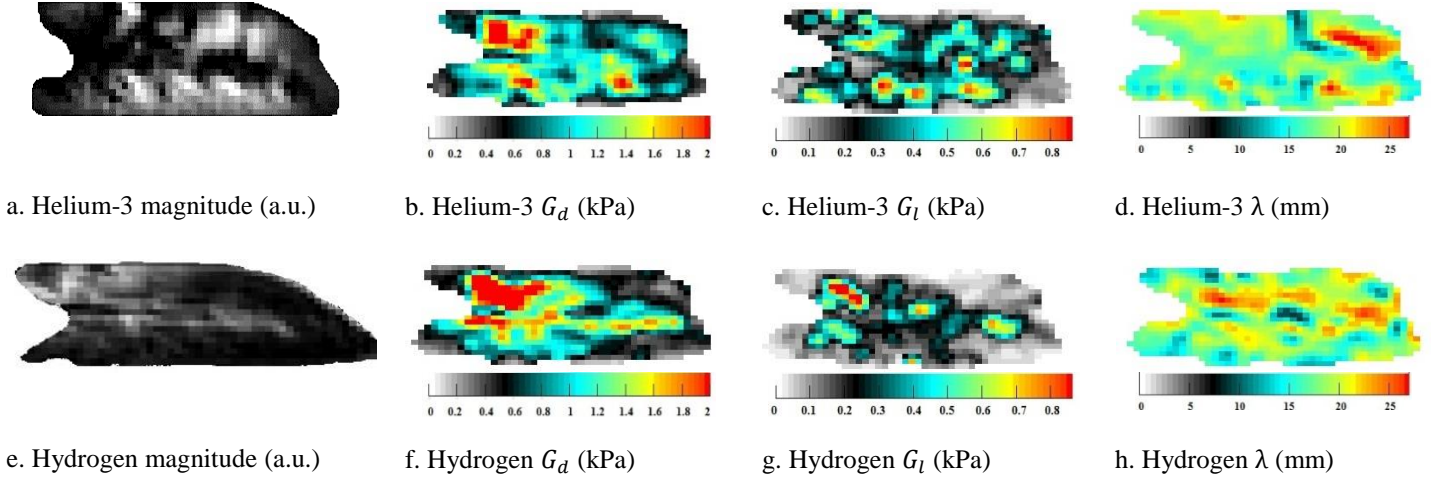


Fig.4. 7: (a,e) Magnitude amplitudes, (b,f) shear dynamic moduli, (c,g) shear loss moduli, and (d,h) shear wavelength maps in the central slice of a preserved BioQuest<sup>®</sup> pig lung for helium-3 and hydrogen MRE, respectively.

Pulmonary structures are revealed by both modalities but shear moduli are lower in the proximal airways and greater in the distal airways for helium-3 MRE than for hydrogen MRE.

As summarized in Tab.4 1, the calculated global mean values over the whole lung are  $\langle G_d \rangle_H = (1.25 \pm 1.17)$  kPa and  $\langle G_l \rangle_H = (0.49 \pm 0.67)$  kPa, with hydrogen MRE, and  $\langle G_d \rangle_{He} = (0.89 \pm 0.68)$  kPa and  $\langle G_l \rangle_{He} = (0.32 \pm 0.31)$  kPa, with helium-3 MRE.

	Dynamic shear modulus	Loss shear modulus	Wavelength
Hydrogen MRE	$(1.25 \pm 1.17)$ kPa	$(0.49 \pm 0.67)$ kPa	$(18.58 \pm 4.41)$ mm
Helium-3 MRE	$(0.89 \pm 0.68)$ kPa	$(0.32 \pm 0.31)$ kPa	$(16.72 \pm 5.01)$ mm

Tab.4 1: Global mean values of the viscoelastic moduli in a preserved BioQuest<sup>®</sup> pig lung. The values recorded in hydrogen are slightly higher than the ones recorded in helium-3.

The wall structures of the main airways, where helium-3 cannot be confined, may affect the measure of the viscoelastic properties in hydrogen such that the shear viscoelasticity moduli are enhanced with respect to those measured in helium-3. Once the large airways are removed, the calculated global mean values over the pulmonary tissue are then reduced to  $\langle G_d \rangle_H = (0.79 \pm 0.83)$  kPa and  $\langle G_l \rangle_H = (0.28 \pm 0.43)$  kPa, for hydrogen MRE, and  $\langle G_d \rangle_{He} = (0.72 \pm 0.90)$  kPa and  $\langle G_l \rangle_{He} = (0.23 \pm 0.75)$  kPa, for helium-3 MRE. The corresponding global mean wavelengths are then  $\langle \lambda \rangle_H = (15.41 \pm 5.73)$  mm and  $\langle \lambda \rangle_{He} = (14.44 \pm 6.33)$  mm (**Erreur ! Source du renvoi introuvable.**).

	Dynamic shear modulus	Loss shear modulus	Wavelength
Hydrogen MRE	$(0.79 \pm 0.83)$ kPa	$(0.28 \pm 0.43)$ kPa	$(15.41 \pm 5.73)$ mm
Helium-3 MRE	$(0.72 \pm 0.90)$ kPa	$(0.23 \pm 0.75)$ kPa	$(14.44 \pm 6.33)$ mm

Tab.4 2: Global mean values of the shear viscoelastic parameters,  $G_d$ ,  $G_l$ , and  $\lambda$ , over the lung parenchyma of a preserved BioQuest® pig lung, once the main airways (first and second generations of the bronchi) are excluded, so that only the parenchyma and bronchioles contributions are considered.

In Fig.4. 8, mean values,  $\langle G_d \rangle_{H/He}^{sl}$  and  $\langle G_l \rangle_{H/He}^{sl}$ , and a fourth of the standard deviation,  $\delta_{dH/He}^{sl}$  and  $\delta_{lH/He}^{sl}$ , for each slice, are plotted from right to left sagittal slices.

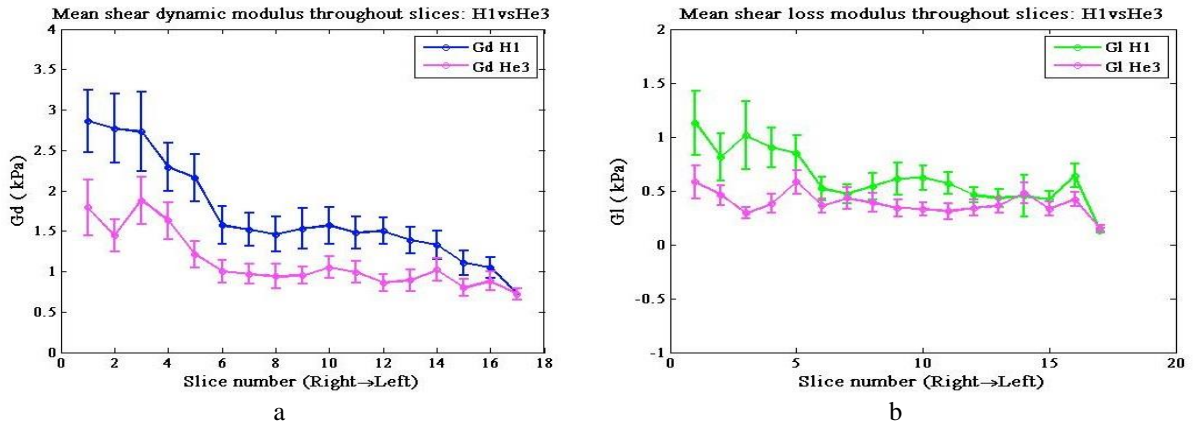


Fig.4. 8: Evolution of the mean shear (a) dynamic  $\langle G_d \rangle_{H/He}^{sl}$  and (b) loss moduli  $\langle G_l \rangle_{H/He}^{sl}$  for helium-3 and hydrogen MRE across the lung slices from right to left in a preserved BioQuest® pig lung. The bars,  $\delta_{dH/He}^{sl}$  and  $\delta_{lH/He}^{sl}$ , correspond to a fourth of the standard deviation over each slice.

Even though they follow the same trend, shear moduli are lower for helium-3 MRE than for hydrogen MRE as expected by the relative tissue and gas density weightings.

Finally, Fig.4. 9 shows the magnitude image of the central slice obtained with the high resolution anatomical scan on the deflated preserved BioQuest® pig lung.

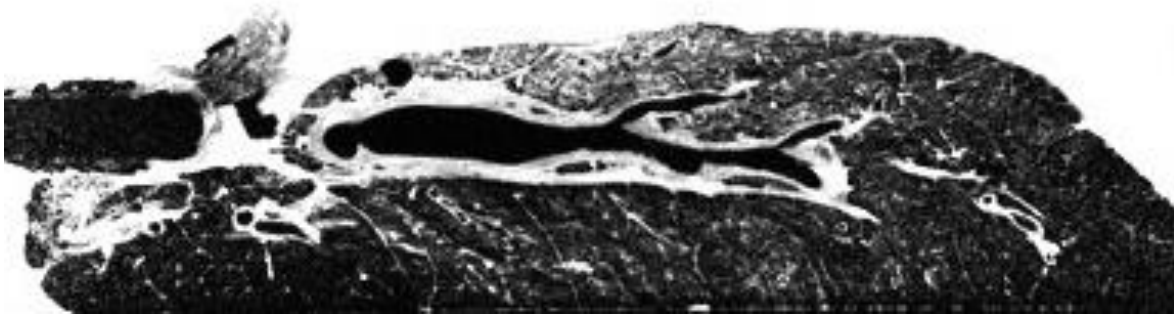


Fig.4. 9: High resolution magnitude image of the 0.5 mm central slice of the deflated BioQuest® pig lung obtained by hydrogen MRI.

Lung structures may easily be delineated and the revealed wall thickness of large airways explains fairly well the magnitude images obtained with hydrogen or helium-3 as well as the differences between the maps of shear moduli extracted with hydrogen and helium-3 MRE.

#### 4.2.4. Discussion

Lung anatomy is clearly but very differently revealed by the 3D magnitude images obtained with standard MRI (Fig.4. 7-c), hydrogen MRE (Fig.4. 7-a), and helium-3 MRE (Fig.4. 7-b). As shown for the central slice in the preserved BioQuest® pig lung on Fig.4. 7, the proximal large airways are underlined by enhanced signal intensity that originates from the higher hydrogen density expected along the thick walls of the trachea and the bronchial tree. Accordingly, the distal small airways appear with a much lower signal intensity, which corresponds to the local lower hydrogen density of the lung parenchyma. On the contrary, on helium-3 magnitude images, the parenchyma shows enhanced signal intensity as the alveolar spaces were filled with gas at the desired lung inflation volume. However, even though the proximal large airways were effectively filled with gas, the very low signal intensity in the bronchial tree contrasts with the surrounding parenchyma. This signal loss results from the important gas motion – induced by the guided pressure wave and the nearly-free diffusion throughout the large airways – in the magnetic field gradients of the MRE acquisition. Hence, helium-3 magnitude images are not exactly the negative images of the hydrogen magnitude images. The high resolution magnitude image (Fig.4. 4-c) confirms the anatomy of the lung structure; it underlines the large airways and the dominant role of the thickness of the airway walls in the determination of the viscoelastic properties in the vicinity of the bronchial tree.

For the two MRE modalities, shear wave propagation was recorded either in the lung tissue or in the gaseous medium. The guided pressure wave is effective in both cases. It provides

rather homogenous displacement amplitude maps over the lung. Measured shear displacements (Fig.4. 5) could reach values close to  $0.4 \mu\text{m}$  while the latter fell down by more than an order of magnitude in reference MRE acquisitions without motion sensitizing gradient nor mechanical excitation.

The maps of the shear wavelength look similar for both hydrogen and helium-3 MRE as illustrated for the central slice on (Fig.4. 6). However the hydrogen-based map show higher values close to the main airway structures (Fig.4. 6-a) whereas the greatest values in the helium-3-based map are in the parenchyma and from the surrounding of the bronchial tree region (Fig.4. 6-b). The same comments hold for the viscoelastic,  $G_d$  and  $G_l$ , maps (Fig.4. 7). The measurement bias on the global mean values is between 10 to 30% for the shear wavelength and the complex shear moduli, respectively (Tab.4 1). For helium-3 MRE, there is no contribution of the large airways in the reconstruction process as there is simply no signal from those regions. On the contrary, for hydrogen MRE, the signal, hence the contribution, of the large airways is predominant. This bias is obvious on the plot of the shear dynamic and loss moduli across the 17 reconstructed slices (Fig.4. 8): The plots follow the same trend but the helium-3-based slice mean values are systematically lower by a few hPa than the hydrogen-based slice mean values. Moreover, this bias diminishes while approaching the peripheral slices, away from the trachea and the large airways [5]. Once the lung was segmented into the bronchial tree and the parenchyma regions, the measurement bias could be reduced to 6%, 8%, and 17% for the shear wavelength, the dynamic shear modulus, and the loss shear modulus, respectively (Tab.4 2).

As far as an absolute quantitative measurement is concerned, the dynamic shear moduli obtained in the two MRE modalities, for an intermediate volume of 400 ml, fall within the range of stiffness values found by Lai-Fook and Hyatt [6], who studied the incidence of age on the dynamic shear modulus of human lungs. They found that human dynamic shear modulus *ex vivo* is within 0.2 kPa (for a pressure of 4 cmH<sub>2</sub>O at residual volume) and 1.6 kPa (for a pressure of 16 cmH<sub>2</sub>O at 90% of the total lung volume). In this work, the transpulmonary pressure is unknown, but from the works of Lai-Fook *et al.* and McGee *et al.*[4], [5], one can infer that when the volume and the pressure are increased or decreased, the shear modulus accordingly increases or decreases. The volume of 400 ml used in this work is certainly inferior to the 90% of the total lung volume used by Lai-Fook and Hyatt, so the pressure should also be smaller than 16 cm H<sub>2</sub>O. Finally, the global mean values of the dynamic shear modulus (Tab.4 2) agree fairly well with those found by Lai-Fook and Hyatt.

Overall, helium-3 MRE provided solid and quantitative measurements of the regional mechanical properties in a preserved BioQuest<sup>®</sup> pig lung. Three-dimensional maps of the dynamic and loss shear moduli obtained throughout the lung parenchyma where gas signal could be recorded agreed with the values inferred by hydrogen MRE. Thus the primary assumption on gas confinement, which lies behind the new modality, is validated.

Finally, in these experiments, the acquisition times for hydrogen and helium-3 MRE were 79 s and 7 s per spatial motion encoding direction (measurement, phase, and slice), respectively. Thus only the helium-3 MRE protocol is compatible with *in vivo* applications for which subjects can achieve apneas only over limited times – usually shorter than 10 s.

### **4.3. Secondary assumption for helium-3 MRE: Insensitivity to gas content**

#### **4.3.1. Introduction**

We can circumvent the SNR limitations of MRE in the airways by implementing this technique with hyperpolarized helium-3 as a tracer gas [139]. Yet, the gas contained in the lung presents specific elastic properties which, even at a given pressure, may affect MRE measurements. Therefore its effect must be considered.

Previous experiments on wave propagation in dog lungs suggested that the elastic moduli of the lungs are essentially a function of pressure and that gas inertia does not affect the viscoelastic properties of the lung parenchyma [140]. However, in this work, only longitudinal waves were probed and only bulk elastic moduli were extracted. MRE is able to regionally record both shear and longitudinal waves throughout the lung. Here we performed MRE measurements in preserved pig lungs inflated to the same volume with three different gases of widely varying density: air, helium-4 (<sup>4</sup>He), and sulfur hexafluoride (SF<sub>6</sub>). The set up was designed to make voxel-by-voxel comparison possible.

#### **4.3.2. Materials and methods**

In order to compare MRE measurements in the same lung for different inflations with the three gases, air, helium-4, and sulfur hexafluoride, a lung container was constructed to ensure inflation could be performed to a reproducible volume and shape. The three gases were chosen because of their different density and mechanical properties in order to probe possible modification of the mechanical properties of the lung as measured with MRE. Helium-4 and

helium-3 present similar density and mechanical properties, so for these experiments,  $^4\text{He}$  was used instead of  $^3\text{He}$  for obvious economic reasons.

A BioQuest<sup>®</sup> preserved pig lung (Nasco International, Fort Atkinson, Wisconsin) was inflated with air flowing at  $2 \text{ L}\cdot\text{min}^{-1}$  while immersed in liquid silicon. Then the silicon was allowed to harden overnight. The continuous flow of air was made possible through the lung and the silicon by several small leaks in the lung and two 22 mm output ports embedded in the silicon (Fig.4. 10, c). This resulted in a firm mold containing the lung when deflated, and closing around the lung when inflated. During the MR acquisitions, a constant input gas flow was maintained to overcome the remaining small leaks in the lung (Fig.4. 10, a-b). Larger leaks had been repaired with latex fixture beforehand.

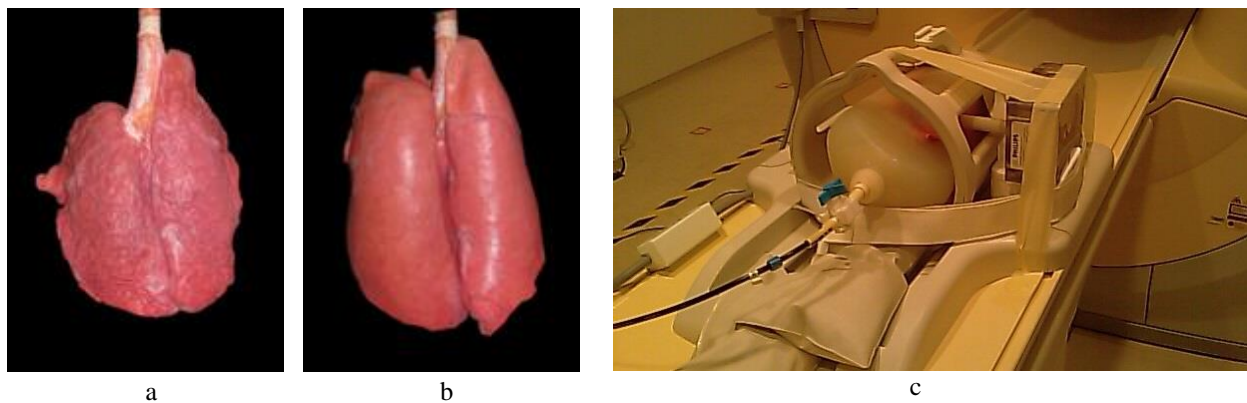


Fig.4. 10: Preserved BioQuest<sup>®</sup> pig lungs (a) fully deflated and (b) fully inflated. (c) Silicon mold containing the lungs. The resulting phantom is positioned in a head coil and solid contact is secured with the piston of an electromechanical vibrator (right). Gas flows through the tracheal port (blue valve) so, despite the remaining small leaks, the lungs remains fully inflated over the MR acquisitions.

MRE measurements were performed with a 1.5 T Achieva scanner (Philips Healthcare, Best, The Netherlands). The lung phantom was placed in an 8-channel SENSE head coil. It was maintained inflated to fully fill up the mold while an MR-compatible vibrator (Philips Healthcare, Best, The Netherlands) induced a mechanical excitation at 85 Hz onto the upper left lobe of the preserved lung. Motion sensitizing gradients,  $21 \text{ mT}\cdot\text{m}^{-1}$ , synchronized with the mechanical wave, were implemented in a spin-echo sequence, over 11 slices, with  $\text{FOV} = (244 \times 194 \times 44) \text{ mm}^3$ ,  $\text{matrix} = 64 \times 64 \times 11$ ,  $TE/TR = 41/59 \text{ ms}$ , and  $T_{\text{ACQ/direction}} = 4 \text{ min } 42 \text{ s}$ , along the three spatial directions  $x$  (phase),  $y$  (measurement), and  $z$  (slice), to acquire eight snap-shots of the propagation wave during the oscillatory cycle. Sets of MRE data were acquired while the lung was inflated with air (twice), helium-4, and sulfur hexafluoride. Shear wavelength ( $\lambda$ ), dynamic and loss shear moduli distribution maps (elasticity,  $G_d$ , and viscosity,  $G_l$ ), were computed for each slice progressing across the lungs

from posterior to anterior. Hydrogen MRI morphology and computed  $\lambda$ ,  $G_d$ , and  $G_l$  maps were compared on a voxel-by-voxel basis by computing the mean differences between corresponding voxels in each image slice. Mean values of  $\lambda$ ,  $G_d$ , and  $G_l$  over the acquired lung volume were also compared.

### **4.3.3. Results and Discussion**

Reconstructed wavelength ( $\lambda$ ), dynamic shear modulus ( $G_d$ ), and loss shear modulus ( $G_l$ ) maps are presented on Fig.4. 11 in the central slice of the preserved pig lung for air,  $^4\text{He}$ , and  $\text{SF}_6$  inflation. Morphology data between air/ $^4\text{He}$ , air/air and air/ $\text{SF}_6$  measurements agree within 12%, 13% and 21% respectively.

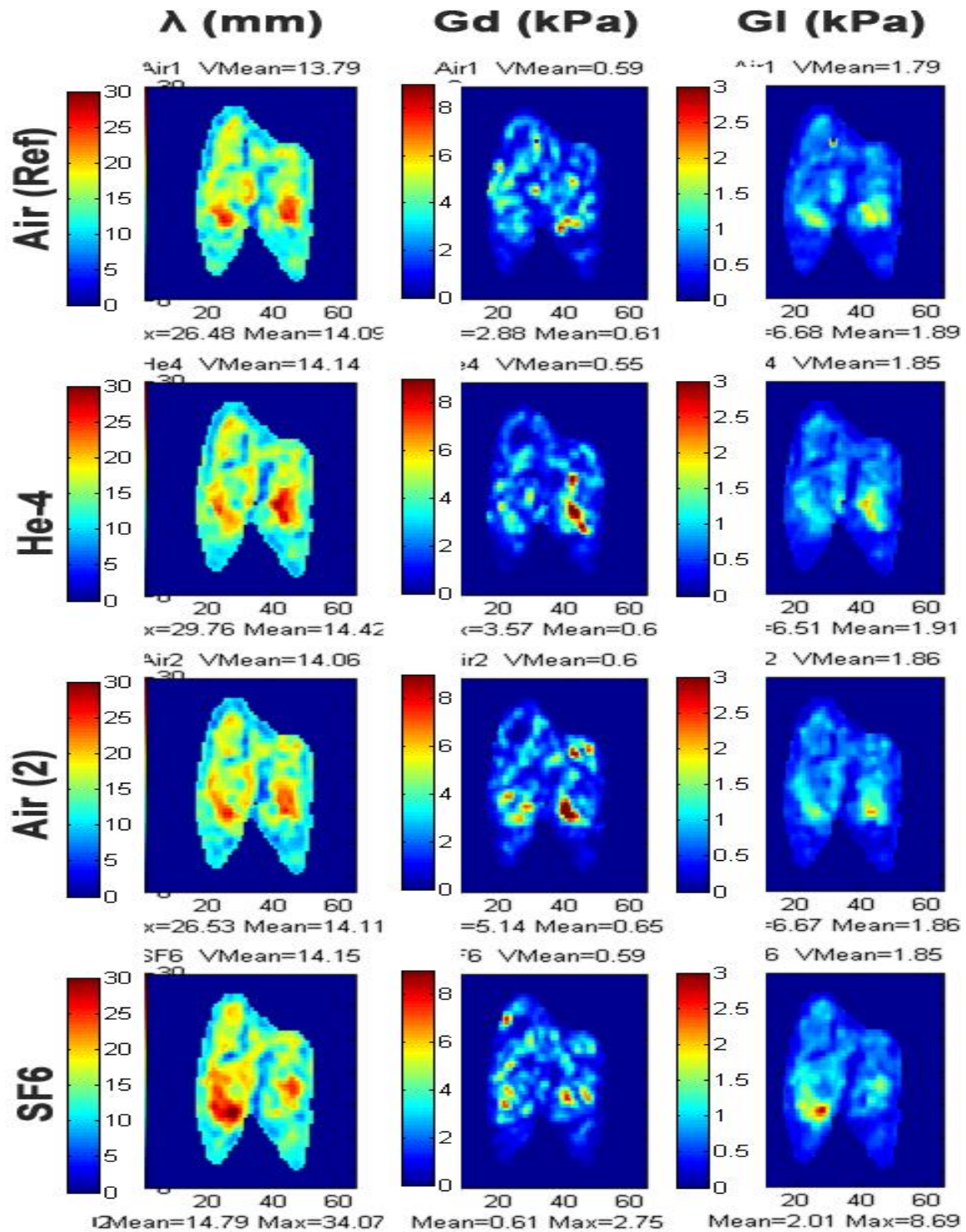


Fig.4. 11: Wavelength ( $\lambda$ ), dynamic shear modulus ( $G_d$ ), and loss shear modulus ( $G_l$ ) maps (left to right) in the preserved pig lungs in the central slice for air,  $^4\text{He}$ , air, and  $\text{SF}_6$  inflation (top to bottom).

Calculated  $\lambda$  values between air/ $^4\text{He}$ , Air/Air and Air/ $\text{SF}_6$  agree to 16%, 15% and 15% respectively. The corresponding  $G_d$  values agree to 26%, 25% and 26%, and the  $G_l$  values to 54%, 52% and 53%. The voxel-by-voxel variations are large and  $G_l$ , being very structured, appears the most sensitive parameter to tissue displacements from one gas inflation to

another. However, these differences can be attributed to regional misregistration since global values of  $\lambda$ ,  $G_d$  and  $G_l$  for the lung phantom inflated with air,  $^4\text{He}$ , and  $\text{SF}_6$  agree very well within  $(14.03 \pm 0.08)$  mm,  $(1.84 \pm 0.02)$  kPa,  $(0.58 \pm 0.02)$  kPa, respectively. These figures clearly corroborate Butler *et al.* [140] earlier findings. For a given inflation volume, namely a given transpulmonary pressure, the viscoelastic properties of the lung parenchyma do not depend on the gas content.

#### 4.4. Conclusion

Lung MRI may be drastically enhanced by the use of hyperpolarized noble gases to achieve fast static and dynamic 3D images of the respiratory system and function under safe conditions even for asthmatic or emphysematous patients [141]–[144]. However, none of the available techniques reveals information on the state of the lung parenchyma tissue itself. Helium-3 MRE opens a new route to probe the mechanical properties of the lungs by non-invasively quantifying its viscoelastic properties. It relies on the primary assumption that the tracer gas is confined within the respiratory system and the secondary assumption that the measured mechanical properties do not depend on the gas composition in the lung. They were challenged in the course of this chapter thanks to the design of two dedicated elastography phantoms based on a BioQuest<sup>®</sup> excised pig lung. The first one preserved the *in vivo* liquid boundary conditions, for any given lung volume, by encapsulating the excised pig lung in a surfactant-filled container and by controlling the admitted amount of surfactant. The second one preserved the volume shape, for a given lung inflation volume, by encapsulating the excised pig lung in a solid silicone mold. Both phantoms were stable over time and ensured controlled and reproducible experimental setups. On the one hand, viscoelastic properties, extracted from the gas displacement fields measured with helium-3 MRE, revealed the underlying mechanical structure of the probed lung and agreed fairly well with those, extracted from the tissue displacement fields with hydrogen MRE. On the other hand, viscoelastic properties remained consistent while being inferred from tissue displacement fields recorded with a different gas in the lung. Hence, the two initial assumptions hold and the helium-3 MRE route is positively validated.

# **Chapter 5.           Sensitivity and quantitation of lung Magnetic Resonance Elastography**

## **5.1. Introduction**

In the former chapter, the viscoelastic properties of a preserved BioQuest® pig lung were quantitatively evaluated and compared both with helium-3 and hydrogen MRE [145]. The fluid/structure coupling was effective such that the two assumptions on gas confinement and gas content in the lung could be validated. The feasibility of helium-3 MRE makes the application of the technique promising as a diagnostic tool for pulmonary diseases.

The main questions we address now is the sensitivity of MRE to any lung disease, namely to any alteration of the organ viscoelastic properties associated to a particular illness. In healthy lungs, the viscoelastic shear moduli are already influenced by several factors. The lung compliance depends on the subject's age, size, weight, and gender [6], [146]. Its distensibility depends on gravity and it reduces with inflation. The prone position was also proven to be more favorable to alveolar recruitment than the supine position [147].

In this chapter, we challenge hydrogen MRE with respect to the degree of lung inflation and to gravity. The goal is twofold: First, evaluation of the sensitivity of lung MRE with controlled changes of the tissue mechanical properties; second, evaluation of the degree of control over the conditions for performing relevant lung MRE to effectively reveal pathological affections.

In the first set of experiments, the preserved pig lung was directly placed in an open cylindrical holder such that the posterior boundary was solid and the anterior boundary, as the lung, even inflated, did not fully fill the surrounding cylinder, was gaseous and let free at

atmospheric pressure. Hydrogen MRE was performed onto the preserved pig lung for three degrees of inflation from deflated lung to normal lung inflation.

In the second set of experiments, we made use of the system model, described in the former chapter, of the preserved pig lung encapsulated in the silicon mold (for a detailed description of the phantom, see Chapter 4, paragraph 4.1.2). The solid boundary of the silicone mold preserved the volume and shape of the inflated lung while the phantom was flipped between prone to supine positions to potentially reverse the distensibility gradient.

In both cases, before every experimental run, we forced a series of successive lung inflations and deflations to remove airway collapses favored by long lung deflation times when the preserved pig lungs were stored between experiments.

## **5.2. Magnetic Resonance Elastography sensitivity to lung inflation**

### **5.2.1. Introduction**

This section focuses on the sensitivity of viscoelastic properties of hydrogen MRE to the degree of lung inflation. It points out correlations between boundary conditions, gravity effects and the distribution maps of the shear wavelength as well as the dynamic and loss shear moduli. The reconstructed mechanical properties are clearly changed throughout the inner regions and the outer periphery of the lungs in relation to the density changes of the structured tissue over lung inflation.

### **5.2.2. Materials and methods**

Experiments were performed on BioQuest® preserved pig lungs in a 1.5 T Achieva scanner (Philips Healthcare, Best, The Netherlands) at CIERM, Bicêtre Hospital, France. The left lung was placed in a cylindrical holder surrounded by a dual Flex-M coil for hydrogen MRE. A MR-compatible transducer (Philips Medical Systems, The Netherlands) [122], induced a mechanical excitation at 85 Hz onto the upper lobe of the left side of the preserved lung (Fig.5.1). Motion sensitizing gradients of  $25.2 \text{ mT}\cdot\text{m}^{-1}$ , synchronized with the mechanical wave, were implemented in a spin-echo sequence for hydrogen MRE, over 12 slices, to acquire eight snap-shots of the propagation wave during the oscillatory cycle along three spatial directions  $x$  (phase),  $y$  (measurement), and  $z$  (slice). The main acquisition parameters were  $\text{FOV} = (159 \times 530 \times 96) \text{ mm}^3$ ,  $\text{matrix} = 68 \times 68 \times 12$ ,  $TE/TR = 17/23 \text{ ms}$ , and

$T_{ACQ}/direction = 27$  s. Sets of MRE data were recorded for three different inflation volumes, 0.8 L, 1 L, and 1.2 L, with a constant nitrogen flow. Shear wavelength ( $\lambda$ ), dynamic and loss shear modulus distribution maps (respectively elasticity,  $G_d$  and viscosity,  $G_l$ ), were estimated in each slice. Slice distributions were extracted from posterior to anterior periphery of the lung.

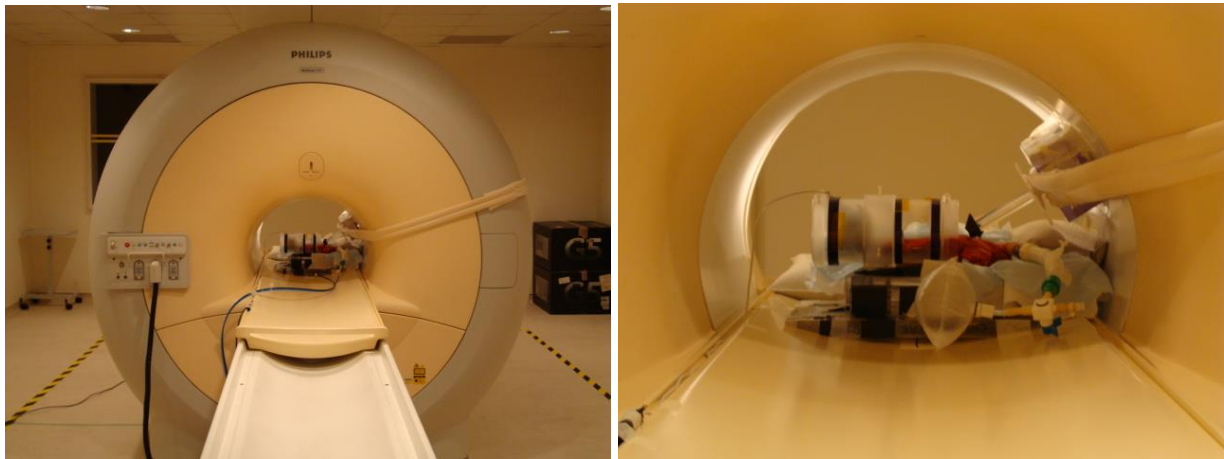


Fig. 5.1 Experimental set up for estimating the MRE sensitivity to lung inflation. The left lung of a BioQuest® preserved pig lung is placed in a dual Flex-M coil for hydrogen MRE (left). A MR-compatible transducer is directly tied to the magnet bore with an extended piston to excite the pig lung (right).

### 5.2.3. Results

**Erreur ! Source du renvoi introuvable.** shows the range of values for the shear wavelength ( $\lambda$ ), dynamic and loss shear moduli ( $G_d$  and  $G_l$ ) at three lung inflation volumes:  $V = \{0.8, 1, 1.2\}$  L.

The variations of the  $\lambda$ ,  $G_d$  and  $G_l$  values are of the 16% , 22% and 6% respectively when the volume increases from 0.8L to 1L and 3.8%, 4.2% and 7% from 1L to 1.2L.

$V = 0.8 \text{ L}$	$V = 1 \text{ L}$	$V = 1.2 \text{ L}$
$5 \text{ mm} < \lambda < 67 \text{ mm}$	$18 \text{ mm} < \lambda < 77 \text{ mm}$	$18 \text{ mm} < \lambda < 80 \text{ mm}$
$5 \text{ kPa} < G_d < 34 \text{ kPa}$	$5 \text{ kPa} < G_d < 41 \text{ kPa}$	$5 \text{ kPa} < G_d < 47 \text{ kPa}$
$0.2 \text{ kPa} < G_l < 29 \text{ kPa}$	$0.2 \text{ kPa} < G_l < 30 \text{ kPa}$	$0.2 \text{ kPa} < G_l < 28 \text{ kPa}$

Tab.5. 2: Range of values for shear wavelength ( $\lambda$ ), dynamic and loss shear moduli ( $G_d$  and  $G_l$ ) at three different inflation volumes: 0.8 L, 1 L, and 1.2 L.

**Erreur ! Source du renvoi introuvable.** 2 (a-c) shows the set of shear wavelength ( $\lambda$ ), dynamic ( $G_d$ ) and loss shear modulus ( $G_l$ ) distributions along the slice progression from posterior (where the lungs were lying) to anterior lung side at 0.8 L (**Erreur ! Source du renvoi introuvable.** 2, a), 1 L (**Erreur ! Source du renvoi introuvable.** 2, b), and 1.2 L (**Erreur ! Source du renvoi introuvable.** 2, c).

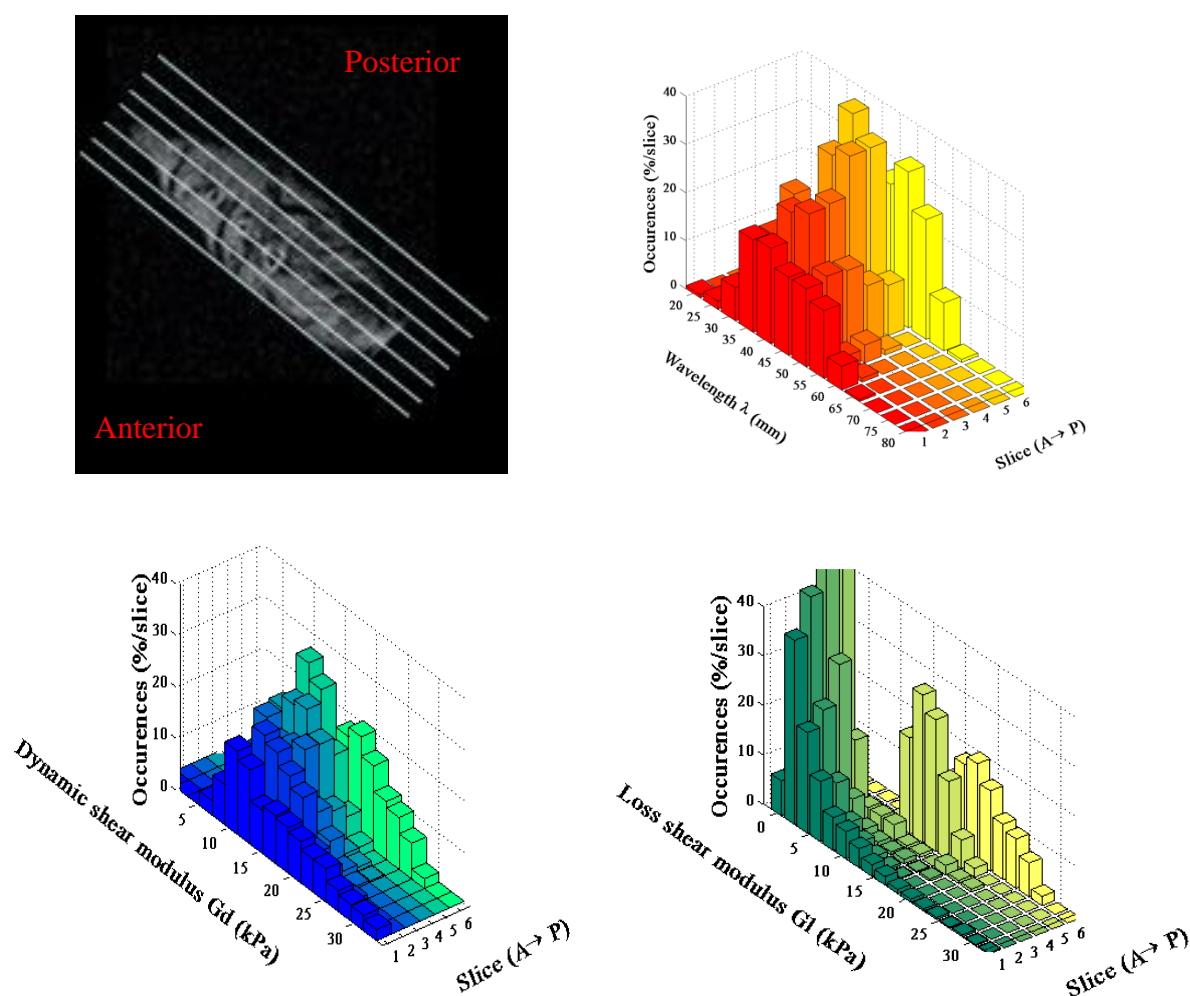


Fig. 5.2-a : Magnitude image of the central axial slice of the preserved Bioquest<sup>®</sup> pig lung inflated to 0.8 L (top

left). Anterior to posterior slice distribution of shear wavelength ( $\lambda$  top right), dynamic ( $G_d$  bottom left) and loss ( $G_l$  bottom right) shear moduli at 0.8 L inflation volume.

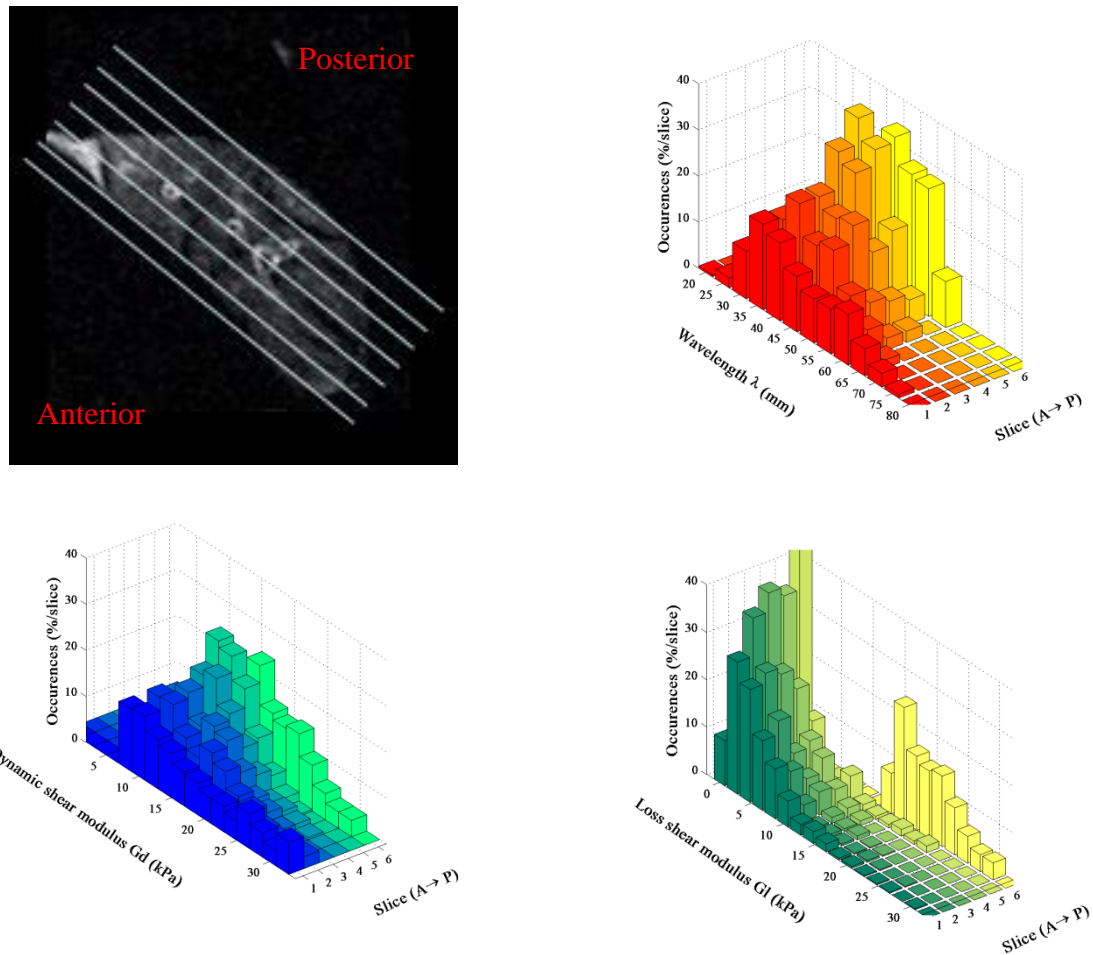


Fig. 5.2-b : Magnitude image of the central axial slice of the preserved Bioquest<sup>®</sup> pig lung inflated to 1.0 L (top left). Anterior to posterior slice distribution of shear wavelength ( $\lambda$  top right), dynamic ( $G_d$  bottom left) and loss ( $G_l$  bottom right) shear moduli at 1.0 L inflation volume.

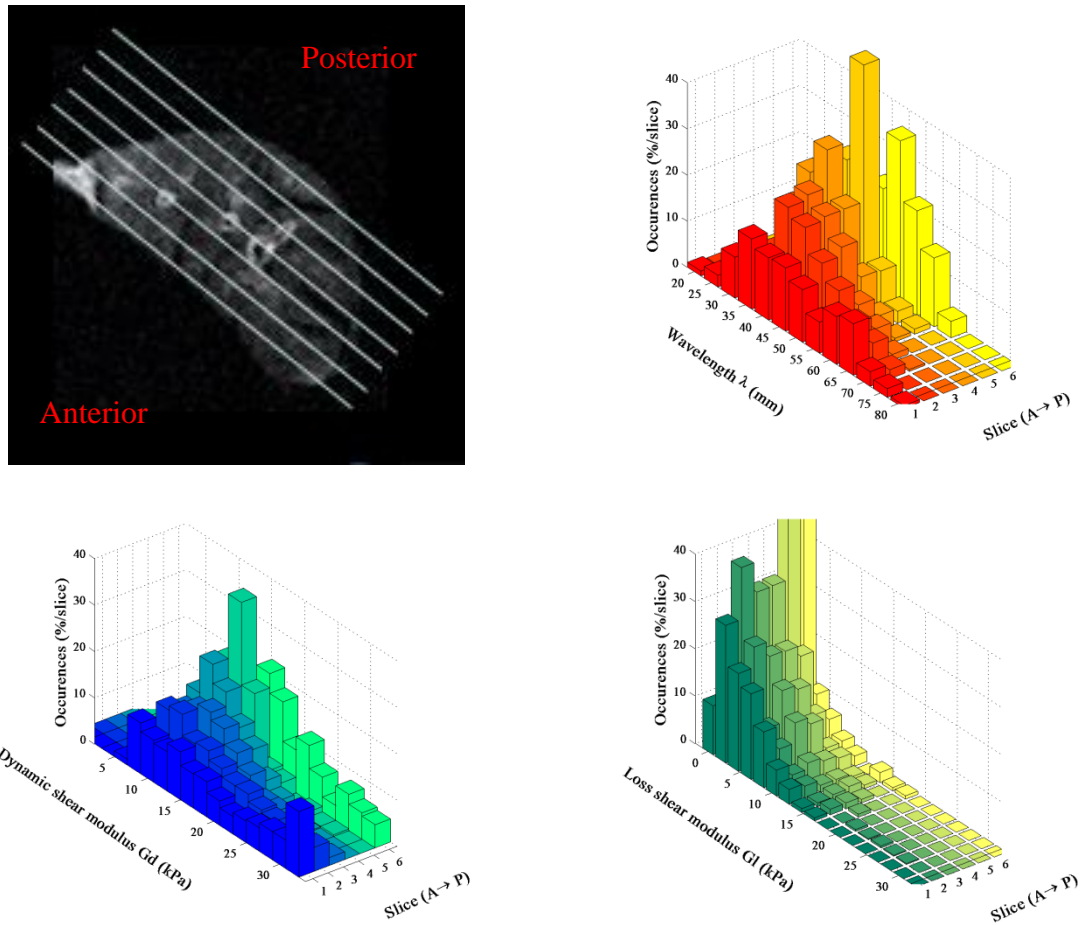


Fig. 5.2-c : Magnitude image of the central axial slice of the preserved Bioquest<sup>®</sup> pig lung inflated to 1.2 L (top left). Anterior to posterior slice distribution of shear wavelength ( $\lambda$  top right), dynamic ( $G_d$  bottom left) and loss ( $G_l$  bottom right) shear moduli at 1.2 L inflation volume.

Volume changes mainly occur at the lung periphery in the anterior lung where alveolar recruitment is underlined by the increase of  $\lambda$  and  $G_d$  and a radical decrease of  $G_l$ .

#### 5.2.4. Discussion

Looking at the morphological images, by a simple qualitative evaluation, over the inflations, (**Erreur ! Source du renvoi introuvable.,c**) in the inner slices, where the main airways are dominant, very little changes are registered. Meanwhile in the outer slices, the volume increases in the upper side of the lung (anterior periphery) more than in the lower side (posterior periphery) because structured tissue is subjected to the gravity and boundary effects. Shear wavelength, dynamic and loss shear modulus distribution maps (**Erreur ! Source du renvoi introuvable.-a,b,c**) corroborate this observation. The inner slices of the lung maintain similar values for the three inflation degrees because the larger airways, which

govern the mechanical behavior of these regions, are barely affected by the lung inflation.  $\lambda$  and  $G_d$  essentially increase with the inflation in the outer slices especially in the anterior lung where volume changes are important.  $G_l$  radically decreases with the inflation volume at the periphery of the anterior lung whereas it remains in the same range of values in the central and posterior parts of the lung. These behaviors could be related to alveolar recruitment.  $\lambda$  and  $G_d$  undergo important increases, 16% and 22% respectively, when the lung is inflated from 0.8 L to 1 L while they undergo little changes when the lung is inflated from 1 L to 1.2 L. When the lung reaches 1 L, most of the proximal airways, including the large airways, bronchioles and alveoli, are already enlisted. When the lung reaches 1.2 L, only the distal airways, namely the remote alveolar spaces, are finally enlisted. Hence, when the lung volume goes from 1 L to 1.2 L,  $\lambda$  and  $G_d$  increase only in the outer anterior and posterior slices of the lung (**Erreur ! Source du renvoi introuvable.-c**). Similarly, the striking decrease of  $G_l$  in the anterior part is related to the regional lessening of the lung density and increase of  $G_d$ . The dynamic and loss shear moduli,  $G_d$  and  $G_l$ , are clearly very sensitive biomarkers of the degree of inflation of the lung. They might be used to map the distribution of alveolar recruitment in lung pathophysiology.  $G_d$  increases while  $G_l$  decreases when airways are recruited.

### 5.3. Magnetic Resonance Elastography sensitivity to gravity

#### 5.3.1. Introduction

Here, we probe the effects of gravity and position on the viscoelastic properties with hydrogen MRE in a preserved Bioquest<sup>®</sup> pig lung in supine and prone positions with a controlled volume and given solid boundaries. CT scans of the preserved pig lung in the same states (position and degree of inflation) were acquired to independently characterize the lung volumes in the two prone and supine positions.

#### 5.3.2. Materials and methods

A BioQuest<sup>®</sup> preserved pig lung was inflated with air flowing at  $2.4 \text{ L}\cdot\text{min}^{-1}$  to fill an enclosing silicon mold in order to ensure lung volume and shape reproducibility and to allow MRE comparison for both prone and supine positions [148] (Fig.5. -a) (for a detailed description of the phantom, see Chapter 4, paragraph 4.1.2). The lung phantom was placed in an 8-channel SENSE head coil in a 1.5 T Achieva scanner. An MR-compatible

electromechanical vibrator (Philips Healthcare, Best, The Netherlands) induced a mechanical excitation at 85 Hz onto the upper left lobe of the preserved lung (Fig.5. -b). Motion sensitizing gradients of  $25.2 \text{ mT}\cdot\text{m}^{-1}$ , synchronized with the mechanical wave, were implemented in a spin-echo sequence, over 36 and 41 slices for the supine and prone positions respectively. Extra slices and a subsequent larger field of view were required in the prone position to image the whole phantom as the silicon mold was not symmetrical around its main axis. Eight snap-shots of the displacement field were acquired during the oscillatory cycle along the right-left (phase), feet-head (measurement), and anterior-posterior (slice) directions.  $\text{FOV} = (244 \times 144 \times 176) \text{ mm}^3$ ,  $\text{matrix} = 64 \times 64 \times 36/41$ ,  $TE/TR = 53/70 \text{ ms}$ , and  $T_{\text{Acq/direction}} = 15 \text{ min}$ . Shear wavelength ( $\lambda$ ), dynamic and loss shear moduli (respectively elasticity,  $G_d$ , and viscosity,  $G_l$ ), were computed using a 3D inversion method described in section 3.2.3.2 of Chapter 3 [149]. Every parametric maps ( $\lambda$ ,  $G_d$ , and  $G_l$ ) were then co-registered with SPM software using Matlab<sup>®</sup> on the basis of the magnitude images with the supine position as a reference. Histograms of  $\lambda$ ,  $G_d$ , and  $G_l$  were eventually inferred for co-registered prone and supine data sets to illustrate their distribution in each slice progressing from the posterior to anterior periphery of the lung. Mean values and standard deviations were processed for each slice.

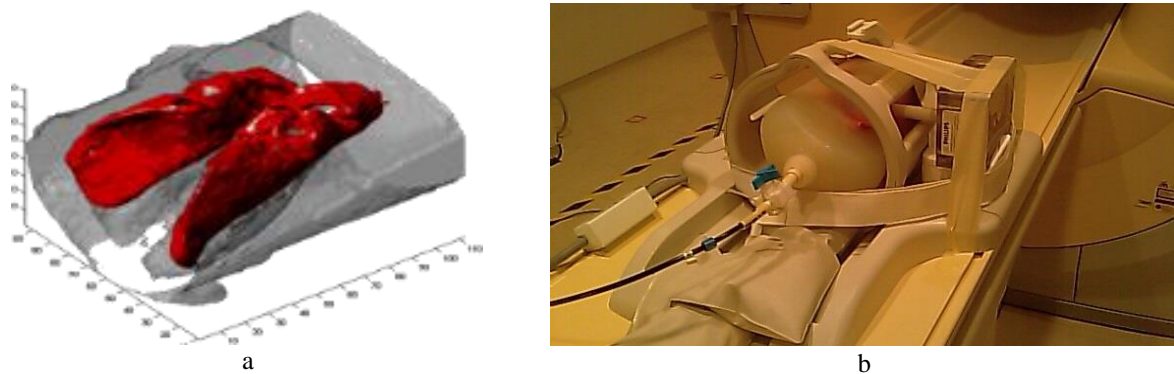


Fig.5. 3: (a) Volume rendering of the BioQuest<sup>®</sup> preserved pig lung in the supine position in the encapsulating silicon mold. (b) Experimental setup on the bed of the MRI scanner: The phantom is placed in an 8-channel head coil with an electromechanical vibrator attached to it.

### 5.3.3. Results

Fig. 5. 4 shows the axial views of the anatomical images acquired by X-ray computed tomodensitometry of the encapsulated pig lung phantom in supine (Fig. 5. 4a) and prone (Fig. 5. 4b) positions.

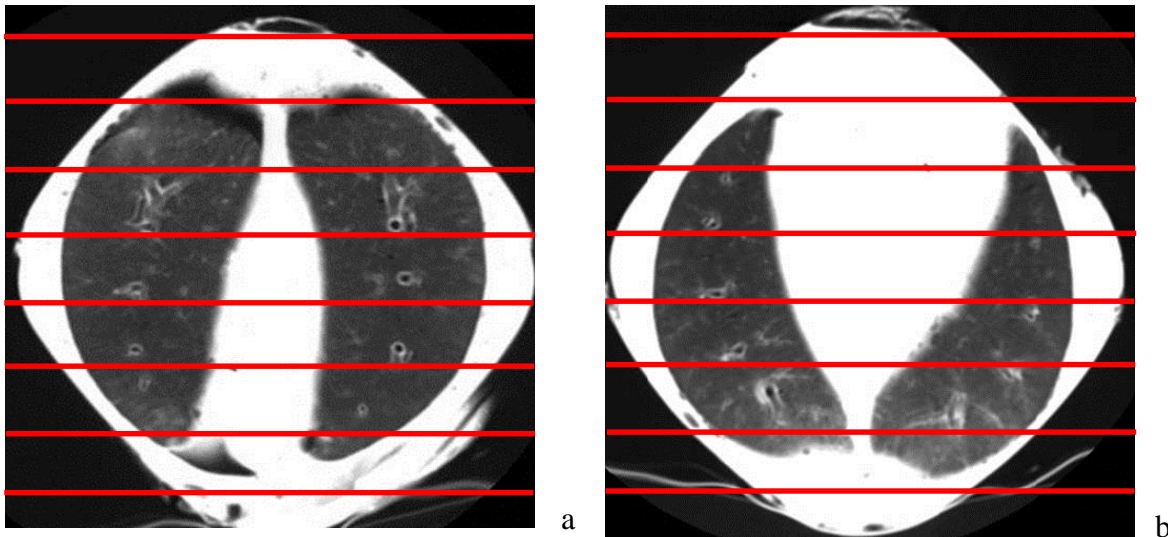


Fig. 5. 4: Morphology images of the lung (axial views) acquired with X-ray computed tomodensitometry in supine (a) and prone (b) positions.

The extracted volumes differed for both positions by 1.08%.

**Erreur ! Source du renvoi introuvable.** (a-b), Fig. 5. 6 (a-b), and Fig. 5. 7 (a-b) show the histograms of  $\lambda$ ,  $G_d$ , and  $G_l$  across the coronal slices for the lung in supine and prone positions. Fig. 5. 5c, Fig. 5. 6c, and Fig. 5. 7c give the corresponding mean values and standard deviations for both positions.

b

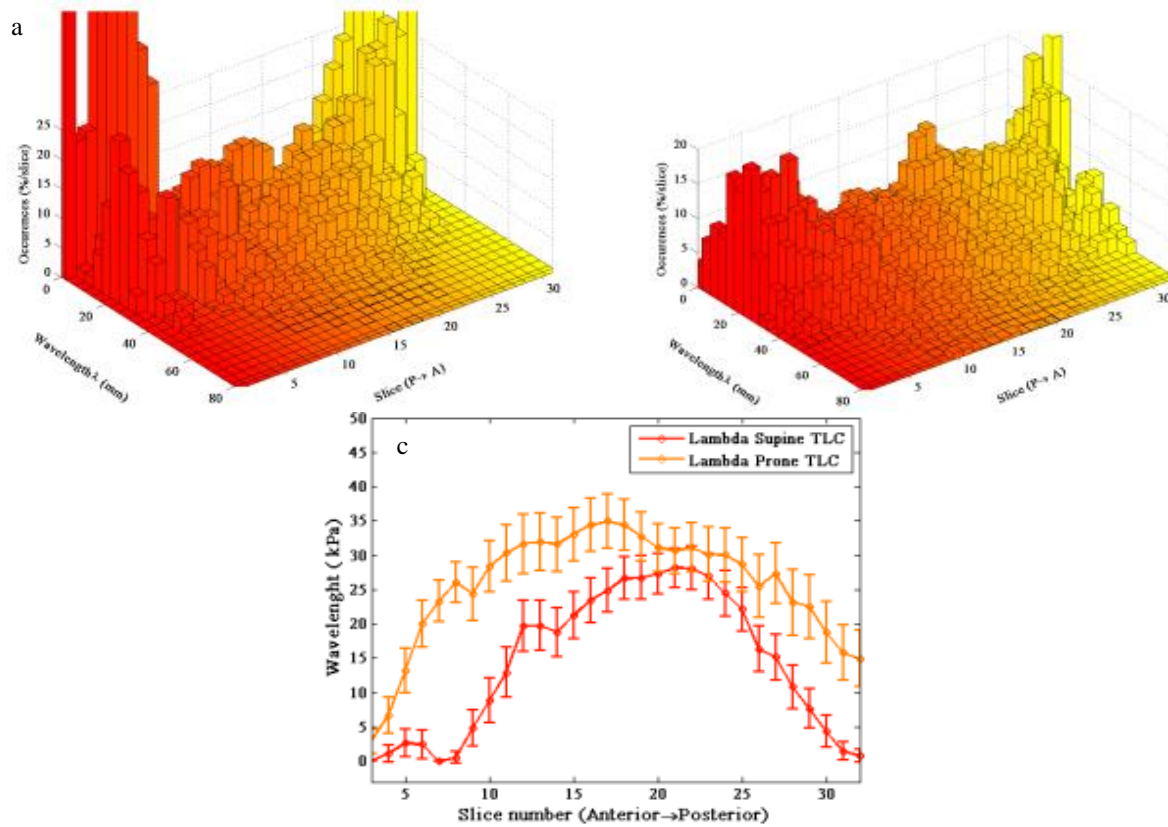


Fig. 5: Shear wavelength ( $\lambda$ ) distribution in a preserved Bioquest<sup>®</sup> pig lung in supine and prone position. Histograms in (a) supine and (b) prone positions across 32 coronal slices. (c) Mean and a fourth of the standard deviation of  $\lambda$  for both positions across the 32 slices.

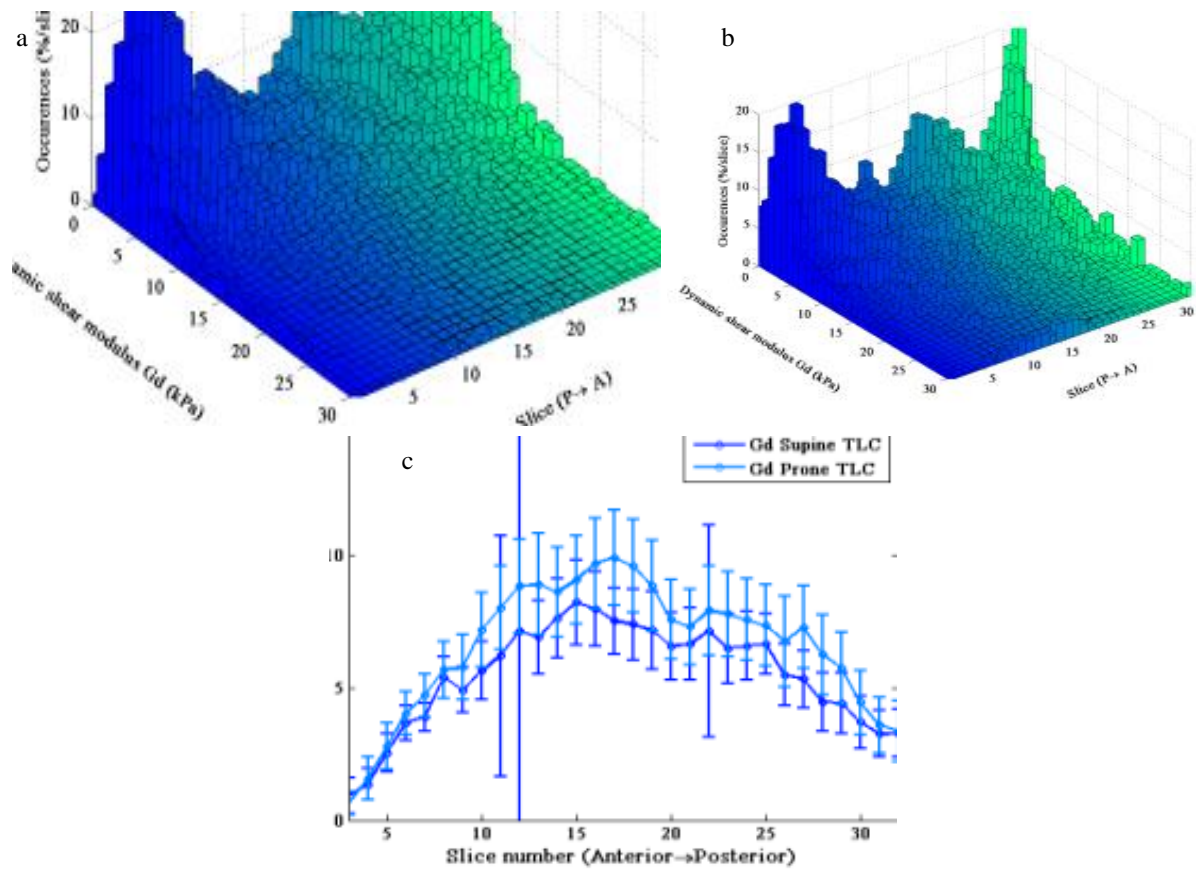


Fig. 5: Dynamic shear modulus ( $G_d$ ) distribution in a preserved Bioquest<sup>®</sup> pig lung in supine and prone position. Histograms in (a) supine and (b) prone positions across 32 coronal slices. (c) Mean and a fourth of the standard deviation of  $G_d$  for both positions across the 32 slices.

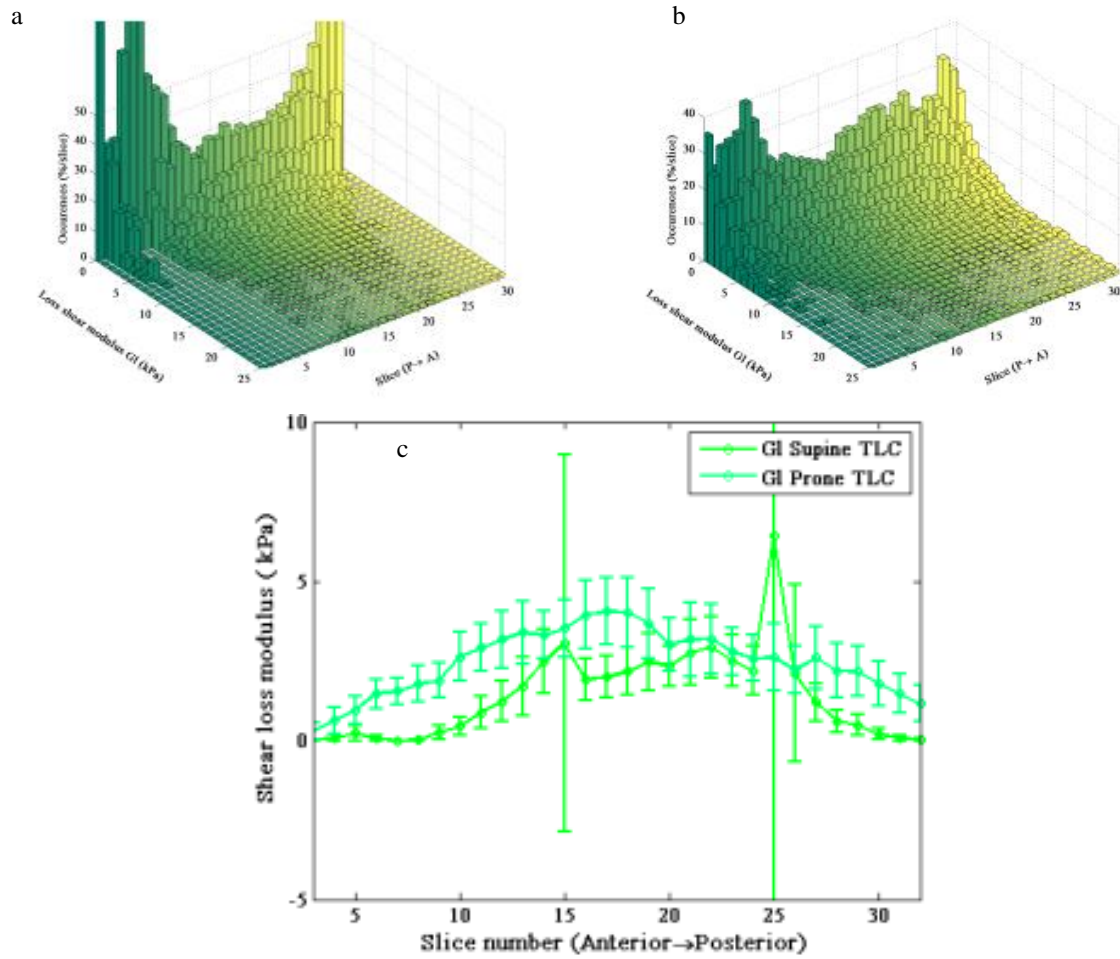


Fig. 5: Loss shear modulus ( $G_l$ ) distribution in a preserved Bioquest<sup>®</sup> pig lung in supine and prone position. Histograms in (a) supine and (b) prone positions across 32 coronal slices. (c) Mean values and a fourth of the standard deviation of  $G_l$  for both positions across the 32 slices.

Mean shear wavelengths increase towards the central slices of the lung from 1 to 25 mm in the supine position and from 5 to 35 mm in the prone position.  $G_d$  and  $G_l$  follow the same trend with mean values reaching, in the supine position, 7 kPa and 2.5 kPa, respectively, and, in the prone position, 10 kPa and 2 kPa, respectively. Mean  $\lambda$ ,  $G_d$ , and  $G_l$  are always higher in the prone than in the supine position. The difference is minimal at the periphery of the lung and maximal in the center.

#### 5.3.4. Discussion

The BioQuest<sup>®</sup> preserved pig lungs encapsulated in the silicone mold ensured reproducible inflation volumes and shapes, for prone and supine positions indifferently, within a percent according to the X-ray tomodensitometry measurements.

The distribution of  $G_d$  and  $G_l$  over the lung in both supine and prone positions with higher values in the central slices match the spatial distribution of the larger and stiffer structures of the bronchial tree in the center of the lung. In the supine position, the posterior part of the lung, larger and more distensible, is compressed due to gravity by the mass of the overlying organ. In prone position, the anterior part, smaller, is less compressed in spite of the same gravity because the lung morphological shape limits the effective compression. Therefore, alveolar recruitment is made easier and is expected to be higher when the lung is in prone position. It is nicely probed with the viscoelastic properties since alveolar recruitment corresponds to distended tissue, namely, in a first approach, to increased  $G_d$  as recorded in the histograms of Fig. 5.5 (a-b), Fig. 5.6 (a-b), and **Erreur ! Source du renvoi introuvable.** (a-b). It is clearly depicted by the mean value increase between supine and prone position for nearly every slices in Fig. 5. 5c, Fig. 5. 6c and Fig.5. 7c. Viscoelastic properties of peripheral slices do not change between prone and supine position as they may be governed by the boundary conditions given by the surrounding silicon mold, which are the same for both positions. These results corroborate the findings of Cakar *et al.* [150]: oxygenation and alveolar recruitment are more efficient when the lung operates in natural position, namely, in prone position for dogs in the Cakar *et al.* work, and, in pigs here.

#### 5.4. Conclusion

In Lai-Fook *et al.* [6], mean shear moduli were measured by indentation test *ex vivo* in human lungs of different ages. Measurements were performed for different inflation volumes defined by the input pressure set between 4 and 25 cmH<sub>2</sub>O. The recorded values increased with the input pressure and ranged between 0.2 or 0.3 kPa (according to the age) to 1.6 kPa. The first set of experiments introduced in this Chapter corroborates the global findings provided by the indentation test: The inflation of the lung volume resulted here in an increase of the regional dynamic shear modulus, mapped by hydrogen MRE. Even though it is not surprising to find different shear moduli on preserved pig lungs and excised human lungs, the values here differ with those measured by Lai-Fook *et al.* mostly because the complex shear modulus was not corrected by the effective regional density of the lung. However, the values obtained in the second set of experiments, where density correction could be applied, fall very close into the range 0.2 kPa-1.6 kPa found by Lai-Fook *et al.* when considering the peripheral values in preserved pig lungs (Fig. 5. 5c, Fig. 5. 6c and Fig.5. 7c) with respect to the outcomes of indentation tests carried at the surface of the excised human lung [6].

In the second set of experiments, the sensitivity of MR elastography to the subject's position was challenged. The alveolar recruitment is expected to be eased in the natural position, which is prone for pigs as it is for dogs [150]. Both dynamic and loss shear moduli are higher over the whole lung when the latter is in the natural prone position. MR elastography clearly discriminates between the two lung states. The greater shear wavelength and dynamic shear modulus accordingly sustain more distended tissues and dilated air spaces. Yet, the greater loss shear modulus is rather puzzling in this second set of experiments as, in the first set of experiments, it decreases with lung inflation, hence, with dilated air spaces. This difference cannot simply be understood by density correction, which is applied in the second set of experiments and not in the first one, as it is the relative change that is considered here. But it might be explained by the different boundary conditions, set free in the air for the first setup and constrained by the solid containing mold for the second setup. Both dynamic and loss shear moduli may consequently be governed at the periphery of the lung by the constraints of the mold.

In conclusion, MR elastography is very sensitive to the state and conditions of the lung. It should be very sensitive to any affections. Thereof, the state and conditions of the lung should be controlled or monitored to reveal the resulting intrinsic pathological effects onto the complex shear modulus.

# **Chapter 6.        *In vivo* helium-3 Magnetic Resonance Elastography of the lung**

## **6.1. Introduction**

As it was shown for hydrogen MRE on two lung system models in the former two chapters, helium-3 MRE is anticipated to be very sensitive to early biomechanical changes that occur in the lung once a disease or a therapy starts affecting the pulmonary tissue.

Unlike hydrogen MRE, helium-3 MRE may be achieved within time durations lower than 10 s, which are compatible with the limiting apneas required *in vivo*. In this last Chapter, helium-3 lung MRE was implemented *in vivo* on small animals and humans.

## **6.2. Materials and methods**

### **6.2.1.        *In vivo* hyperpolarized helium-3 MRE acquisitions in rat lungs**

The rat used in the animal experiment was a 120-day old Wistar male with a weight of 413 g. It was anesthetized with 0.85 mL of a Ketamine/Xylazine cocktail administered by intraperitoneal injection: Kétamine 500 (Virbac, France), concentrated to 50%, and Xylazine (Rompun Bayern Animal Health GmbH, Leverkusen, Germany), concentrated to 10%, with a dose of 80 mg/kg for the first injection and of 10 mg/kg for the second injection. Then it was tracheotomized using a 14 G and 70 mm catheter (Vygon SA, Ecouen, France). Subsequently, the animal was put onto a gel-filled pack (ColdHot pack, 3M Nexcare, Loughborough, United-Kingdom), to keep its body temperature warm. It was finally inserted inside a home-made double bracelet Helmholtz coil in supine position (Fig.6. 1-b). Once in

the scanner, a 1.5 T Achieva scanner (Philips Healthcare, Best, The Netherlands), the animal was connected to a monitoring system, Model 1025 Small Animal Monitoring and Gating System (SA Instrument, Inc, Stony Brook, New York, United-States), to check its heartbeat and temperature.

The mechanical excitation needed for MRE was induced into the rat lung by applying a pressure wave generated by a remote loudspeaker and guided to the surface of the animal chest along a tubular altuglas<sup>®</sup> waveguide (Fig.6. 1-a). The length and diameter of the tubular waveguide were chosen according to the targeted 290 Hz frequency of the pressure wave, such that attenuation between the generating means and the organ was minimized. The loudspeaker was driven by a sine wave generated with a 5.2 V-amplitude by a function generator AFG 3021B (Tektronix, Beaverton, Oregon, United-States) and amplified up to 52 V by a bipolar amplifier BOP 50-2M (Kepco, Flushing, New York, United-States). The generated sine wave was synchronized with the MRI acquisition with a set of definite phase offsets (Fig.6. 1-c). The open output port of the pressure waveguide was secured onto the rat chest with a weight in order to maximize the coupling to the animal. Compression and shear waves were thus induced across the thoracic cage throughout the whole lung. In the primary assumption confirmed by the coupled hydrogen and helium-3 experiments (Chapter 4), the gas is confined in the airways of the respiratory system enough that the motion of the tissue, especially driven by the shear wave propagation, impels the gas molecules to an oscillatory motion at the frequency and wavelength of the propagating shear wave.

A dose of 10 mL of hyperpolarized helium-3 was administered with a syringe to the rat to eventually reach the total lung capacity (TLC) of the animal before an apnea was forced for the MR acquisitions. Helium-3 gas was polarized at 69–71% by metastability exchange optical pumping (Physics Department, Mainz University, Mainz, Germany). Once polarized, the gas was shipped to the experimental site in glass cells contained in a special transport box [82] (Fig.6. 1-d) that creates an homogeneous magnetic field inside in order to maintain the hyperpolarization and mechanically protect the cells from external shocks. The cell holds a pressure of 3 bar when the gas is shipped to the experimental site (CIERM, Le Kremlin-Bicêtre, France).

A 3D gradient-echo sequence was implemented over  $FOV = (80 \times 40 \times 30) \text{ mm}^3$ , with a flip angle  $\alpha = 2,43^\circ$ , 30 slices with 1.25 mm thickness matrix =  $64 \times 32 \times 24$ ,  $TE/TR = 5.2/10 \text{ ms}$ , and eight snap-shots were acquired per oscillatory cycle of the propagating wave. The total acquisition time for each motion encoding spatial direction was reduced to

17 s by a partial k-space acquisition along the two phase encoding directions with  $HS = 60\%$ . The echo time,  $TE$ , was also slightly reduced by the implementation of a partial echo with  $PE = 60\%$ . The overall acceleration factor was close to 3. Such extreme partial acquisition approach could safely be applied as the encoded signal phase was not expected to wrap and, according to former validation tests run on a cylindrical PVA phantom (Chapter 4), the resulting phase artifacts could be neglected.

### 6.2.2. *In vivo* hyperpolarized helium-3 MRE acquisitions in healthy human lungs

*In vivo* experiments were conducted on a healthy volunteer, supine in a prototype helium-3 thorax coil (Rapid Biomedical, Würzburg, Germany) (Fig.6. 1-f) placed in the bore of the 1.5 T Achieva scanner (Fig.6. 1-e). A home-built MR-compatible transducer [152], positioned onto the left side of the chest, induced a mechanical excitation at a frequency of 100 Hz into the lungs (Fig.6. 1-g). A 600 mL dose of helium-3 gas were transferred from the glass cell (Fig.6. 1-d) into a Tedlar<sup>®</sup> bag (SKC, Eighty Four, PA, USA) (Fig.6. 1-h) before being inhaled and supplemented by air so that the subject reached total lung capacity. The subject remained in apnea during the 12 s MRI acquisition. A gradient echo sequence was applied over five 12 mm thick slices, with  $FOV = (350 \times 350 \times 60) \text{ mm}^3$ ,  $matrix = 29 \times 32 \times 5$ , and  $TE/TR = 15/100 \text{ ms}$ . The  $10 \text{ mT} \cdot \text{m}^{-1}$  motion sensitizing gradients, synchronized with the mechanical wave through a trigger pulse, were set along the three spatial directions,  $x$  (phase encoding),  $y$  (reading) and  $z$  (slice) at different time offsets with respect to the excitation. As a result, four snapshots of the propagating wave during one oscillatory cycle were acquired. A fourth acquisition without motion sensitizing gradients was performed to obtain a reference data set. For each spatial acquisition and for the reference one, it was administrated the same dose of gas each time, with a total of 2.4 L of helium-3.

### 6.2.3. MRE data reconstruction

Raw MRE complex data were masked and processed by a dedicated software [111], [122], [153] to reconstruct the 3D displacement fields and to extract the related tissue mechanical properties: 3D maps of the shear wavelength,  $\lambda$ , and of the dynamic and loss shear moduli,  $G_d$ , and  $G_l$ . Mean values and standard deviations of the shear wavelength and the shear viscoelastic moduli were then calculated over the mask.

Density-weighting was applied by multiplying the shear moduli by mean density values:  $0.4 \text{ g}\cdot\text{mL}^{-1}$  for rats and  $0.12 \text{ g}\cdot\text{mL}^{-1}$  for humans. Both values were determined for TLC conditions from typical radiodensity of rat lung parenchyma, measured by computed tomodensitometry (CT) to be  $-600 \text{ HU}$  (Hounsfield Units) [154], and typical radiodensity of human lung parenchyma, found around  $-880 \text{ HU}$  [155]. The corresponding mean mass densities were found by using the conversion formula from HU to  $\text{g}\cdot\text{mL}^{-1}$  [156]:

$$\text{CT density (g}\cdot\text{mL}^{-1}) = (\text{HU} + 1000)/1000, \quad (6. 1)$$

and by considering that the human lung density ranges from  $0.08$  to  $0.5 \text{ g}\cdot\text{mL}^{-1}$  [157]–[159], and that the rat was 120 days old [154].

For human MRE data, the resulting maps of the three middle slices were averaged. The reference displacement map was compared to the wave displacement in the presence of the motion sensitizing gradient and mechanical excitation.

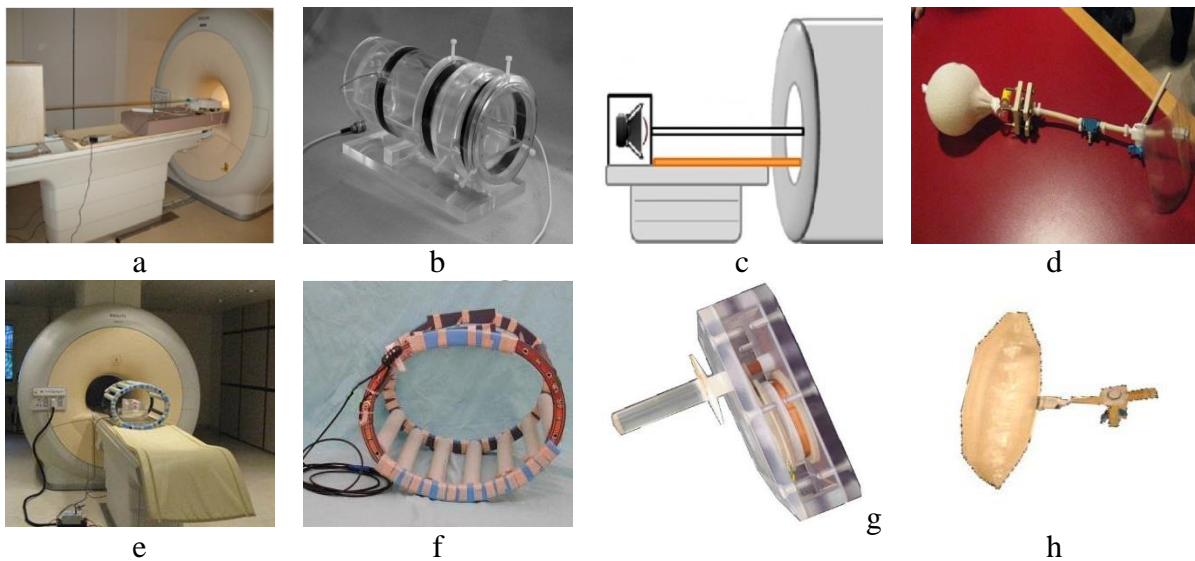


Fig.6. 1 : (a) Set up for small animal helium-3 MRE (b) Helium-3 rat coil (c) Schematic of the remote pressure wave generating means (d) Storage glass cell for hyperpolarized helium-3 (e) Set up for human helium-3 MRE (f) Prototype helium-3 thorax coil (g) Electromechanical vibrator (h) Transport and administration Tedlar® bag

### 6.3. Results

Fig.6. 2 shows the phase maps obtained with helium-3 MRE on the human lungs with the application of the mechanical excitation and the motion sensitizing gradients. They are averaged over the three central slices. It also shows the 3-slice averaged magnitude image (Fig.6. 2-a) and the reference displacement field map acquired without any motion sensitizing

gradient (Fig.6. 2-b), and the displacement field maps  $\{U_P, U_M, U_S\}$  acquired with motion sensitizing gradient along the three spatial directions (Fig.6. 2c-e).

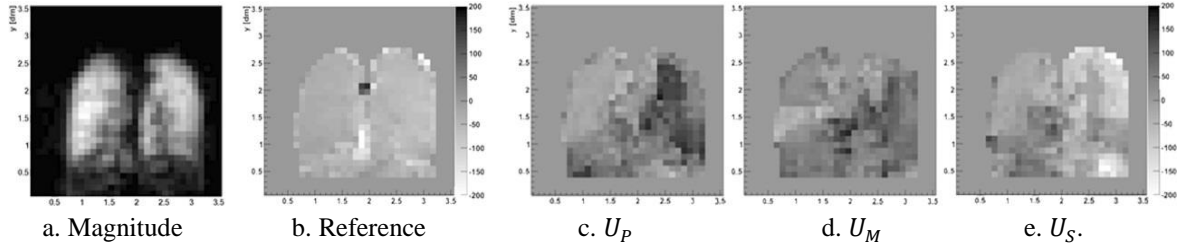


Fig.6. 2: (a) Helium-3 magnitude image averaged over the three central slices (a.u.) and corresponding displacement field maps ( $\mu\text{m}$ ) for a selected time offset (b) without motion sensitizing gradients and with motion sensitizing gradient (c) along  $x$ , the phase encoding direction,  $U_P$ , (d) along  $y$ , the reading direction,  $U_M$ , and (e) along  $z$ , the slice selection,  $U_S$ .

The reference displacement field maps are flat compared to the maps where the motion induced by the propagation of the mechanical wave is encoded. Displacements reached amplitudes of  $118 \mu\text{m}$ ,  $153 \mu\text{m}$ , and  $117 \mu\text{m}$  when motion sensitizing gradients were respectively applied along  $x$ ,  $y$ , and  $z$ . They were limited to  $48 \mu\text{m}$  in the reference image.

Fig.6. 3 shows the magnitude image (Fig.6. 3-a), and the displacement field maps  $\{U_P, U_M, U_S\}$  with motion sensitizing gradient (Fig.6. 3-b-d), averaged over the three central slices, for the rat.

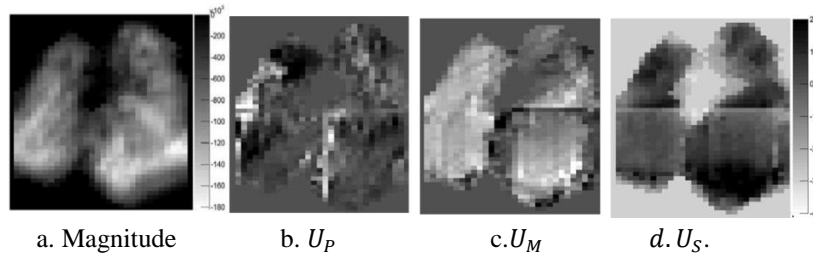


Fig.6. 3 : (a) Rat helium-3 magnitude image (a.u.), and corresponding displacement field maps ( $\mu\text{m}$ ) for a selected time offset with motion sensitizing gradient (b) along  $x$ , the phase encoding direction,  $U_P$ , (c) along  $y$ , the reading direction,  $U_M$ , and (d) along  $z$ , the slice selection,  $U_S$ , over the three central slices.

From displacement field maps, wave propagation and viscoelastic shear modulus maps are calculated for human and rat lungs: Shear wavelength  $\lambda$  (Fig.6. 4-b and Fig.6. 4-f), dynamic shear modulus  $G_d$  (Fig.6. 4-c and Fig.6. 4-g), and loss shear moduli  $G_l$  (Fig.6. 4-d and Fig.6. 4-h).

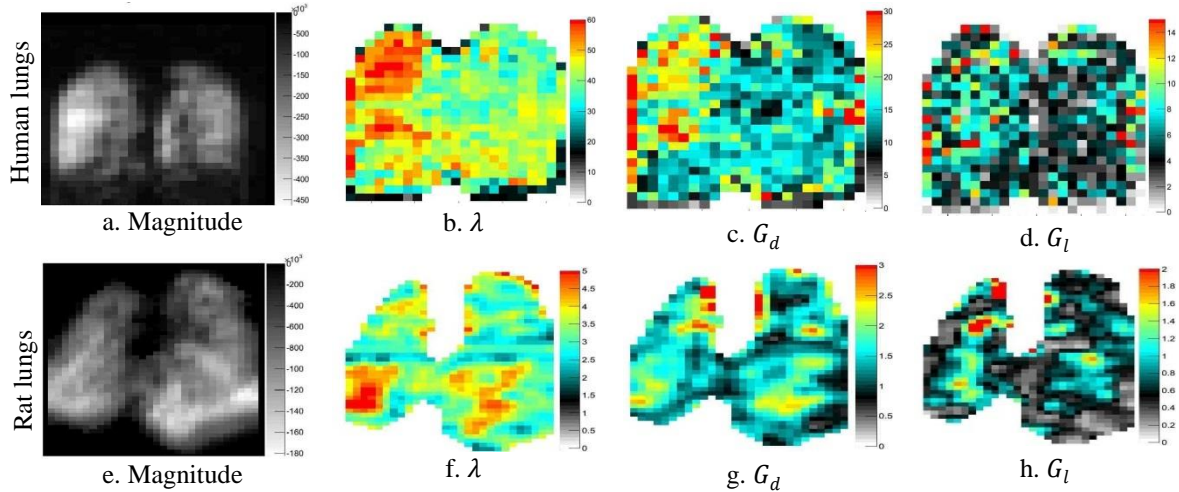


Fig.6. 4: (a) and (e) Magnitude images for human and rat lungs averaged over the three central slices (a.u.). (b) and (f) Wavelength maps (mm) (c-d) and (g-h) Shear elastic and viscosity maps (kPa).

Mean wavelengths of 45 mm and 4 mm were measured in the human and rat lungs, respectively. For elasticity and viscosity, the mean global values before density correction were  $G_d = (1.6 \pm 0.01)$  kPa and  $G_l = (0.45 \pm 0.01)$  kPa, for the rat lungs; and  $G_d = (15.33 \pm 0.21)$  kPa and  $G_l = (2.08 \pm 0.10)$  kPa for the human lungs (Tab.6. 1). The mean global values after density correction were  $G_d = (0.64 \pm 0.01)$  kPa and  $G_l = (0.16 \pm 0.01)$  kPa, for the rat lungs; and  $G_d = (1.83 \pm 0.02)$  kPa and  $G_l = (0.25 \pm 0.01)$  kPa for the human lungs (Tab.6. 1).

	$G_d$ (kPa) without density correction	$G_l$ (kPa) without density correction	Mean density ( $\text{g}\cdot\text{mL}^{-1}$ )	$G_d$ (kPa) with density correction	$G_l$ (kPa) with density correction
Rat lungs	$1.6 \pm 0.01$	$0.45 \pm 0.01$	0.4	$0.64 \pm 0.01$	$0.16 \pm 0.01$
Human lungs	$15.33 \pm 0.21$	$2.08 \pm 0.10$	0.12	$1.83 \pm 0.02$	$0.25 \pm 0.01$

Tab.6. 1: Dynamic and loss shear moduli,  $G_d$  and  $G_l$ , for rat and human lungs before and after density correction (mean and standard deviation over the three central slices). The mean densities used for density correction in the rat and human lungs were calculated from typical radiodensities measured in TLC by X-ray CT.

#### 6.4. Discussion

In *in vivo* experiments in rat and human lungs, the mechanical excitation was generated in the pulmonary tissue along two distinct ways. In the human study, compression and shear waves were induced through the thoracic cage in the body by an electromechanical transducer positioned directly onto the subject's chest in the MRI bore. In the small animal study,

compression and shear waves were induced by a pressure wave guided from a remote loudspeaker to the surface of the animal chest. In both cases, the waves have to cross the thoracic cage, chest muscles, and bones – where it is diffracted and attenuated – before propagating within the lungs. The amplitudes of the propagating waves are far from homogenous throughout the lung, with a pronounced maximum at the point source where the piston or the pressure waveguide is applied onto the chest. They are also physiologically limited by the animal or patient's discomfort or pain, which mainly results from the solid contact between the generating means and the subject's body. In further applications, as it has been shown, so far *ex vivo*, on the system model with liquid boundaries in Chapters 4 and 5, guided pressure wave excitation may advantageously be set up for humans as the pressure wave, guided to the subject's buccal cavity, is naturally guided farther down the upper airways to the bronchial tree before homogeneously propagating throughout the lungs. This approach limits the impediments to wave propagation in the human lung.

In these helium-3 MRE experiments, carried out *in vivo* in rat and human lungs, the acquisition times were 17 s and 12 s for isotropic spatial resolutions of 1.25 mm and 12 mm, and for acquisition matrices of  $64 \times 32 \times 24 \times 8$  snapshots and  $29 \times 32 \times 5 \times 4$  snapshots. Apart from the obvious size difference,  $FOV_{\text{Rat}} = (80 \times 40 \times 30) \text{ mm}^3$  and  $FOV_{\text{Hum}} = (350 \times 350 \times 60) \text{ mm}^3$ , the total acquisition time could be reduced for human studies by the same acceleration factor, close to 3, gained with the partial k-space acquisitions, which were successfully implemented for the small animal studies. The saved time could be used for either increasing the FOV third dimension, improving the spatial resolution, or acquiring the three motion encoded directions in a single apnea. Other acceleration techniques like compressed sensing [160], parallel imaging with a helium-3 RF coil array [161] are currently being developed at IR4M to achieve whole lung MRE in a 10 s apnea.

In Fig.6. 2-b, the phase map, obtained with zero motion sensitizing gradients, is rather uniform. It sets the baseline for the displacement fields to a maximum of  $48 \mu\text{m}$ , which is three times smaller than the recorded displacements when a motion sensitizing gradient is applied along one of the three spatial directions (Fig.6. 2c-e). The non-zero uniform baseline cannot be attributed to motion encoding by the imaging gradients but it may result from the residual magnetic stray field of the electromechanical driver fixed between the subject's chest and the structure of the helium-3 thorax coil. A perfect coupling between the chest surface and the vibrator assures optimal wave propagation in the organ. In this experiment, the

vibrator was wedged in the coil and the volunteer's thorax. The coil of the transducer (Chapter 3, paragraph 3.2.3) may have interacted with the thorax coil components. Lately, in experiments where an electropneumatic transducer and guided pressure was used instead (Chapter 3, paragraph 3.2.5), the baseline for the displacement field of the reference map (with no motion sensitizing gradient and turned off transducer) reaches maxima of  $(0.8 \pm 0.1) \mu\text{m}$  and  $(0.5 \pm 0.05) \mu\text{m}$ , in the rat and human lung experiments, respectively.

The quantitation in the lung of processed dynamic and loss shear moduli highly depends on the value of the tissue density used in the reconstruction. Here, a single global mean value, deduced from radiodensity measurements, was used whereas the density of the pulmonary tissue is neither homogenous nor uniform. As we saw earlier in the BioQuest<sup>®</sup> pig lung (in the paragraph 5.2.2), the lung density widely varies from the thick walls of the bronchial tree down to the thin alveolar structures. The single value approximation, made here, works for the overall organ but certainly fails locally. As we did for the system model with liquid boundaries, density maps should be acquired with either MRI or CT according to the subject specific anatomy, registered to the MRE dataset, and processed to produce quantitative density-weighted maps of dynamic and loss shear moduli.

The global mean value of the dynamic shear modulus,  $G_d = (0.64 \pm 0.01) \text{ kPa}$ , obtained for the rat lungs after density correction falls within the 0.4 – 0.8 kPa range reported by Salerno *et al.* on excised rat lungs at TLC [162]. It is below stiffness values, from 1.07 to 1.30 kPa, that were found with hydrogen MRE in rats *post-mortem* for a pressure between 10 and 15 cmH<sub>2</sub>O by McGee *et al.* [5]. In the latter study, the rats were euthanatized and their chest opened such that lung stiffening might have occurred before MRE measurements could be performed. Therefore, reported values stand above the physiological values found here with helium-3 MRE.

The global mean value of the dynamic shear modulus,  $G_d = (1.83 \pm 0.02) \text{ kPa}$ , obtained for the human lungs after density correction is slightly above the 1.6 – 1.75 kPa range found by Lay-Fook *et al.* and Lambert *et al.* on excised human lungs at TLC [6], [163]. It also falls within the range of stiffness values obtained between 1.51 and 2.14 kPa by Mariappan *et al.* with hydrogen MRE in eight volunteers at TLC [159] but the relevance of the latter is questionable with regard to the very low MR signal to noise ratio achievable in the lungs.

The loss shear moduli, extracted here with helium-3 MRE, cannot be neither checked against any previous experimental measures – as there is none – nor theoretically substantiated – as

---

the interpretation of this parameter is still unclear. Different definitions do exist for parameters such as resistance, elastance, or viscance [164]–[166], but they have not been linked to elasticity and viscosity. Elastance and viscance concern the properties of the system and depend on its geometry whereas elasticity and viscosity strictly deal with the local material properties and are independent of its size or shape. So far, elasticity and stiffness were measured by static methods, like indentation tests, through the bulk modulus,  $K$ , and the shear modulus,  $\mu$  [6], [162]. Unfortunately, the estimation or simulation of resistance and viscance does not provide a direct measure of viscosity. In the liver, hydrogen MRE revealed that viscosity increased for inflamed or injured tissue [167], [168]. Viscosity was shown here in Chapter 5 to decrease with lung inflation [169]. It might even be a more sensitive biomarker of alveolar recruitment than elasticity. MRE measurements in controlled varying conditions, as initiated during the course of this PhD work on two system models, should be carried on to clarify the meaning and relevance of this additional parameter that is lung viscosity.

## 6.5. Conclusion

These experiments, carried *in vivo* for the first time here in human and small animal lungs, ascertain the feasibility of helium-3 MRE for mapping the mechanical properties of the organ. Measured maps of dynamic and loss shear moduli were shown to be sensitive regional indicators of the function of the organ. They should be properly weighted by density maps of the organ to improve the localization of diseases, like emphysema and fibrosis, which usually affect the inferior and posterior regions of the lung [22], [170].

Helium-3 MRE certainly presents all the promises of a new non-invasive tool in the diagnosis, gradation, and monitoring of pulmonary diseases, such as fibrosis, emphysema, asthma, and lung cancer [169].

## Conclusions and perspectives

Two systems models were designed to assess the validity and the sensitivity of helium-MRE. Based on a BioQuest<sup>®</sup> preserved pig lung, they allowed to simulate fairly well the complex behavior of the lung while the biomechanical conditions could be controlled and varied.

Two generating means were used here to induce *ex vivo* and *in vivo* mechanical waves in the respiratory system. The first one was based on a piston driven by a close electromechanical transducer and positioned against the subject's chest or directly on the preserved lung. Its point-source specification limits the extension of the propagation of the mechanical waves over the large human lungs. Associated stray fields add some unwanted artifacts in the MRE acquisition. The required contact between the piston and the subject's chest may be uncomfortable or painful for the subject lying in the MRI scanner. The second one was based on an original design, which made use of the subject's natural airways to guide remotely-generated pressure waves from the buccal cavity along the bronchial tree down to the distal airways. Hence, the propagation of the mechanical wave in the pulmonary tissue was promoted everywhere within the respiratory system. It will be preferred for patient comfort. It is more efficient and easily applicable on patients.

Dedicated gradient echo sequences were developed for helium-3 MRE to reduce the total scan time so the acquisition may eventually be achieved within a single breath hold. Acceleration factors close to 3 were achieved by extreme partial k-space acquisitions. Helium-3 NMR signal was also enhanced by partial echo. New hardware and new methods are being developed today at IR4M to further optimize helium-3 MRE acquisition: Compressed sensing, multifrequency MRE, and parallel acquisition with a six-channel RF coil array.

---

The validity of the two underlying assumptions for helium-3 MRE was established in Chapter 4:

1. In the respiratory system, the gas, hence the tracer gas, is effectively confined in the pulmonary tissue
2. The mechanical properties, namely the dynamic and loss shear moduli, of the respiratory system are not affected by the composition of the gas within.

Thereof, the measurement of the displacement fields of administered hyperpolarized helium-3 gas by helium-3 MRE in the respiratory system provides reliable biomechanical markers of the pulmonary tissue as hydrogen MRE would do through the direct measurement of the displacement fields of the tissue itself.

The sensitivity of hydrogen MRE, hence helium-3 MRE, was challenged in Chapter 5 along known physiological changes of lung compliance:

1. MRE is sensitive to the degree of lung inflation:
  - a. The dynamic shear modulus increases with the lung volume
  - b. The loss shear modulus decreases with the lung volume
2. MRE is sensitive to the distensibility gradient, otherwise the position-dependent gravity effects:
  - a. The dynamic shear modulus increases in gravity and position-eased lung regions
  - b. The loss shear modulus increases in gravity and position-eased lung regions

Therefore, like hydrogen MRE, helium-3 MRE is anticipated to be very sensitive to early biomechanical changes – expectantly overriding physiological changes studied here – that occur in the lung once a disease or a therapy starts affecting the pulmonary tissue.

The feasibility of helium-3 MRE was demonstrated *in vivo* in Chapter 6:

1. In rat lungs
  - a. Mechanical waves were generated by guided pressure waves applied at the surface of the body on the animal chest;
  - b. Displacement fields were recorded throughout the lungs at 290 Hz;
  - c. Reconstructed 3D maps of dynamic and loss shear moduli substantiated the biomechanical structure of the anatomy of the respiratory system;
  - d. Whole lung mean dynamic shear modulus corroborates previous findings obtained by indentation tests on excised lungs;

## 2. In human lungs

- a. Mechanical waves were generated by an electromechanical transducer directly applied at the surface of the subject's body on the chest;
- b. Displacement fields were recorded in the 5 acquired central slices in the lungs at 100 Hz;
- c. Reconstructed maps of dynamic and loss shear moduli roughly differentiated biomechanical structures in the respiratory system;
- d. The dynamic shear modulus averaged over the three central slices of the lung corroborates previous findings obtained by indentation tests on excised lungs.

The segmentation of the imaged lung was shown to be important first to remove regions with low helium-3 signal to noise ratio that would hinder the reconstruction process – like the large airways in the BioQuest<sup>®</sup> preserved pig lung experiments – second to highlight the correlations between lung anatomy and mechanical properties. Reciprocally, lung segmentation based on the shear moduli might yield delineation not only of the different pulmonary lobes but most importantly of the diseased regions.

The tissue density was an essential parameter to assess absolute quantitation of the dynamic and, presumably, loss shear moduli. Density maps obtained with ultrashort echo time (UTE) sequences in MRI or from registered radiodensity maps must be sought to enable regional, quantitative helium-3 MRE.

The information the extracted loss shear modulus provides was still unclear even though it appeared clearly relevant when it could be correlated to alveolar recruitment in the study on lung inflation in a preserved pig lung. Further studies should be carried on in controlled conditions to explore the meaning and the relevance of both dynamic and loss shear moduli with respect to physiological changes of the pulmonary tissue.

These rich quantitative biomechanical parameters are worth pursuing their explorations so we could eventually measure them routinely as obvious biomarkers of the pathophysiological state of the lung in the clinic for early diagnoses, gradation, and monitoring. It might not be with helium-MRE as the cost and the availability of the gas impede any large-scale development. However, xenon-MRE might offer an attractive alternative and hydrogen-MRE might be handled differently such that signal would be measured directly out of the lung parenchyma.

A full clinical research protocol was established for the evaluation of helium-3 MRE on healthy subjects and fibrotic patients. The new modality was ascertained through this PhD to a level where it could have been tested on patients. The sudden limitations on the worldwide stocks of helium-3 have postponed the planned clinical application. The continuing regulations on helium-3 supply suggest today to open the way to alternative imaging solutions so the mechanical parameters of the lung could be at hand.

**Table of symbols**

ADC	Apparent Diffusion Coefficient
B	Magnetic field
B <sub>0</sub>	Main static magnetic field
E	Young's modulus
FOV	Field Of View
G <sub>d</sub>	Shear dynamic modulus
G <sub>l</sub>	Shear loss modulus
ħ	Planck constant divided by 2π
k	Boltzmann's constant
K	Compression modulus
$\vec{M}$	Magnetization
M <sub>0</sub>	Equilibrium magnetization
m <sub>0</sub>	Magnetization per unit volume
T <sub>2</sub>	Intrinsic transverse relaxation time
T <sub>2</sub> <sup>*</sup>	Transverse relaxation time in an inhomogeneous static magnetic field
T <sub>E</sub>	Echo time
T <sub>R</sub>	Repetition time
α	Flip angle

---

$\alpha_e$	Initial mechanical phase-offset
$\tau$	Duration of the RF excitation pulse
$\sigma_p$	Poisson's ratio
$\lambda$	Wavelength
$\lambda_L$	Lame's first parameter
$\mu$	Shear modulus
$\sigma$	Strain



## Bibliography

- [1] [www.lung.org/lung-disease/lung-cancer/resources/facts-figures/lung-cancer-fact-sheet.html](http://www.lung.org/lung-disease/lung-cancer/resources/facts-figures/lung-cancer-fact-sheet.html), “American Lung Association.” .
- [2] National Cancer Institute: SEER Cancer Statistics Review, “U.S. National Institutes of Health.” .
- [3] Cancer Facts and Figures, 2012, “American Cancer Society. Cancer Facts and Figures, 2012.” .
- [4] B. C. Goss, K. P. McGee, E. C. Ehman, A. Manduca, and R. L. Ehman, “Magnetic resonance elastography of the lung: technical feasibility,” *Magn Reson Med*, vol. 56, no. 5, pp. 1060–6, 2006.
- [5] K. P. McGee, R. D. Hubmayr, and R. L. Ehman, “MR elastography of the lung with hyperpolarized  $^3\text{He}$ ,” *Magn Reson Med*, vol. 59, no. 1, pp. 14–8, 2008.
- [6] S. J. Lai-Fook and R. E. Hyatt, “Effects of age on elastic moduli of human lungs,” *J Appl Physiol*, vol. 89, no. 1, pp. 163–8, 2000.
- [7] A. Baghani, S. Salcudean, and R. Rohling, “Theoretical limitations of the elastic wave equation inversion for tissue elastography,” *The Journal of the Acoustical Society of America*, vol. 126, p. 1541, 2009.
- [8] Mathieu Sarracanie, “Imagerie quantitative du dépôt d’aérosols dans les voies aériennes par résonance magnétique de l’hélium-3 hyperpolarisé,” Université Paris-Sud 11, 2011.
- [9] “Nasal cavity,” *Wikipedia, the free encyclopedia*. 10-Feb-2013.
- [10] “Morphometry of the Human Lung: Anesthesiology.” [Online]. Available: [http://journals.lww.com/anesthesiology/Fulltext/1965/05000/Morphometry\\_of\\_the\\_Human\\_Lung.23.aspx](http://journals.lww.com/anesthesiology/Fulltext/1965/05000/Morphometry_of_the_Human_Lung.23.aspx). [Accessed: 27-Nov-2012].
- [11] E. R. Weibel, “Morphometry of the human lung,” *Anesthesiology*, vol. 26, no. 3, p. 367, 1965.
- [12] M. A. Grippi, *Physiopathologie pulmonaire: du concept à la pratique clinique*. Arnette Blackwell, 1996.

- 
- [13] E. R. Weibel, B. Sapoval, and M. Filoche, "Design of peripheral airways for efficient gas exchange," *Respiratory Physiology & Neurobiology*, vol. 148, no. 1–2, pp. 3–21, Aug. 2005.
- [14] J. E. Hansen, E. P. Ampaya, G. H. Bryant, and J. J. Navin, "Branching pattern of airways and air spaces of a single human terminal bronchiole," *J Appl Physiol*, vol. 38, no. 6, pp. 983–989, Jun. 1975.
- [15] E. R. Weibel, "What makes a good lung," *Swiss Med Wkly*, vol. 139, no. 27–28, pp. 375–375, 2009.
- [16] C. B. Daniels and S. Orgeig, "Pulmonary Surfactant: The Key to the Evolution of Air Breathing," *Physiology*, vol. 18, no. 4, pp. 151–157, Aug. 2003.
- [17] Marie Makings, "Human cardiac and respiratory systems," *HUMAN CARDIAC AND RESPIRATORY SYSTEMS*. .
- [18] "Global Initiative for Asthma.2010." 2010.
- [19] "Global Initiative for Asthma. 2009." 2009.
- [20] D. J. Slade and M. Kraft, "Airway remodeling from bench to bedside: current perspectives," *Clin. Chest Med.*, vol. 27, no. 1, pp. 71–85, vi, Mar. 2006.
- [21] M. Kraft, R. Djukanovic, S. Wilson, S. T. Holgate, and R. J. Martin, "Alveolar tissue inflammation in asthma," *Am. J. Respir. Crit. Care Med.*, vol. 154, no. 5, pp. 1505–1510, Nov. 1996.
- [22] S. Matsuoka, T. Yamashiro, G. R. Washko, Y. Kurihara, Y. Nakajima, and H. Hatabu, "Quantitative CT Assessment of Chronic Obstructive Pulmonary Disease1," *Radiographics*, vol. 30, no. 1, pp. 55–66, Jan. 2010.
- [23] M. Longmore, I. Wilkinson, E. Davidson, A. Foulkes, and A. Mafi, *Oxford Handbook of Clinical Medicine*. Oxford University Press, 2010.
- [24] G. SNIDER, "The definition of emphysema : report of a National Heart, Lung and Blood Institute. Division of Lung Diseases. Workshop," *Am Rev Respir Dis*, vol. 132, pp. 182–185, 1985.
- [25] S. Ito, E. P. Ingenito, K. K. Brewer, L. D. Black, H. Parameswaran, K. R. Lutchen, and B. Suki, "Mechanics, nonlinearity, and failure strength of lung tissue in a mouse model

---

of emphysema: possible role of collagen remodeling,” *J Appl Physiol*, vol. 98, no. 2, pp. 503–511, Feb. 2005.

[26] D. Stamenovic and D. Yager, “Elastic properties of air- and liquid-filled lung parenchyma,” *J Appl Physiol*, vol. 65, no. 6, pp. 2565–2570, Dec. 1988.

[27] Y. Fung, *Biomechanics: {M}echanical {P}roperties of {L}iving {T}issues*. Springer-Verlag, 1993.

[28] S. Ito, E. P. Ingenito, K. K. Brewer, L. D. Black, H. Parameswaran, K. R. Lutchen, and B. Suki, “Mechanics, nonlinearity, and failure strength of lung tissue in a mouse model of emphysema: possible role of collagen remodeling,” *J Appl Physiol*, vol. 98, no. 2, pp. 503–511, Feb. 2005.

[29] P. D. Sly, R. A. Collins, C. Thamrin, D. J. Turner, and Z. Hantos, “Volume dependence of airway and tissue impedances in mice,” *J Appl Physiol*, vol. 94, no. 4, pp. 1460–1466, Apr. 2003.

[30] K. K. Brewer, H. Sakai, A. M. Alencar, A. Majumdar, S. P. Arold, K. R. Lutchen, E. P. Ingenito, and B. Suki, “Lung and alveolar wall elastic and hysteretic behavior in rats: effects of in vivo elastase treatment,” *J Appl Physiol*, vol. 95, no. 5, pp. 1926–1936, Nov. 2003.

[31] T. E. King, “Clinical Advances in the Diagnosis and Therapy of the Interstitial Lung Diseases,” *Am. J. Respir. Crit. Care Med.*, vol. 172, no. 3, pp. 268–279, Aug. 2005.

[32] D. S. Kim, H. R. Collard, and T. E. King, “Classification and Natural History of the Idiopathic Interstitial Pneumonias,” *Proc Am Thorac Soc*, vol. 3, no. 4, pp. 285–292, Jun. 2006.

[33] S. J. Bourke, “Interstitial lung disease: progress and problems,” *Postgrad Med J*, vol. 82, no. 970, pp. 494–499, Aug. 2006.

[34] B. Ley, H. R. Collard, and T. E. King, “Clinical Course and Prediction of Survival in Idiopathic Pulmonary Fibrosis,” *Am. J. Respir. Crit. Care Med.*, vol. 183, no. 4, pp. 431–440, Feb. 2011.

[35] S. Misumi and D. A. Lynch, “Idiopathic Pulmonary Fibrosis/Usual Interstitial Pneumonia Imaging Diagnosis, Spectrum of Abnormalities, and Temporal Progression,” *Proc Am Thorac Soc*, vol. 3, no. 4, pp. 307–314, Jun. 2006.

- 
- [36] D. W. Visscher and J. L. Myers, "Histologic Spectrum of Idiopathic Interstitial Pneumonias," *Proc Am Thorac Soc*, vol. 3, no. 4, pp. 322–329, Jun. 2006.
- [37] R. H. Sansores, A. Ramirez-Venegas, R. Pérez-Padilla, M. Montaña, C. Ramos, C. Becerril, M. Gaxiola, P. Paré, and M. Selman, "Correlation between pulmonary fibrosis and the lung pressure-volume curve," *Lung*, vol. 174, no. 5, pp. 315–323, Sep. 1996.
- [38] D. S. Faffe, G. H. Silva, P. M. P. Kurtz, E. M. Negri, V. L. Capelozzi, P. R. M. Rocco, and W. A. Zin, "Lung tissue mechanics and extracellular matrix composition in a murine model of silicosis," *J Appl Physiol*, vol. 90, no. 4, pp. 1400–1406, Apr. 2001.
- [39] Emmanuel DURAND, "Mise en oeuvre de l'imagerie par résonance magnétique du noyau d'hélium-3 hyperpolarisé et contribution à la caractérisation tissulaire des voies aériennes pulmonaires," Université parissud-XI, Orsay, 2001.
- [40] P. K. Manden and A. H. Siddiqui, "Pneumorrhachis, pneumomediastinum, pneumopericardium and subcutaneous emphysema as complications of bronchial asthma," *Ann Thorac Med*, vol. 4, no. 3, pp. 143–145, 2009.
- [41] G. Volpicelli, V. Caramello, L. Cardinale, A. Mussa, F. Bar, and M. F. Frascisco, "Bedside ultrasound of the lung for the monitoring of acute decompensated heart failure," *The American Journal of Emergency Medicine*, vol. 26, no. 5, pp. 585–591, Jun. 2008.
- [42] E. A. Kazerooni, "High-Resolution CT of the Lungs," *AJR*, vol. 177, no. 3, pp. 501–519, Sep. 2001.
- [43] Y. Berthezène, P. Croisille, M. Wiart, N. Howarth, C. Houzard, O. Faure, P. Douek, M. Amiel, and D. Revel, "Prospective comparison of MR lung perfusion and lung scintigraphy," *Journal of Magnetic Resonance Imaging*, vol. 9, no. 1, pp. 61–68, 1999.
- [44] R. Thurnheer, H. Engel, W. Weder, U. Stammberger, I. Laube, E. W. Russi, and K. E. Bloch, "Role of Lung Perfusion Scintigraphy in Relation to Chest Computed Tomography and Pulmonary Function in the Evaluation of Candidates for Lung Volume Reduction Surgery," *Am. J. Respir. Crit. Care Med.*, vol. 159, no. 1, pp. 301–310, Jan. 1999.
- [45] P. J. Roach, D. J. Gradinscak, G. P. Schembri, E. A. Bailey, K. P. Willowson, and D. L. Bailey, "SPECT/CT in V/Q Scanning," *Seminars in Nuclear Medicine*, vol. 40, no. 6, pp. 455–466, Nov. 2010.

- 
- [46] M. F. V. Melo, D. Layfield, R. S. Harris, K. O'Neill, G. Musch, T. Richter, T. Winkler, A. J. Fischman, and J. G. Venegas, "Quantification of Regional Ventilation-Perfusion Ratios with PET," *J Nucl Med*, vol. 44, no. 12, pp. 1982–1991, Dec. 2003.
- [47] A. M. Groves, T. Win, N. J. Screatton, M. Berovic, R. Endozo, H. Booth, I. Kayani, L. J. Menezes, J. C. Dickson, and P. J. Ell, "Idiopathic Pulmonary Fibrosis and Diffuse Parenchymal Lung Disease: Implications from Initial Experience with 18F-FDG PET/CT," *J Nucl Med*, vol. 50, no. 4, pp. 538–545, Apr. 2009.
- [48] V. M. Mai and S. S. Berr, "MR perfusion imaging of pulmonary parenchyma using pulsed arterial spin labeling techniques: FAIRER and FAIR," *Journal of Magnetic Resonance Imaging*, vol. 9, no. 3, pp. 483–487, 1999.
- [49] C. J. Galbán, M. K. Han, J. L. Boes, K. A. Chughtai, C. R. Meyer, T. D. Johnson, S. Galbán, A. Rehemtulla, E. A. Kazerooni, F. J. Martinez, and B. D. Ross, "Computed tomography-based biomarker provides unique signature for diagnosis of COPD phenotypes and disease progression," *Nat Med*, vol. 18, no. 11, pp. 1711–1715, Nov. 2012.
- [50] I. I. Rabi, S. Millman, P. Kusch, and J. R. Zacharias, "The Molecular Beam Resonance Method for Measuring Nuclear Magnetic Moments," *Phys. Rev*, vol. 53, no. 495, p. 318, 1938.
- [51] A. G. Filler, "The history, development and impact of computed imaging in neurological diagnosis and neurosurgery: CT, MRI, and DTI," *Internet Journal of Neurosurgery*, vol. 7, no. 1, 2010.
- [52] P. Mansfield and A. . Maudsley, "Planar spin imaging by NMR," *Journal of Magnetic Resonance (1969)*, vol. 27, no. 1, pp. 101–119, Jul. 1977.
- [53] A. Kumar, D. Welti, and R. R. Ernst, "NMR Fourier zeugmatography," *Journal of Magnetic Resonance*, vol. 213, no. 2, pp. 495–509, 2011.
- [54] R. Muthupillai, D. J. Lomas, P. J. Rossman, J. F. Greenleaf, A. Manduca, and R. L. Ehman, "Magnetic Resonance Elastography by Direct Visualization of Propagating Acoustic Strain Waves," *Science*, vol. 269, no. 5232, pp. 1854–1857, Sep. 1995.
- [55] E. J. van Beek and J. M. Wild, "Hyperpolarized 3-helium magnetic resonance imaging to probe lung function," *Proc Am Thorac Soc*, vol. 2, no. 6, pp. 528–32, 510, 2005.
- [56] C. Cohen-Tannoudji, B. Diu, and F. Laloë, "Mécanique quantique," 1986.

- [57] J.M. Perez Sanchez, “La Imagen de Resonancia Magnética de difusión de gases como herramienta de caracterización de la estructura y la función pulmonar,” Universidad complutense, Madrid, 2008.
- [58] J. L. Flowers, B. W. Petley, and M. G. Richards, “A Measurement of the Nuclear Magnetic Moment of the Helium-3 Atom in Terms of that of the Proton,” *Metrologia*, vol. 30, no. 2, pp. 75–87, Jan. 1993.
- [59] F Bloch, “Nuclear induction,” *Physical Review*, vol. 70(7–8), pp. 460–474, 1946.
- [60] M. L. Wood and F. W. Wehrli, “Principles of magnetic resonance imaging,” *Magnetic Resonance Imaging 3rd edn (eds Stark, DD & Bradley, W.)*, pp. 1–14, 1999.
- [61] P. Mansfield, A. A. Maudsley, and T. Bains, “Fast scan proton density imaging by NMR,” *Journal of Physics E: Scientific Instruments*, vol. 9, no. 4, pp. 271–278, Apr. 1976.
- [62] L. de Rochefort, “Imagerie dynamique et vélocimétrie IRM des gaz hyperpolarisés,” Université Paris-Sud 11, 2006.
- [63] H. R. Wexler, R. L. Nicholson, F. S. Prato, L. S. Carey, S. Vinitski, and L. Reese, “Quantitation of lung water by nuclear magnetic resonance imaging. A preliminary study,” *Investigative Radiology*, vol. 20, pp. 583–590, 1985.
- [64] M. S. Albert, G. D. Cates, B. Driehuys, W. Happer, B. Saam, C. S. Springer, and A. Wishnia, “Biological magnetic resonance imaging using laser-polarized  $^{129}\text{Xe}$ ,” *Published online: 21 July 1994; | doi:10.1038/370199a0*, vol. 370, no. 6486, pp. 199–201, Jul. 1994.
- [65] J. R. MacFall, H. C. Charles, R. D. Black, H. Middleton, J. C. Swartz, B. Saam, B. Driehuys, C. Erickson, W. Happer, G. D. Cates, G. A. Johnson, and C. E. Ravin, “Human lung air spaces: potential for MR imaging with hyperpolarized  $\text{He-3}$ ,” *Radiology*, vol. 200, no. 2, pp. 553–558, Aug. 1996.
- [66] L. R. Schad, P. Bachert, M. Bock, M. Essig, M. V. Knopp, M. Ebert, T. Grossmann, W. Heil, R. Surkau, and E. W. Otten, “Hyperpolarized gases—a new type of MR contrast agents?,” *Acta Radiol Suppl*, vol. 412, pp. 43–6, 1997.
- [67] L. Darrasse, G. Guillot, P.-J. Nacher, and G. Tastevin, “Low-field  $^3\text{He}$  nuclear magnetic resonance in human lungs,” *Comptes Rendus de l’Académie des Sciences - Series IIB - Mechanics-Physics-Chemistry-Astronomy*, vol. 324, no. 11, pp. 691–700, Jun. 1997.

- 
- [68] H U Kauczor, “Helium-3 imaging of pulmonary ventilation,” *The British Journal of Radiology*, vol. 71, pp. 701–703, 1998.
- [69] J. R. Mayo and M. E. Hayden, “Hyperpolarized Helium 3 Diffusion Imaging of the Lung1,” *Radiology*, vol. 222, no. 1, pp. 8–11, Jan. 2002.
- [70] G. Peces-Barba, J. Ruiz-Cabello, Y. Cremillieux, I. Rodríguez, D. Dupuich, V. Callot, M. Ortega, M. L. R. Arbo, M. Cortijo, and N. Gonzalez-Mangado, “Helium-3 MRI diffusion coefficient: correlation to morphometry in a model of mild emphysema,” *Eur Respir J*, vol. 22, no. 1, pp. 14–19, Jul. 2003.
- [71] T. G. Walker and W. Happer, “Spin exchange optical pumping of noble gas nuclei,” *Reviews of Modern Physics*, vol. 69, pp. 629–642, 1997.
- [72] F. D. Colegrove, L. D. Schearer, and G. K. Walters, “Polarization of  $\text{He}^{\{3\}}$  Gas by Optical Pumping,” *Phys. Rev.*, vol. 132, no. 6, pp. 2561–2572, Dec. 1963.
- [73] G. K. Walters, F. D. Colegrove, and L. D. Schearer, “Nuclear Polarization of  $\text{He}^{\{3\}}$  Gas by Metastability Exchange with Optically Pumped Metastable  $\text{He}^{\{3\}}$  Atoms,” *Phys. Rev. Lett.*, vol. 8, no. 11, pp. 439–442, Jun. 1962.
- [74] A Vignaud, “Influence de l’intensité du champ magnétique sur l’imagerie RMN des poumons à l’aide d’hélium-3 hyperpolarisé.” Université Paris-Sud 11, 2003.
- [75] J. Dupont-Roc, M. Leduc, and F. Laloë, “Contribution à l’étude du pompage optique par échange de métastabilité dans  $3\text{He}$ . - Première Partie,” *Journal de Physique*, vol. 34, no. 11–12, pp. 961–976, 1973.
- [76] “Optical pumping in  $3\text{He}$  with a laser | J. Phys. France.” .
- [77] T. R. Gentile and R. D. McKeown, “Spin-polarizing  $^{\{3\}}\text{He}$  nuclei with an arc-lamp-pumped neodymium-doped lanthanum magnesium hexaluminate laser,” *Phys. Rev. A*, vol. 47, no. 1, pp. 456–467, Jan. 1993.
- [78] N. P. Bigelow, P. J. Nacher, and M. Leduc, “Accurate optical measurement of nuclear polarization in optically pumped  $^3\text{He}$  gas,” *Journal de Physique II*, vol. 2, no. 12, pp. 2159–2179, Dec. 1992.
- [79] S. V. Chernikov, J. R. Taylor, N. S. Platonov, V. P. Gapontsev, P. J. Nacher, G. Tastevin, M. Leduc, and M. J. Barlow, “1083 nm ytterbium doped fibre amplifier for optical pumping of helium,” *Electronics Letters*, vol. 33, no. 9, pp. 787–789, Apr. 1997.

- [80] E Courtage, “Pompage optique de l’hélium dans des conditions non standard,” Ecole Normale Supérieure, Université Paris-Sud 11, 2001.
- [81] T. R. Gentile, M. E. Hayden, and M. J. Barlow, “Comparison of metastability-exchange optical pumping sources,” *J. Opt. Soc. Am. B*, vol. 20, no. 10, pp. 2068–2074, Oct. 2003.
- [82] S. Hiebel, T. Großmann, D. Kiselev, J. Schmiedeskamp, Y. Gusev, W. Heil, S. Karpuk, J. Krimmer, E. W. Otten, and Z. Salhi, “Magnetized boxes for housing polarized spins in homogeneous fields,” *Journal of Magnetic Resonance*, vol. 204, no. 1, pp. 37–49, May 2010.
- [83] J. Choukeife, X. Maitre, P. J. Nacher, and G. Tastevin, “On-site production of hyperpolarised helium-3 gas for lung MRI,” *Abstracts ISSN*, pp. 1524–6965, 2003.
- [84] P. J. Nacher, G. Tastevin, X. Maître, X. Dollat, B. Lemaire, and J. Olejnik, “A peristaltic compressor for hyperpolarized helium,” *Eur. Radiol*, vol. 9, p. B18, 1999.
- [85] A. J. Deninger, B. Eberle, M. Ebert, T. Großmann, W. Heil, H.-U. Kauczor, L. Lauer, K. Markstaller, E. Otten, J. Schmiedeskamp, W. Schreiber, R. Surkau, M. Thelen, and N. Weiler, “Quantification of Regional Intrapulmonary Oxygen Partial Pressure Evolution during Apnea by  $^3\text{He}$  MRI,” *Journal of Magnetic Resonance*, vol. 141, no. 2, pp. 207–216, Dec. 1999.
- [86] Sarracanie, M., Grebenkov, D., Sandeau, J., Coulibaly. S., Martin, A.R., Hill, K.A., Pérez-Sánchez, J.M., Fodil, R., Martin, L., Durand, E., Caillibotte, G., Isabey, D., Darrasse, L., Bittoun, J., & Maître, X., “Helium-3 MRI of aerosol deposition in human airways,” *Phys. Rev. Lett*, 2011.
- [87] Sarracanie, M., Grebenkov, D., Sandeau, J., Coulibaly. S., Martin, A.R., Hill, K.A., Pérez-Sánchez, J.M., Fodil, R., Martin, L., Durand, E., Caillibotte, G., Isabey, D., Darrasse, L., Bittoun, J., & Maître, X., “Quantification of aerosol deposition in the upper airways: A multimodality study,” presented at the ISMRM, 19th Annual Meeting, Montréal, Québec, Canada., 2011.
- [88] Sarracanie, M., Pérez-Sánchez, J-M., Marsolat, F., Martin, L., Santarelli, R., Hagot, P., Maître, X., & Darrasse, L., “SAGAS (Small Animal Gas Administration System): Gas administration platform for lung imaging of small animals, Nouveaux défis en imagerie du petit animal,” presented at the GDR Imagiv (CNRS), Marseille, France, 2010.

- 
- [89] José M. Pérez-Sánchez, Kyle Hill, Ignacio Rodríguez, Laura Carrero-Gonzalez, Roberta Santarelli, Jelena Pesic, Marion Tardieu, Pascal Hagot, Mathieu Sarracanie, Thomas Kaulisch, Detlef Stiller, Lars E. Olsson, Jesús Ruiz-Cabello, Luc Darrasse and Xavier Maître, “A comparison of  $^3\text{He}$  MRI short-range Apparent Diffusion Coefficient and  $^3\text{He}$   $T_2^*$  as in-vivo microstructural probes of the rat lung periphery at different magnetic field strengths,” *MRM*, 2013.
- [90] Sarracanie Mathieu, “SAGAS (Small Animal Gas Administration System): Gas administration platform for lung imaging of small animals,” *IMAGIV*, 2011.
- [91] L. Zhao, R. Mulkern, C. H. Tseng, D. Williamson, S. Patz, R. Kraft, R. L. Walsworth, F. A. Jolesz, and M. S. Albert, “Gradient-echo imaging considerations for hyperpolarized  $^{129}\text{Xe}$  MR,” *Journal of magnetic resonance. Series B*, vol. 113, no. 2, pp. 179–183, 1996.
- [92] W. Heil, H. Humblot, E. Otten, M. Schafer, R. Sarkau, and M. Leduc, “Very long nuclear relaxation times of spin polarized helium 3 in metal coated cells,” *Physics Letters A*, vol. 201, no. 4, pp. 337–343, May 1995.
- [93] N. R. Newbury, A. S. Barton, G. D. Cates, W. Happer, and H. Middleton, “Gaseous  $^3\text{-}^3\text{He}$  magnetic dipolar spin relaxation,” *Phys. Rev. A*, vol. 48, no. 6, pp. 4411–4420, Dec. 1993.
- [94] B. Saam, W. Happer, and H. Middleton, “Nuclear relaxation of  $^3\text{He}$  in the presence of  $\text{O}_2$ ,” *Phys. Rev. A*, vol. 52, no. 1, pp. 862–865, Jul. 1995.
- [95] M. Bock, “Simultaneous  $T_2^*$  and diffusion measurements with  $^3\text{He}$ ,” *Magnetic Resonance in Medicine*, vol. 38, no. 6, pp. 890–895, 1997.
- [96] M. Salerno, J. R. Brookeman, E. E. de Lange, and J. P. Mugler, “Hyperpolarized  $^3\text{He}$  lung imaging at 0.5 and 1.5 Tesla: A study of susceptibility-induced effects,” *Magnetic Resonance in Medicine*, vol. 53, no. 1, pp. 212–216, 2005.
- [97] X. J. Chen, H. E. Möller, M. S. Chawla, G. P. Cofer, B. Driehuys, L. W. Hedlund, and G. A. Johnson, “Spatially resolved measurements of hyperpolarized gas properties in the lung in vivo. Part I: Diffusion coefficient,” *Magnetic Resonance in Medicine*, vol. 42, no. 4, pp. 721–728, 1999.
- [98] M. H. Deppe, J. Parra-Robles, S. Ajraoui, S. R. Parnell, M. Clemence, R. F. Schulte, and J. M. Wild, “Susceptibility effects in hyperpolarized  $^3\text{He}$  lung MRI at 1.5T and 3T,” *Journal of Magnetic Resonance Imaging*, vol. 30, no. 2, pp. 418–423, 2009.

- 
- [99] M. A. Hajji, T. A. Wilson, and S. J. Lai-Fook, "Improved measurements of shear modulus and pleural membrane tension of the lung," *J Appl Physiol*, vol. 47, no. 1, pp. 175–181, Jul. 1979.
- [100] T. M. Atanackovic and A. Guran, *Theory of elasticity for scientists and engineers*. Birkhauser, 2000.
- [101] J. Ophir, S. K. Alam, B. S. Garra, F. Kallel, E. E. Konofagou, T. KROUSKO, C. R. B. Merritt, R. RIGHETT, R. Souchon, and S. Srinivasan, "Elastography: imaging the elastic properties of soft tissues with ultrasound," *J. Med*, vol. 29, p. 156, 2002.
- [102] F. M. Tanter M, "Elastography using ultrasound or magnetic resonance: New imaging tools for cancer diagnosis," *Méd Nucl*, vol. 31, pp. 132–141, 2007.
- [103] J. Ophir, B. Garra, F. Kallel, E. Konofagou, T. Krouskop, R. Righetti, and T. Varghese, "Elastographic imaging," *Ultrasound in Medicine and Biology*, vol. 26, no. 1, p. 23, 2000.
- [104] A. Itoh, E. Ueno, E. Tohno, H. Kamma, H. Takahashi, T. Shiina, M. Yamakawa, and T. Matsumura, "Breast Disease: Clinical Application of US Elastography for Diagnosis1," *Radiology*, vol. 239, no. 2, pp. 341–350, May 2006.
- [105] T. A. Krouskop, D. R. Dougherty, and F. S. Vinson, "A pulsed Doppler ultrasonic system for making noninvasive measurements of the mechanical properties of soft tissue," *J. Rehabil. Res. Dev*, vol. 24, no. 2, pp. 1–8, 1987.
- [106] S. Catheline, F. Wu, and M. Fink, "A solution to diffraction biases in sonoelasticity: The acoustic impulse technique," *The Journal of the Acoustical Society of America*, vol. 105, no. 5, pp. 2941–2950, 1999.
- [107] L. Sandrin, M. Tanter, J.-L. Gennisson, S. Catheline, and M. Fink, "Shear elasticity probe for soft tissues with 1-D transient elastography," *IEEE Transactions on Ultrasonics, Ferroelectrics and Frequency Control*, vol. 49, no. 4, pp. 436–446, Apr. 2002.
- [108] A. Popescu and I. Sporea, "ShearWave Elastography (SWE)," *Hepatic Elastography Using Ultrasound Waves*, p. 96.
- [109] T. Karlas, M. Tröltzsch, J. Wiegand, and V. Keim, "Use of Aixplorer® for Detection of Liver Fibrosis or Cirrhosis in Patients with Hepatitis C," *Ultrasound in Medicine and Biology*, vol. 37, no. 8, p. 5, 2011.

- 
- [110] R. Muthupillai, D. Lomas, P. Rossman, J. Greenleaf, A. Manduca, and R. Ehman, "Magnetic resonance elastography by direct visualization of propagating acoustic strain waves," *Science*, vol. 269, no. 5232, pp. 1854–1857, Sep. 1995.
- [111] R. Sinkus, M. Tanter, S. Catheline, J. Lorenzen, C. Kuhl, E. Sondermann, and M. Fink, "Imaging anisotropic and viscous properties of breast tissue by magnetic resonance-elastography," *Magnetic Resonance in Medicine*, vol. 53, no. 2, pp. 372–387, 2005.
- [112] S. A. Kruse, G. H. Rose, K. J. Glaser, A. Manduca, J. P. Felmlee, C. R. Jack, and R. L. Ehman, "Magnetic Resonance Elastography of the Brain," *Neuroimage*, vol. 39, no. 1, pp. 231–237, Jan. 2008.
- [113] M. A. Green, L. E. Bilston, and R. Sinkus, "In vivo brain viscoelastic properties measured by magnetic resonance elastography," *NMR in Biomedicine*, vol. 21, no. 7, pp. 755–764, 2008.
- [114] L. Huwart, F. Peeters, R. Sinkus, L. Annet, N. Salameh, L. C. ter Beek, Y. Horsmans, and B. E. Van Beers, "Liver fibrosis: non-invasive assessment with MR elastography," *NMR in Biomedicine*, vol. 19, no. 2, pp. 173–179, 2006.
- [115] J. Chen, C. Ni, and T. Zhuang, "Imaging mechanical shear waves induced by piezoelectric ceramics in magnetic resonance elastography," *Chinese Science Bulletin*, vol. 51, no. 6, pp. 755–760, Mar. 2006.
- [116] S. F. Othman, H. Xu, T. J. Royston, and R. L. Magin, "Microscopic magnetic resonance elastography ( $\mu$ MRE)," *Magnetic Resonance in Medicine*, vol. 54, no. 3, pp. 605–615, 2005.
- [117] M. M. Doyley, J. B. Weaver, E. E. W. Van Houten, F. E. Kennedy, and K. D. Paulsen, "Thresholds for detecting and characterizing focal lesions using steady-state MR elastography," *Medical physics*, vol. 30, p. 495, 2003.
- [118] J. Weaver, E. Van Houten, M. Miga, F. Kennedy, A. Hartov, S. Poplack, H. Nagy, and K. Paulsen, "Measurement of harmonic motion for MR elastography," in *Proc. ISMRM, 7th Meeting (Philadelphia, PA)*, 1999, p. 1617.
- [119] K. Uffmann, C. Abicht, W. Grote, H. H. Quick, and M. E. Ladd, "Design of an MR-compatible piezoelectric actuator for MR elastography," *Concepts in Magnetic Resonance*, vol. 15, no. 4, pp. 239–254, 2002.

- 
- [120] Najat SALAMEH, “Développement et validation de l'élastographie pour le diagnostic des pathologies hépatiques chroniques,” Université Catholique de Louvain.
- [121] J. Braun, K. Braun, and I. Sack, “Electromagnetic actuator for generating variably oriented shear waves in MR elastography,” *Magnetic Resonance in Medicine*, vol. 50, no. 1, pp. 220–222, 2003.
- [122] R. Sinkus, J. Lorenzen, D. Schrader, M. Lorenzen, M. Dargatz, and D. Holz, “High-resolution tensor MR elastography for breast tumour detection,” *Physics in Medicine and Biology*, vol. 45, no. 6, pp. 1649–1664, Jun. 2000.
- [123] Benjamin Robert, “Etude des Propriétés Viscoélastiques des Tissus Mous par Elastographie IRM. Une Approche Multi-Echelle.,” Université Paris VII – Denis Diderot UFR Sciences, 2009.
- [124] M. Yin, J. A. Talwalkar, K. J. Glaser, A. Manduca, R. C. Grimm, P. J. Rossman, J. L. Fidler, and R. L. Ehman, “A Preliminary Assessment of Hepatic Fibrosis with Magnetic Resonance Elastography,” *Clin Gastroenterol Hepatol*, vol. 5, no. 10, pp. 1207–1213.e2, Oct. 2007.
- [125] P. Asbach, D. Klatt, U. Hamhaber, J. Braun, R. Somasundaram, B. Hamm, and I. Sack, “Assessment of liver viscoelasticity using multifrequency MR elastography,” *Magnetic Resonance in Medicine*, vol. 60, no. 2, pp. 373–379, 2008.
- [126] I. Sack, B. Beierbach, U. Hamhaber, D. Klatt, and J. Braun, “Non-invasive measurement of brain viscoelasticity using magnetic resonance elastography,” *NMR in Biomedicine*, vol. 21, no. 3, pp. 265–271, 2008.
- [127] X. Maître, L. Darrasse, R. Sinkus, and B. Louis, “Apparatus and method for generating mechanical waves into living bodies, system and method for mapping an organ or tissue and system and method for characterising the mechanical properties of said organ or tissue,” n°10 290 448.9, 17-Aug-2010.
- [128] X. Maitre, E. Lamain, R. Sinkus, B. Louis, and L. Darrasse, “Whole brain MRE with guided pressure waves,” presented at the 19th Annual Meeting of the International Society for Magnetic Resonance in Medicine (ISMRM), Montréal (Canada), 2011.
- [129] Salameh N, Souris L, Diguët E, Sarracanie M, Tardieu M, Sinkus R, Brouillet E, Darrasse L, and Maître X, “Suivi de thérapie thermique intracrânienne par IRM cérébrale

---

multi-paramétrique chez le rat,” presented at the Xème colloque de la Section 30 du CNRS, Strasbourg (France), 2011.

[130] D. B. Plewes, I. Betty, S. N. Urchuk, and I. Soutar, “Visualizing tissue compliance with MR imaging,” *Journal of Magnetic Resonance Imaging*, vol. 5, no. 6, pp. 733–738, 1995.

[131] R. Muthupillai, D. Lomas, P. Rossman, J. Greenleaf, A. Manduca, and R. Ehman, “Magnetic resonance elastography by direct visualization of propagating acoustic strain waves,” *Science*, vol. 269, no. 5232, pp. 1854–1857, Sep. 1995.

[132] O. Bieri, S. Maderwald, M. e. Ladd, and K. Scheffler, “Balanced alternating steady-state elastography,” *Magnetic Resonance in Medicine*, vol. 55, no. 2, pp. 233–241, 2006.

[133] J. Rydberg, R. Grimm, S. Kruse, J. Felmlee, P. McCracken, and R. L. Ehman, “Fast spin-echo magnetic resonance elastography of the brain,” in *Proceedings of the 9th Annual Meeting of ISMRM, Glasgow, Scotland*, 2001, p. 1647.

[134] S. A. Kruse, R. C. Grimm, D. S. Lake, A. Manduca, and R. L. Ehman, “Fast EPI based 3D MR elastography of the brain,” in *Proceedings of the International Society for Magnetic Resonance in Medicine*, 2006, p. 3385.

[135] S. Maderwald, K. Uffmann, C. J. Galbán, A. de Greiff, and M. E. Ladd, “Accelerating MR elastography: A multiecho phase-contrast gradient-echo sequence,” *Journal of Magnetic Resonance Imaging*, vol. 23, no. 5, pp. 774–780, 2006.

[136] R. Sinkus, M. Tanter, T. Xydeas, S. Catheline, J. Bercoff, and M. Fink, “Viscoelastic shear properties of in vivo breast lesions measured by MR elastography,” *Magn Reson Imaging*, vol. 23, no. 2, pp. 159–65, 2005.

[137] D. A. Herzka, M. S. Kotys, R. Sinkus, R. I. Pettigrew, and A. M. Gharib, “Magnetic resonance elastography in the liver at 3 Tesla using a second harmonic approach,” *Magn Reson Med*, vol. 62, no. 2, pp. 284–91, 2009.

[138] H. Lum and W. Mitzner, “Effects of 10% formalin fixation on fixed lung volume and lung tissue shrinkage. A comparison of eleven laboratory species,” *Am. Rev. Respir. Dis.*, vol. 132, no. 5, pp. 1078–1083, Nov. 1985.

[139] Santarelli Roberta, “In vivo lung elastography with hyperpolarised helium-3 MRI,” ESMRMB, Valencia, Spain, 2008.

- 
- [140] J. P. Butler, J. L. Lehr, and J. M. Drazen, “Longitudinal elastic wave propagation in pulmonary parenchyma,” *J Appl Physiol*, vol. 62, no. 4, pp. 1349–1355, Apr. 1987.
- [141] M. Salerno, E. E. de Lange, T. A. Altes, J. D. Truwit, J. R. Brookeman, and 3rd Mugler, J. P., “Emphysema: hyperpolarized helium 3 diffusion MR imaging of the lungs compared with spirometric indexes—initial experience,” *Radiology*, vol. 222, no. 1, pp. 252–60, 2002.
- [142] S. Patz, F. W. Hersman, I. Muradian, M. I. Hrovat, I. C. Ruset, S. Ketel, F. Jacobson, G. P. Topulos, H. Hatabu, and J. P. Butler, “Hyperpolarized (129)Xe MRI: a viable functional lung imaging modality?,” *Eur J Radiol*, vol. 64, no. 3, pp. 335–44, 2007.
- [143] E. E. de Lange, T. A. Altes, J. T. Patrie, J. D. Gaare, J. J. Knake, 3rd Mugler, J. P., and T. A. Platts-Mills, “Evaluation of asthma with hyperpolarized helium-3 MRI: correlation with clinical severity and spirometry,” *Chest*, vol. 130, no. 4, pp. 1055–62, 2006.
- [144] S. Samee, T. Altes, P. Powers, E. E. de Lange, J. Knight-Scott, G. Rakes, 3rd Mugler, J. P., J. M. Ciambotti, B. A. Alford, J. R. Brookeman, and T. A. Platts-Mills, “Imaging the lungs in asthmatic patients by using hyperpolarized helium-3 magnetic resonance: assessment of response to methacholine and exercise challenge,” *J Allergy Clin Immunol*, vol. 111, no. 6, pp. 1205–11, 2003.
- [145] Santarelli Roberta, “Fluid/structure coupling in the lung parenchyma for quantitative hyperpolarised helium-3 MR-elastography,” ESMRMB, Antalya, Turkey, 2009.
- [146] R. J. Knudson, D. F. Clark, T. C. Kennedy, and D. E. Knudson, “Effect of Aging Alone on Mechanical Properties of the Normal Adult Human Lung,” *J Appl Physiol*, vol. 43, no. 6, pp. 1054–1062, Dec. 1977.
- [147] E. A. Hoffman, “Effect of body orientation on regional lung expansion: a computed tomographic approach,” *J Appl Physiol*, vol. 59, no. 2, pp. 468–480, Aug. 1985.
- [148] Friese M., “Gas content dependence in Magnetic Resonance Elastography of the lungs,” ISMRM, Stokolm, 2010.
- [149] R. Sinkus, K. Siegmann, T. Xydeas, M. Tanter, C. Claussen, and M. Fink, “MR elastography of breast lesions: Understanding the solid/liquid duality can improve the specificity of contrast-enhanced MR mammography,” *Magnetic Resonance in Medicine*, vol. 58, no. 6, pp. 1135–1144, 2007.

- 
- [150] N. Cakar, T. V. der Kloot, M. Youngblood, A. Adams, and A. Nahum, "Oxygenation Response to a Recruitment Maneuver during Supine and Prone Positions in an Oleic Acid-Induced Lung Injury Model," *Am. J. Respir. Crit. Care Med.*, vol. 161, no. 6, pp. 1949–1956, Jun. 2000.
- [151] N. Cakar, T. V. der Kloot, M. Youngblood, A. Adams, and A. Nahum, "Oxygenation Response to a Recruitment Maneuver during Supine and Prone Positions in an Oleic Acid-Induced Lung Injury Model," *Am. J. Respir. Crit. Care Med.*, vol. 161, no. 6, pp. 1949–1956, Jun. 2000.
- [152] R. Sinkus, J. Lorenzen, D. Schrader, M. Lorenzen, M. Dargatz, and D. Holz, "High-resolution tensor MR elastography for breast tumour detection," *Physics in Medicine and Biology*, vol. 45, no. 6, pp. 1649–1664, Jun. 2000.
- [153] R. Sinkus, K. Siegmann, T. Xydeas, M. Tanter, C. Claussen, and M. Fink, "MR elastography of breast lesions: Understanding the solid/liquid duality can improve the specificity of contrast-enhanced MR mammography," *Magnetic Resonance in Medicine*, vol. 58, no. 6, pp. 1135–1144, 2007.
- [154] S. Lehnert, L. J. Schreiner, and E. el-Khatib, "Factors influencing lung density in experimental models: results of studies using CT densitometry," *Physiol Meas*, vol. 14, no. 2, pp. 183–193, May 1993.
- [155] W. Biernacki, A.T. Redpath, J.J.K. Best, and W. MacNee, "Measurement of CT lung density in patients with chronic asthma," *European Respiratory Journal*, vol. 10, pp. 2455–2459, 1997.
- [156] R. Yuan, T. Nagao, P. D. Paré, J. C. Hogg, D. D. Sin, M. W. Elliott, L. Loy, L. Xing, S. E. Kalloger, J. C. English, J. R. Mayo, and H. O. Coxson, "Quantification of lung surface area using computed tomography," *Respiratory Research*, vol. 11, no. 1, p. 153, Oct. 2010.
- [157] M. Jahed and S. J. Lai-Fook, "Stress wave velocity measured in intact pig lungs with cross-spectral analysis," *J Appl Physiol*, vol. 76, no. 2, pp. 565–571, Feb. 1994.
- [158] D. A. Rice, "Sound speed in pulmonary parenchyma," *J Appl Physiol*, vol. 54, no. 1, pp. 304–308, Jan. 1983.
- [159] Y. K. Mariappan, K. J. Glaser, R. D. Hubmayr, A. Manduca, R. L. Ehman, and K. P. McGee, "MR elastography of human lung parenchyma: technical development, theoretical

modeling and in vivo validation,” *J Magn Reson Imaging*, vol. 33, no. 6, pp. 1351–1361, Jun. 2011.

[160] S. Ajraoui, K. J. Lee, M. H. Deppe, S. R. Parnell, J. Parra-Robles, and J. M. Wild, “Compressed sensing in hyperpolarized  $^3\text{He}$  Lung MRI,” *Magnetic Resonance in Medicine*, vol. 63, no. 4, pp. 1059–1069, 2010.

[161] R. F. Lee, G. Johnson, R. I. Grossman, B. Stoeckel, R. Trampel, and G. McGuinness, “Advantages of parallel imaging in conjunction with hyperpolarized helium—A new approach to MRI of the lung,” *Magnetic Resonance in Medicine*, vol. 55, no. 5, pp. 1132–1141, 2006.

[162] F. G. Salerno and M. S. Ludwig, “Elastic moduli of excised constricted rat lungs,” *J. Appl. Physiol.*, vol. 86, no. 1, pp. 66–70, Jan. 1999.

[163] R. K. Lambert and P. D. Paré, “Lung parenchymal shear modulus, airway wall remodeling, and bronchial hyperresponsiveness,” *J. Appl. Physiol.*, vol. 83, no. 1, pp. 140–147, Jul. 1997.

[164] Mount LE., “The ventilation flow-resistance and compliance of rat lungs,” *J Physiol Lond*, vol. 127, pp. I57–I67, 1955.

[165] V. Antonaglia, A. Grop, P. Demanins, F. Beltrame, U. Lucangelo, A. Peratoner, L. De Simoni, A. Gullo, and J. Milic-Emili, “Single-breath method for assessing the viscoelastic properties of the respiratory system,” *Eur. Respir. J.*, vol. 12, no. 5, pp. 1191–1196, Nov. 1998.

[166] L. E. Bayliss and G. W. Robertson, “The Visco-Elastic Properties of the Lungs,” *Exp Physiol*, vol. 29, no. 1, pp. 27–47, Mar. 1939.

[167] N. Salameh, B. Larrat, J. Abarca-Quinones, S. Pallu, M. Dorvillius, I. Leclercq, M. Fink, R. Sinkus, and B. E. V. Beers, “Early Detection of Steatohepatitis in Fatty Rat Liver by Using MR Elastography<sup>1</sup>,” *Radiology*, vol. 253, no. 1, pp. 90–97, Oct. 2009.

[168] R. Sinkus, K. Siegmann, T. Xydeas, M. Tanter, C. Claussen, and M. Fink, “MR elastography of breast lesions: Understanding the solid/liquid duality can improve the specificity of contrast-enhanced MR mammography,” *Magnetic Resonance in Medicine*, vol. 58, no. 6, pp. 1135–1144, 2007.

---

[169] A.-L. A. Katzenstein and J. L. Myers, "Idiopathic Pulmonary Fibrosis Clinical Relevance of Pathologic Classification," *Am. J. Respir. Crit. Care Med.*, vol. 157, no. 4, pp. 1301–1315, Apr. 1998.

[170] E. Meltzer and P. Noble, "Idiopathic pulmonary fibrosis," *Orphanet Journal of Rare Diseases*, vol. 3, no. 1, p. 8, Mar. 2008.